Development of Reduced-Order Models for Lift and Drag on Oscillating Cylinders with Higher-Order Spectral Moments

Lihai Qin

Dissertation submitted to the Faculty of the Virginia Polytechnic Institute and State University in partial fullfillment of the requirements for the degree of

Doctor of Philosophy

In

Engineering Mechanics

Muhammad R. Hajj, Chair

Dean T. Mook

Daniel J. Inman

Saad A. Ragab

Ronald D. Kriz

November, 2004

Blacksburg, VA

Keywords: Reduced-Order Model, Lift, Drag, Cylinder, Higher-Order Spectral Moments, Trispectrum, Nonlinear Identification

Development of Reduced-Order Models for Lift and Drag on Oscillating Cylinders with Higher-Order Spectral Moments

Lihai Qin

ABSTRACT

An optimal solution of vortex-induced vibrations of structures would be a time-domain numerical simulation that simultaneously solves the fluid flow and structural response. Yet, the requirements in terms of computing power remains a major obstacle for implementing such a simulation. On the other hand, lower- or reduced-order models provide an alternative for determining structural response to forcing by fluid flow. The objective of this thesis is to provide a consistent approach for the development of reduced-order models for the lift and drag on oscillating cylinders and the identification of their parameters. Amplitudes and phases of higher-order spectral moments of the lift and drag coefficients data are combined with approximate solutions of the representative models to determine their parameters. The results show that the amplitude and phase of the trispectrum could be used to model the lift on the oscillating cylinder under different excitation conditions. Moreover, the amplitude and phase of the cross-bispectrum could be used to establish the lift-drag relation for oscillating cylinders. A forced van der Pol equation is used to represent the lift on a transversely oscillating cylinder, and a parametrically excited van der Pol equation is used to model the lift coefficient on an inline oscillating cylinder. All cases of excitations lead to close values for the damping and nonlinear parameters in the van der Pol equation. Consequently, and as shown in this thesis, different excitation cases could be used to identify the parameters in the governing equations.

Moreover, the results show that the drag coefficient could be derived from the lift coefficient through a square relation that takes into account the effects of the forced motions.

Acknowledgements

As it comes to the end of my Ph.D. study, I would like to thank all people who have taught, supported and assisted me. First, I must acknowledge my research advisor, Professor Muhammad R. Hajj, for his intelligent guidance, support and time given to my research. I must as well thank Professors Dean T. Mook, Daniel J. Inman, Saad A. Ragab, and Ronald D. Kriz for providing their advice and serving as the committee members. Additionally, I also would like to thank Professor Ali H. Nayfeh and Professor Henry W. Tieleman for providing invaluable advice. I should also thank Dr. Farouk Owis for providing the RANS data that are analyzed in this work.

There is a special person, my wife, Juan Ouyang, in my life that I must acknowledge. Without her encouragement and support, I would have given up my Ph.D study.

Finally, thank God.

Table of Contents

List of Figures

List of Tables

Chapter 1

Introduction

1.1 Background

Vortex shedding, induced by a fluid flow past a structure or a structural element, leads to fluctuating lift and drag forces. In cases where the structure or element is flexible or elastically constrained, these forces induce structural motions. These motions can be significantly amplified under lock-in conditions where the vortex shedding frequency is near a natural frequency of the structure or when the ratio of the structures' mass to the fluid's mass of its equivalent volume is small. Such amplified responses are of great concern in many practical applications. In offshore oil production systems, risers of up to 2000 m in length have been installed to convey fluids from seabed to water surface. These risers are circular cylinders of one or two meters in diameter and are subjected to the oscillatory flow caused by waves and to currents with significant shear profiles. The vortex shedding frequency at any depth may result in constructive interference to excite one or more structural modes. Vortex-induced vibrations are also significant when considering the wind flow around tall building, bridges, and chimney stacks. Besides the potential for catastrophic incidents, such as the collapse of the Tacoma Narrows bridge, wind-induced motions of tall buildings can cause a great deal of discomfort. Vortex induced vibrations have also been a problem in heat exchanger tubes. Such vibrations cause the tubes to move, strike each other, and /or vibrate against their supports. These phenomena cause the tube walls to wear thin or crack.

An optimal solution of vortex-induced vibrations of structures would be a time-domain numerical simulation of the fluid flow and the structure's response. In this solution, the fluid and structure would be treated as a single dynamical system and all governing equations would be solved simultaneously in time. Obviously, this is not a simple task, especially when considering the facts that the Reynolds number associated with the applications of these flows is usually large and that these flows usually have many complex features. The prediction of fluid forces can be made with different assumptions, including inviscid flow and the use of vortex lattice, Euler equations or viscous flows with different turbulence models. The use of more advanced simulations such as Large Eddy Simulation (LES) or Direct Numerical Simulation (DNS) is very limited because of their needs in terms of computing power. Modeling the structural motions is also limited by the number of the degrees of freedom and assumptions made in setting the structural operator. These complications and assumptions are significantly magnified because of the need to model the structure's motions as well.

On the other hand, the practical effects of the vortex-induced vibrations phenomenon has lead to a large number of fundamental studies whereby different aspects of this phenomenon have been independently considered. These studies have been concerned with the characteristics of the fluid flow and vortex shedding phenomena behind bluff bodies, the modeling of the lift and drag forces on stationary and moving cylinders, the lock-in phenomenon and feedback between body motion and vortex shedding, and the introduction of passive and active control techniques to dampen the structural motions. The large number of these studies and results has lead to better understanding of the vortex shedding and vortex-induced vibrations phenomena.

1.1.1 Vortex Shedding Regimes and Physics

In the flow over circular cylinders and their oscillations, laminar vortex shedding could take place at a Reynolds number(Re) as low as 50 with an upper limit of about 200[1]. For Re values between 200 and 100,000, the nondimensional frequency for the vortex shedding, also known as the Strouhal number, is about 0.2 and the flow regime is referred to as subcritical. In the lower part of this regime, Re up to 260, intermittent low-frequency velocity fluctuations are observed. These are caused by local shedding phase dislocations along the span[2]. Beyond Re of 1000, fine-scale streamwise vortex structures have been observed. Over Re of about 1000, the shear layer instability plays an important role in the characteristics of the vortex shedding. At a Re of about 100,000, the transition to turbulence starts to take place in the boundary layer over the cylinder at or near the point of separation. Beyond Re of 100,000 and up to about 4,000,000, there is a signifcant rise in the Strouhal number or a loss of organized vortex shedding[3]. This regime is referred to as the supercritical regime. Beyond Re of 4,000,000, the separating boundary layer on the surface of the cylinder is fully turbulent. In this regime, usually referred to as transcritical regime, organized vortex shedding is re-established with a Strouhal number of about 0.26 - 0.3.

The physics of the vortex shedding phenomenon have been the subject of several studies. By representing the two parallel shear layers of opposing signs by rows of point vortices, Abernathy & Kronauer[4] showed that the two shear layers, and not the body itself, are responsible for vortex shedding. The role of the bluff body is simply to allow feedback between the wake and the shedding of circulation at the separation points. Gerrard[5] determined that an important aspect of the formation of the vortex street is the interaction between the separating shear layers. The growing vortex from one of the shear layers will grow until it becomes strong enough to draw the opposing shear layer, which contains oppositely signed vorticity, across the wake. A part of the drawn shear layer will then cut off the circulation supply of the growing vortex and cause it to shed. Sarpakaya[6] offers a more complicated process for the vortex shedding. He postulated that with the initial symmetric growth of vortices, one of the shear layers begins to develop instabilities and is drawn across the wake due to the reduced base pressure brought about by the presence of a growing vortex across the wake. This corresponds to the time when the drawn shear layer has least circulation. The drawn shear layer breaks up the other layer causing a reduction in the supply of vorticity to the growing vortex which leads to its shedding. The opposite vortex entrains part of the oppositely signed vorticity left in the wake by the cut layer and some of the irrotational fluid from outside the opening created by the shedding of the vortex. The shedding process for the second vortex starts when the circulation feeding it decreases to its minimum. At that time, the corresponding shear layer is again drawn across the wake and the vortex is shed. This process continuously repeats itself.

1.1.2 Modeling the Vortex Shedding

Over the past two decades there has been an interest in relating the vortex shedding phenomenon to flow stability and to nonlinear dynamical systems. In several studies, the vortex shedding phenomenon and some of its aspects have been modeled by dynamical systems. Provansal et al.[7] showed that the vortex street behind a circular cylinder, at low Reynolds number, is a self-excited limit cycle oscillation of the entire wake that can be modeled by the Stuart Landau equation, which, for complex amplitude A, has the form

$$\frac{dA}{dt} = \sigma A - \lambda \left|A\right|^2 A \tag{1.1}$$

where the parameters σ and λ are complex. The real part of σ, σ_r, represents the growth rate. For negative values of σ_r, $A = 0$ is a stable solution. For positive values of σ_r, the steady-state solution is a periodic one with constant amplitude. Provansal et al.[7] also proposed that the Stuart Landau model can be extended to a Ginzberg - Landau model by the addition of a diffusive term to account for three dimensional effects. Alberde and Monkewitz[8], Williamson[9] and Roussopoulos and Monkewitz[10] showed that phase transitions, oblique shedding and chevron patterns could actually be modeled by the Ginzburg-Landau equation with a diffusive term along the span. This equation has the form

$$\frac{\partial A}{\partial t} = \sigma A - \lambda \left|A\right|^2 + \mu \frac{\partial^2 A}{\partial z^2} \tag{1.2}$$

Noack et al.[11] modeled the vortex shedding and its spanwise variations with a van der Pol oscillators with diffusive spanwise coupling. A similar oscillator was also used to model the vortex shedding from uniform cylinders in shear flows (Balasubramanian and Skop[12])

1.1.3 Modeling the Lift, Drag, and Vortex-Induced Vibrations

The shedding of vortices induces in-line and transverse forces on the cylinder. Similar to the representation of the vortex shedding by a nonlinear dynamical system, several investigators have proposed the representation of the fluctuating lift force by a nonlinear oscillator equation such as the Rayleigh or van der Pol equation to represent the lift force. One of the first models proposed to model the vortex induced vibrations of circular cylinders is the one proposed by Hartlen and Currie[13]. In that model the lift, represented by a Rayleigh equation, is linearly coupled to the cylinder's motion. In nondimentional form, the pair of equations which result from this model are written as

$$\ddot{l} + \omega_o^2 l - \mu \omega_o \dot{l} + \frac{\alpha}{\omega_o} \dot{l}^3 = B\dot{y} \tag{1.3}$$

and

$$\ddot{y} + 2\xi\dot{y} + y = A\omega_o^2 l \tag{1.4}$$

In this equation, ω_o is the normalized frequency, μ, ξ, α, A and B are parameters. This model had several discrepancies with experimental data[6]. In particular, the model yields continuous variations in the phase angle between the excitation and response and fails to predict the high amplitude response outside the lock-in region and that is observed in many experiments.

By comparison, there has not been as many proposed models for the drag force. Currie and Turnball[14] proposed a model similar to the wake oscillator model for the fluctuations of the drag coefficient. To study resonant responses of suspended elastic cables, Kim and Perkins[15] used a coupled model, based on two van der Pol equations for the drag and lift coefficients. In this model, the drag is affected by many possibilities of quadratic couplings of the lift. Additionally, the lift is affected by its quadratic coupling with the drag. These couplings were introduced based on the fact that the main frequency of the drag component is twice the main frequency of the lift component.

Nayfeh, Owis and Hajj[16] showed that the lift coefficient, l, on stationary circular cylinders should be modeled by the self-excited van der Pol oscillator written as

$$\ddot{l} + \omega_s^2 l - \mu_v \dot{l} + \alpha_v l^2 \dot{l} = 0 \tag{1.5}$$

where ω_s is the shedding frequency, μ_v and α_v represent the linear and nonlinear damping coefficient. Their results showed that the van der Pol oscillator can be used to model the lift coefficient over a wide range of Re. Additionally, they showed that the drag coefficient can be modeled by

$$d = d_m - C l \dot{l} \tag{1.6}$$

where d_m is the drag and C is a constant of proportionality to $l\dot{l}$; both of which are a function of Re.

1.2 Objectives

This thesis aims at providing an analysis procedure for the development of reduced-order models for the lift and drag on oscillating circular cylinders and the identification of their parameters. In particular, a consistent approach will be presented to identify the parameters in these models. The approach is (1) to develop higher-order spectral moments as tools to identify quadratic and cubic nonlinearities in the time series of the drag and lift coefficients and (2) combine amplitude and phase estimates of these moments with approximate solutions of the governing equations to determine the parameters in the reduced-order models. This approach is implemented to determine the lift and drag coefficients on a cylinder that is forced in the inline and transverse directions. Different forcing conditions are used to examine their effects on the derived parameters.

In Chapter 2, a review of higher-order spectral moments is given. In particular, a detailed discussion of the trispectrum and its use for the detection of cubic nonlinearities is presented. In Chapter 3, the work of Nayfeh et al.[16] is extended to show how the magnitude as well as the phase of the trispectrum can be used to identify the parameters of the self-excited van der Pol equation used to represent the lift coefficient. A different model for the drag-lift relation that is validated with spectral analysis is presented. In Chapter 4, a reduced order model for the lift on a circular cylinder oscillating in the transverse direction under different resonance conditions is obtained by combining spectral analysis and approximate solutions of the van der Pol equation. The drag coefficient is determined through an analysis that makes use of the cross-bispectrum. In Chapter 5, an analysis similar to the one used in Chapter 4 is performed to obtain the parameters in a reduced-order model for the lift and drag on a cylinder oscillating in the inline direction. In Chapter 6, the issue of using forced-vibrations models to predict free-vibrations is discussed. Finally, the conclusions of this work are presented in Chapter 7.

Chapter 2

Higher-Order Spectral Moments and Data Analysis

Traditional signal processing techniques used in data analysis are based on second-order statistics, such as the power spectra and correlation functions. These measures are easy to implement and have straightforward interpretations such as energy content of the frequency components of a signal or the coherence of same frequency components in two signals. However, in many cases, estimation of higher-order spectral moments can be used to obtain more information from signals or time series.

In nonlinear systems, frequency components interact to pass energy to other components at their sum and/or difference frequencies. Because of this interaction, the phases of the interacting components are coupled. This phase coupling can be used for the detection of nonlinear interactions between frequency components in one or more time series. Two higher-order spectral moments of particular interest to this work are the bispectrum and trispectrum. Faced with an unknown system in terms of its nonlinear characteristics, these moments can be applied to identify quadratic and cubic nonlinearities. The bispectrum, which is the next higher-order moment to the power spectrum, has been established as a tool to quantify the level of phase coupling among three frequency components and thus identify quadratic nonlinearities. In this chapter, we present a brief review and explanations of higher-order spectral moments and their use for detection of quadratic and cubic nonlinearities. We also provide a detailed treatment and an example of the trispectrum to show how it can be used to identify cubic nonlinearities through assessment of the phase relation between three frequency components and their algebraic sum.

2.1 Higher-Order Spectral Analysis

2.1.1 Definition of Cumulants and Moments

Higher-order spectra are defined in terms of either cumulants (e.g., cumulant spectra) or moments (e.g., moment spectra)[17]. Simply stated, higher-order spectra are multi-dimensional Fourier transforms of higher-order statistics. If $x(t)$ is a real random process and its moments up to order n are stationary, one could define the n^{th}-order moment function as

$$m_n(\tau_1, ..., \tau_{n-1}) = E\{x(t)x(t+\tau_1)...x(t+\tau_{n-1})\} \tag{2.1}$$

where $E\{\}$ represents ensemble averaging and $\tau_1, ..., \tau_{n-1}$ represent time differences.

The first-, second-, third-, and fourth-order cumulants of real-valued stationary random process, $x(t)$, are defined as

$$C_1 = m_1 = E\{x(t)\} \tag{2.2}$$

$$C_2(\tau_1) = m_2(\tau_1) - (m_1)^2 = E\{x(t)x(t+\tau_1)\} - (Ex(t))^2 \tag{2.3}$$

$$C_3(\tau_1, \tau_2) = m_3(\tau_1, \tau_2) - (m_1)[m_2(\tau_1) + m_2(\tau_2) + m_2(\tau_1 - \tau_2)] + 2(m_1)^3 \tag{2.4}$$

and

$$\begin{aligned}
&C_4(\tau_1, \tau_2, \tau_3) = m_4(\tau_1, \tau_2, \tau_3)\\
&-m_2(\tau_1)m_2(\tau_3 - \tau_2) - m_2(\tau_2)m_2(\tau_3 - \tau_1) - m_2(\tau_3)m_2(\tau_2 - \tau_1)\\
&-m_1[m_3(\tau_2 - \tau_1, \tau_3 - \tau_1) + m_3(\tau_2, \tau_3) + m_3(\tau_3, \tau_1) + m_3(\tau_1, \tau_2)]\\
&+(m_1)^2[m_2(\tau_1) + m_2(\tau_2) + m_2(\tau_3) + m_2(\tau_3 - \tau_1) + m_2(\tau_1 - \tau_2)\\
&+m_2(\tau_2 - \tau_3)] - 6(m_1)^4
\end{aligned} \tag{2.5}$$

Obviously, the first-order cumulant is the mean value; the second-order cumulant is the covariance sequence and is related to the second-order moment sequence, $E[x(t)x(t+\tau_1)]$, which represents the autocorrelation. The autocorrelation is a measure of how the random process is correlated with itself at different times.

2.1.2 Cumulant and Moment Spectral Functions

By Fourier transforming the moment and cumulant functions, presented in equations 2.2, 2.3, 2.4, and 2.5, one obtains a hierarchy of higher-order cumulants spectra or moment spectra. One can write the following Fourier transform pairs for the cumulants

$$C_2(\tau) \quad \overset{2}{\longleftrightarrow} \quad S_2(f) \tag{2.6}$$

$$C_3(\tau_1, \tau_2) \quad \overset{3}{\longleftrightarrow} \quad S_3(f_1, f_2) \tag{2.7}$$

and

$$C_4(\tau_1, \tau_2, \tau_3) \quad \overset{4}{\longleftrightarrow} \quad S_4(f_1, f_2, f_3) \tag{2.8}$$

The symbols $\overset{2}{\longleftrightarrow}$, $\overset{3}{\longleftrightarrow}$, and $\overset{4}{\longleftrightarrow}$ denote one-, two-, and three-dimensional Fourier transforms. The quantities $S_2(f)$, $S_3(f_1, f_2)$, and $S_4(f_1, f_2, f_3)$ denote the second-, third-, and fourth-order cumulant spectra, respectively. They are commonly referred to as the auto-power spectrum, auto-bispectrum, and auto-trispectrum respectively. The hierarchy of higher-order cumulant spectra is then expressed as

$$S_2(f) = \int_{\infty}^{\infty} C_2(\tau) e^{-j2\pi f \tau} d\tau \tag{2.9}$$

$$S_3(f_1, f_2) = \int_{\infty}^{\infty} \int_{\infty}^{\infty} C_3(\tau_1, \tau_2) e^{-j2\pi(f_1\tau_1 + f_2\tau_2)} d\tau_1 d\tau_2 \tag{2.10}$$

and

$$S_4(f_1, f_2, f_3) = \int_{\infty}^{\infty} \int_{\infty}^{\infty} \int_{\infty}^{\infty} C_4(\tau_1, \tau_2, \tau_3) e^{-j2\pi(f_1\tau_1 + f_2\tau_2 + f_3\tau_3)} d\tau_1 d\tau_2 d\tau_3 \tag{2.11}$$

Similarly one can write the Fourier transform pairs for the moments as

$$m_2(\tau) \quad \overset{2}{\longleftrightarrow} \quad S_{xx}(f) \tag{2.12}$$

$$m_3(\tau_1, \tau_2) \quad \overset{3}{\longleftrightarrow} \quad S_{xxx}(f_1, f_2) \tag{2.13}$$

and

$$m_4(\tau_1, \tau_2, \tau_3) \quad \overset{4}{\longleftrightarrow} \quad S_{xxxx}(f_1, f_2, f_3) \tag{2.14}$$

The quantities $S_{xx}(f)$, $S_{xxx}(f_1, f_2)$ and $S_{xxxx}(f_1, f_2, f_3)$ are also referred to as the auto-power spectrum, auto-bispectrum and auto-trispectrum. The hierarchy of higher-order moment spectra is then expressed as

$$S_{xx}(f) = \lim_{T\to\infty} \frac{1}{T} E[X_T^*(f) X_T(f)] \tag{2.15}$$

$$S_{xxx}(f_1, f_2) = \lim_{T\to\infty} \frac{1}{T} E[X_T^*(f_1) X_T^*(f_2) X_T(f_1 + f_2)] \tag{2.16}$$

and

$$S_{xxxx}(f_1, f_2, f_3) = \lim_{T\to\infty} \frac{1}{T} E[X_T^*(f_1) X_T^*(f_2) X_T^*(f_3) X_T(f_1 + f_2 + f_3)] \tag{2.17}$$

where $X_T(f)$ is the Fourier transform of $x(t)$ defined over a time duration T, and the superscript * is used to denote complex conjugate.

It is important to note that if $x(t)$ is zero-mean, i.e. $m_1 = 0$, equations 2.3 and 2.4 show that the second- and third- order cumulants are identical to the second- and third- order moments, respectively. Consequently, the moment based auto-power spectrum and auto-bispectrum are equivalent to the cumulant based auto-power spectrum and auto-bispectrum. On the other hand, the fourth-order cumulant function depends on both the fourth- and second- order moment functions in equation 2.5, i.e., for a zero-mean random process,

$$\begin{aligned} C_4(\tau_1, \tau_2, \tau_3) = \quad & m_4(\tau_1, \tau_2, \tau_3) - m_2(\tau_1) m_2(\tau_3 - \tau_2) \\ & - m_2(\tau_2) m_2(\tau_3 - \tau_1) - m_2(\tau_3) m_2(\tau_2 - \tau_1) \end{aligned} \tag{2.18}$$

Consequently, the fourth-order cumulant spectrum is usually different than the fourth-order moment spectrum even though they are both referred to as the trispectrum.

2.1.3 Cross-Spectral Functions

The higher-order moment functions and spectra can also be defined for two random processes $x(t)$ and $y(t)$ according to the following relations

$$S_{yx}(f) = \lim_{T\to\infty} \frac{1}{T} E[X_T^*(f) Y_T(f)] \tag{2.19}$$

$$S_{yxx}(f_1, f_2) = \lim_{T\to\infty} \frac{1}{T} E[X_T^*(f_1) X_T^*(f_2) Y_T(f_1 + f_2)] \tag{2.20}$$

and

$$S_{yxxx}(f_1, f_2, f_3) = \lim_{T\to\infty} \frac{1}{T} E[X_T^*(f_1) X_T^*(f_2) X_T^*(f_3) Y_T(f_1 + f_2 + f_3)] \tag{2.21}$$

In these relations, S_{yx} is known as the cross-power spectrum and is used to determine the relation between the same frequency component in two signals. Its normalized value yields the linear coherence of that component between the two signals. S_{yxx} is the cross-bispectrum and is used to determine the quadratic relation between two frequency components in $x(t)$ and their sum (or difference) in $y(t)$. Its normalized value can be used to determine the level of quadratic coherence between two frequencies in one signal and their sum or difference in the second signal. More details on the interpretation, implementation and uses of the bispectrum and its appications are given in Kim and Powers[18] and Hajj, Miksad and Powers[19]. The cross-trispectrum, S_{yxxx}, is used to determine the relation between three frequency components in $x(t)$ and their sum in $y(t)$.

2.2 The Trispectrum and Cubic Nonlinearities

Because the second- and third-order moment spectra are most commonly used and have been discussed extensively in the literature, we will expand in this section on the properties of the auto-trispectrum and its usefulness in the detection of cubic nonlinearities.

2.2.1 Symmetry Properties of Auto-Trispectrum

The auto-trispectrum, as defined in equation 2.21, has many symmetry properties. For a real-valued time series $x(t)$, it is only necessary to evaluate the trispectrum in the principal domain or non-redundant area, as all other regions can be found by symmetrical transformations of this area.

The auto-trispectrum has 96 regions of symmetry and has been discussed extensively[20]. Based on these regions, the principal domain of the trispectrum is given by the following:

for $f_3 \geq 0$,

$$\begin{aligned} &1 \geq f_1 \geq f_2 \geq f_3 \geq 0, \\ &1 \geq f_1 + f_2 + f_3 \end{aligned} \tag{2.22}$$

and for $f_3 < 0$,

$$\begin{aligned} &1 \geq f_1 \geq f_2 \geq 0 > f_3 \geq -1, \\ &f_1 + f_2 + 2f_3 \geq 0, \\ &1 \geq f_1 + f_2 + f_3 \end{aligned} \tag{2.23}$$

2.2.2 Use of Trispectrum to Detect Cubically Coupled Modes

To show how the trispectrum can be used to detect cubic nonlinearites, we consider the function

$$y(t) = x(t) + x^3(t) \tag{2.24}$$

where $x(t)$ is given by

$$x(t) = cos(\omega_1 t + \phi_1) + cos(\omega_2 t + \phi_2) + cos(\omega_3 t + \phi_3) \tag{2.25}$$

Substituting equation 2.25 in equation 2.24 and expanding the cubic nonlinear term, one obtains

$$\begin{aligned}
y(t) = \; & \tfrac{1}{4}(19cos[\omega_1 t + \phi_1] + cos[3\omega_1 t + 3\phi_1] + 3cos[(\omega_1 - 2\omega_2)t + \phi_1 - 2\phi_2] \\
& +3cos[(2\omega_1 - \omega_2)t + 2\phi_1 - \phi_2] + 19cos[\omega_2 t + \phi_2] + cos[3\omega_2 t + 3\phi_2] \\
& +3cos[(2\omega_1 + \omega_2)t + 2\phi_1 + \phi_2] + 3cos[(2\omega_2 + \omega_1)t + 2\phi_2 + \phi_1] \\
& +3cos[(\omega_1 - 2\omega_3)t + \phi_1 - 2\phi_3] + 3cos[(\omega_2 - 2\omega_3)t + \phi_2 - 2\phi_3] \\
& +3cos[(2\omega_1 - \omega_3)t + 2\phi_1 - \phi_3] + 6cos[(\omega_1 - \omega_2 - \omega_3)t + \phi_1 - \phi_2 - \phi_3] \\
& +6cos[(\omega_1 + \omega_2 - \omega_3)t + \phi_1 + \phi_2 - \phi_3] + 3cos[(2\omega_2 - \omega_3)t + 2\phi_2 - \phi_3] \\
& +19cos[\omega_3 t + \phi_3] + cos[3\omega_3 t + 3\phi_3] + 3cos[(2\omega_1 + \omega_3)t + 2\phi_1 + \phi_3] \\
& +6cos[(\omega_1 - \omega_2 + \omega_3)t + \phi_1 - \phi_2 + \phi_3] \\
& +6cos[(\omega_1 + \omega_2 + \omega_3)t + \phi_1 + \phi_2 + \phi_3] \\
& +3cos[(2\omega_2 + \omega_3)t + 2\phi_2 + \phi_3] + 3cos[(\omega_1 + 2\omega_3)t + \phi_1 + 2\phi_3] \\
& +3cos[(\omega_2 + 2\omega_3)t + \phi_2 + 2\phi_3])
\end{aligned} \tag{2.26}$$

Obviously, $y(t)$ contains cosinusoidal terms in (ω_1, ϕ_1), (ω_2, ϕ_2), (ω_3, ϕ_3), $(3\omega_1, 3\phi_1)$, $(3\omega_2, 3\phi_2)$, $(3\omega_3, 3\phi_3)$, $(2\omega_1 + \omega_2, 2\phi_1 + \phi_2)$, $(2\omega_2 + \omega_1, 2\phi_2 + \phi_1)$,

$(2\omega_1 + \omega_3, 2\phi_1 + \phi_3)$, $(2\omega_3 + \omega_1, 2\phi_3 + \phi_1)$, $(2\omega_2 + \omega_3, 2\phi_2 + \phi_3)$, $(2\omega_3 + \omega_2, 2\phi_3 + \phi_2)$, $(2\omega_1 - \omega_2, 2\phi_1 - \phi_2)$, $(2\omega_2 - \omega_1, 2\phi_2 - \phi_1)$, $(2\omega_1 - \omega_3, 2\phi_1 - \phi_3)$, $(2\omega_3 - \omega_1, 2\phi_3 - \phi_1)$, $(2\omega_2 - \omega_3, 2\phi_2 - \phi_3)$, $(2\omega_3 - \omega_2, 2\phi_3 - \phi_2)$, $(\omega_1 + \omega_2 + \omega_3, \phi_1 + \phi_2 + \phi_3)$, $(\omega_1 + \omega_2 - \omega_3, \phi_1 + \phi_2 - \phi_3)$, $(\omega_1 - \omega_2 + \omega_3, \phi_1 - \phi_2 + \phi_3)$, and $(\omega_1 - \omega_2 - \omega_3, \phi_1 - \phi_2 - \phi_3)$. Thus, the cubic nonlinearities give rise to sum and difference components of ω_1, ω_2, ω_3. Additionally, it is important to note how the phases of the sum and difference components follow the same algebraic sum as the frequencies.

Next, it is shown how the trispectrum, when averaged over several data segments, is capable of detecting phase coupling for cubically coupled frequency components as given in Equation 2.26. To show that, we consider the process

$$x(t) = \sum_{i=1}^{4} cos(\omega_i t + \phi_i) \tag{2.27}$$

where

$$\omega_i > 0, \text{ and } \omega_4 = \omega_1 + \omega_2 + \omega_3 \tag{2.28}$$

and where the phases ϕ_1, ϕ_2, ϕ_3 are all independent and uniformly distributed random variables over $(0, 2\pi)$. It should be noted that when ϕ_i is independent and uniformly distributed, the expected value

$$E\{cos(\omega_i t + \phi_i)\} = 0 \tag{2.29}$$

The fourth-order cumulant sequence $C_4(\tau_1, \tau_2, \tau_3)$ of $x(t)$ is defined as

$$\begin{aligned} C_4(\tau_1, \tau_2, \tau_3) = \quad & E\{x(t)x(t+\tau_1)x(t+\tau_2)x(t+\tau_3)\} \\ & E\{x(t)x(t+\tau_1)\}E\{x(t+\tau_2)x(t+\tau_3)\} \\ & E\{x(t)x(t+\tau_2)\}E\{x(t+\tau_1)x(t+\tau_3)\} \\ & E\{x(t)x(t+\tau_3)\}E\{x(t+\tau_1)x(t+\tau_3)\} \end{aligned} \tag{2.30}$$

For the case where all phases, ϕ_1, ϕ_2, ϕ_3, ϕ_4, are independent and uniformly distributed over $(0, 2\pi)$, the substitution of equation 2.25 into equation 2.30 and application of equation 2.29 yield the fourth-order cumulant

$$\begin{aligned} & C_4(\tau_1, \tau_2, \tau_3) = \\ & -\tfrac{1}{8}cos[(\tau_1 - \tau_2 - \tau_3)\omega_1] - \tfrac{1}{8}cos[(\tau_1 + \tau_2 - \tau_3)\omega_1] - \tfrac{1}{8}cos[(\tau_1 - \tau_2 + \tau_3)\omega_1] \\ & -\tfrac{1}{8}cos[(\tau_1 - \tau_2 - \tau_3)\omega_2] - \tfrac{1}{8}cos[(\tau_1 + \tau_2 - \tau_3)\omega_2] - \tfrac{1}{8}cos[(\tau_1 - \tau_2 + \tau_3)\omega_2] \\ & -\tfrac{1}{8}cos[(\tau_1 - \tau_2 - \tau_3)\omega_3] - \tfrac{1}{8}cos[(\tau_1 + \tau_2 - \tau_3)\omega_3] - \tfrac{1}{8}cos[(\tau_1 - \tau_2 + \tau_3)\omega_3] \\ & -\tfrac{1}{8}cos[(\tau_1 - \tau_2 - \tau_3)\omega_4] - \tfrac{1}{8}cos[(\tau_1 + \tau_2 - \tau_3)\omega_4] - \tfrac{1}{8}cos[(\tau_1 - \tau_2 + \tau_3)\omega_4] \end{aligned} \tag{2.31}$$

The third-order Fourier transform of equation 2.31, i.e. the auto-trispectrum of $x(t)$, is then given by

$$
\begin{aligned}
&S_{xxxx}(\omega_i, \omega_j, \omega_k) = \\
&-\tfrac{1}{16}\delta(\omega_1+\omega_i)\delta(\omega_1-\omega_j)\delta(\omega_1-\omega_k) - \tfrac{1}{16}\delta(\omega_1-\omega_i)\delta(\omega_1+\omega_j)\delta(\omega_1-\omega_k) \\
&-\tfrac{1}{16}\delta(\omega_1+\omega_i)\delta(\omega_1+\omega_j)\delta(\omega_1-\omega_k) - \tfrac{1}{16}\delta(\omega_2+\omega_i)\delta(\omega_2-\omega_j)\delta(\omega_2-\omega_k) \\
&-\tfrac{1}{16}\delta(\omega_2-\omega_i)\delta(\omega_2+\omega_j)\delta(\omega_2-\omega_k) - \tfrac{1}{16}\delta(\omega_2+\omega_i)\delta(\omega_2+\omega_j)\delta(\omega_2-\omega_k) \\
&-\tfrac{1}{16}\delta(\omega_3+\omega_i)\delta(\omega_3-\omega_j)\delta(\omega_3-\omega_k) - \tfrac{1}{16}\delta(\omega_3-\omega_i)\delta(\omega_3+\omega_j)\delta(\omega_3-\omega_k) \\
&-\tfrac{1}{16}\delta(\omega_3+\omega_i)\delta(\omega_3+\omega_j)\delta(\omega_3-\omega_k) - \tfrac{1}{16}\delta(\omega_4+\omega_i)\delta(\omega_4-\omega_j)\delta(\omega_4-\omega_k) \\
&-\tfrac{1}{16}\delta(\omega_4-\omega_i)\delta(\omega_4+\omega_j)\delta(\omega_4-\omega_k) - \tfrac{1}{16}\delta(\omega_4+\omega_i)\delta(\omega_4+\omega_j)\delta(\omega_4-\omega_k) \\
&-\tfrac{1}{16}\delta(\omega_1-\omega_i)\delta(\omega_1-\omega_j)\delta(\omega_1+\omega_k) - \tfrac{1}{16}\delta(\omega_1+\omega_i)\delta(\omega_1-\omega_j)\delta(\omega_1+\omega_k) \\
&-\tfrac{1}{16}\delta(\omega_1-\omega_i)\delta(\omega_1+\omega_j)\delta(\omega_1+\omega_k) - \tfrac{1}{16}\delta(\omega_2-\omega_i)\delta(\omega_2-\omega_j)\delta(\omega_2+\omega_k) \\
&-\tfrac{1}{16}\delta(\omega_2+\omega_i)\delta(\omega_2-\omega_j)\delta(\omega_2+\omega_k) - \tfrac{1}{16}\delta(\omega_2-\omega_i)\delta(\omega_2+\omega_j)\delta(\omega_2+\omega_k) \\
&-\tfrac{1}{16}\delta(\omega_3-\omega_i)\delta(\omega_3-\omega_j)\delta(\omega_3+\omega_k) - \tfrac{1}{16}\delta(\omega_3+\omega_i)\delta(\omega_3-\omega_j)\delta(\omega_3+\omega_k) \\
&-\tfrac{1}{16}\delta(\omega_3-\omega_i)\delta(\omega_3+\omega_j)\delta(\omega_3+\omega_k) - \tfrac{1}{16}\delta(\omega_4-\omega_i)\delta(\omega_4-\omega_j)\delta(\omega_4+\omega_k) \\
&-\tfrac{1}{16}\delta(\omega_4+\omega_i)\delta(\omega_4-\omega_j)\delta(\omega_4+\omega_k) - \tfrac{1}{16}\delta(\omega_4-\omega_i)\delta(\omega_4+\omega_j)\delta(\omega_4+\omega_k)
\end{aligned}
\tag{2.32}
$$

Note that $S_{xxxx}(\omega_i, \omega_j, \omega_k)$ has peaks at $(\pm\omega_m, \pm\omega_m, \pm\omega_m,)$ with the exception of $(\omega_m, \omega_m, \omega_m,)$ and $(-\omega_m, -\omega_m, -\omega_m,)$, where $m = 1, 2, 3, 4$. Thus, the auto-trispectrum of $x(t)$ as defined in equation 2.27, is zero in the first octant where all frequencies are positive and for the cases where the phases of all four frequency components are random.

For the case where ϕ_1, ϕ_2, and ϕ_3 are independent and uniformly distributed over $[0, 2\pi]$ and where

$$\phi_4 = \phi_1 + \phi_2 + \phi_3 \tag{2.33}$$

The substitution of equation 2.25 into equation 2.31 and application of equations 2.29 and 2.33 yield the fourth-order cumulant

$$
\begin{aligned}
&C_4(\tau_1, \tau_2, \tau_3) = \\
&-\tfrac{1}{8}cos[(\tau_1 - \tau_2 - \tau_3)\omega_1] - \tfrac{1}{8}cos[(\tau_1 + \tau_2 - \tau_3)\omega_1] - \tfrac{1}{8}cos[(\tau_1 - \tau_2 + \tau_3)\omega_1] \\
&-\tfrac{1}{8}cos[(\tau_1 - \tau_2 - \tau_3)\omega_2] - \tfrac{1}{8}cos[(\tau_1 + \tau_2 - \tau_3)\omega_2] - \tfrac{1}{8}cos[(\tau_1 - \tau_2 + \tau_3)\omega_2] \\
&-\tfrac{1}{8}cos[(\tau_1 - \tau_2 - \tau_3)\omega_3] - \tfrac{1}{8}cos[(\tau_1 + \tau_2 - \tau_3)\omega_3] - \tfrac{1}{8}cos[(\tau_1 - \tau_2 + \tau_3)\omega_3] \\
&+\tfrac{1}{8}cos[\tau_1\omega_1 + \tau_2\omega_2 + \tau_3\omega_3] + \tfrac{1}{8}cos[\tau_1\omega_1 + \tau_3\omega_2 + \tau_2\omega_3] + \tfrac{1}{8}cos[\tau_2\omega_1 + \tau_1\omega_2 + \tau_3\omega_3] \\
&+\tfrac{1}{8}cos[\tau_2\omega_1 + \tau_3\omega_2 + \tau_1\omega_3] + \tfrac{1}{8}cos[\tau_3\omega_1 + \tau_1\omega_2 + \tau_2\omega_3] + \tfrac{1}{8}cos[\tau_3\omega_1 + \tau_2\omega_2 + \tau_1\omega_3] \\
&+\tfrac{1}{8}cos[\tau_1\omega_1 - \tau_3\omega_1 + \tau_1\omega_2 - \tau_2\omega_2 + \tau_1\omega_3] + \tfrac{1}{8}cos[\tau_1\omega_1 - \tau_2\omega_1 + \tau_1\omega_2 - \tau_3\omega_2 + \tau_1\omega_3] \\
&+\tfrac{1}{8}cos[\tau_1\omega_1 - \tau_2\omega_1 - \tau_2\omega_2 + \tau_3\omega_2 - \tau_2\omega_3] + \tfrac{1}{8}cos[\tau_2\omega_1 - \tau_3\omega_1 - \tau_1\omega_2 + \tau_2\omega_2 + \tau_2\omega_3] \\
&+\tfrac{1}{8}cos[\tau_2\omega_1 - \tau_3\omega_1 + \tau_1\omega_2 - \tau_3\omega_2 - \tau_3\omega_3] + \tfrac{1}{8}cos[\tau_1\omega_1 - \tau_3\omega_1 + \tau_2\omega_2 - \tau_3\omega_2 - \tau_3\omega_3] \\
&+\tfrac{1}{8}cos[\tau_1\omega_1 - \tau_2\omega_1 + \tau_1\omega_2 + \tau_1\omega_3 - \tau_3\omega_3] + \tfrac{1}{8}cos[\tau_1\omega_1 - \tau_3\omega_1 + \tau_1\omega_2 + \tau_1\omega_3 - \tau_2\omega_3] \\
&+\tfrac{1}{8}cos[\tau_2\omega_1 - \tau_3\omega_1 + \tau_2\omega_2 + \tau_2\omega_3 - \tau_1\omega_3] + \tfrac{1}{8}cos[\tau_2\omega_1 - \tau_2\omega_1 - \tau_2\omega_2 + \tau_3\omega_3 - \tau_2\omega_3] \\
&+\tfrac{1}{8}cos[\tau_2\omega_2 - \tau_3\omega_1 - \tau_3\omega_2 + \tau_1\omega_3 - \tau_3\omega_3] + \tfrac{1}{8}cos[\tau_1\omega_1 - \tau_3\omega_1 - \tau_3\omega_2 + \tau_2\omega_3 - \tau_3\omega_3] \\
&+\tfrac{1}{8}cos[\tau_1\omega_1 + \tau_1\omega_2 - \tau_3\omega_2 + \tau_1\omega_3 - \tau_2\omega_3] + \tfrac{1}{8}cos[\tau_1\omega_1 + \tau_1\omega_2 - \tau_2\omega_2 + \tau_1\omega_3 - \tau_3\omega_3] \\
&+\tfrac{1}{8}cos[\tau_2\omega_1 + \tau_2\omega_2 - \tau_1\omega_2 + \tau_2\omega_2 - \tau_3\omega_3] + \tfrac{1}{8}cos[\tau_2\omega_1 + \tau_2\omega_2 - \tau_3\omega_2 + \tau_2\omega_3 - \tau_1\omega_3] \\
&+\tfrac{1}{8}cos[\tau_3\omega_1 + \tau_3\omega_2 - \tau_1\omega_2 + \tau_3\omega_3 - \tau_2\omega_3] + \tfrac{1}{8}cos[\tau_3\omega_1 + \tau_3\omega_2 - \tau_2\omega_2 + \tau_3\omega_3 - \tau_1\omega_3] \\
&-\tfrac{1}{8}cos[(\tau_1 - \tau_2 - \tau_3)(\omega_1 + \omega_2 + \omega_3)] - \tfrac{1}{8}cos[(\tau_1 + \tau_2 - \tau_3)(\omega_1 + \omega_2 + \omega_3)] \\
&-\tfrac{1}{8}cos[(\tau_1 - \tau_2 + \tau_3)(\omega_1 + \omega_2 + \omega_3)]
\end{aligned}
\tag{2.34}
$$

The third-order Fourier transform of equation 2.34, i.e. the auto-trispectrum of $x(t)$ is then given by

$$
\begin{aligned}
&S_{xxxx}(\omega_i,\omega_j,\omega_k) = \\
&-\tfrac{1}{16}\delta(\omega_1+\omega_i)\delta(\omega_1+\omega_j)\delta(\omega_1-\omega_k) - \tfrac{1}{16}\delta(\omega_1+\omega_i)\delta(\omega_1-\omega_j)\delta(\omega_1+\omega_k) \\
&-\tfrac{1}{16}\delta(\omega_1+\omega_i)\delta(\omega_1-\omega_j)\delta(\omega_1-\omega_k) - \tfrac{1}{16}\delta(\omega_1-\omega_i)\delta(\omega_1+\omega_j)\delta(\omega_1+\omega_k) \\
&-\tfrac{1}{16}\delta(\omega_1-\omega_i)\delta(\omega_1+\omega_j)\delta(\omega_1-\omega_k) - \tfrac{1}{16}\delta(\omega_1-\omega_i)\delta(\omega_1-\omega_j)\delta(\omega_1+\omega_k) \\
&-\tfrac{1}{16}\delta(\omega_2+\omega_i)\delta(\omega_2+\omega_j)\delta(\omega_2-\omega_k) - \tfrac{1}{16}\delta(\omega_2+\omega_i)\delta(\omega_2-\omega_j)\delta(\omega_2+\omega_k) \\
&-\tfrac{1}{16}\delta(\omega_2+\omega_i)\delta(\omega_2-\omega_j)\delta(\omega_2-\omega_k) - \tfrac{1}{16}\delta(\omega_2-\omega_i)\delta(\omega_2+\omega_j)\delta(\omega_2+\omega_k) \\
&-\tfrac{1}{16}\delta(\omega_2-\omega_i)\delta(\omega_2+\omega_j)\delta(\omega_2-\omega_k) - \tfrac{1}{16}\delta(\omega_2-\omega_i)\delta(\omega_2-\omega_j)\delta(\omega_2+\omega_k) \\
&-\tfrac{1}{16}\delta(\omega_3+\omega_i)\delta(\omega_3+\omega_j)\delta(\omega_3-\omega_k) - \tfrac{1}{16}\delta(\omega_3+\omega_i)\delta(\omega_3-\omega_j)\delta(\omega_3+\omega_k) \\
&-\tfrac{1}{16}\delta(\omega_3+\omega_i)\delta(\omega_3-\omega_j)\delta(\omega_3-\omega_k) - \tfrac{1}{16}\delta(\omega_3-\omega_i)\delta(\omega_3+\omega_j)\delta(\omega_3+\omega_k) \\
&-\tfrac{1}{16}\delta(\omega_3-\omega_i)\delta(\omega_3+\omega_j)\delta(\omega_3-\omega_k) - \tfrac{1}{16}\delta(\omega_3-\omega_i)\delta(\omega_3-\omega_j)\delta(\omega_3+\omega_k) \\
&+\tfrac{1}{16}\delta(\omega_1-\omega_i)\delta(\omega_2-\omega_j)\delta(\omega_3-\omega_k) + \tfrac{1}{16}\delta(\omega_1-\omega_i)\delta(\omega_3-\omega_j)\delta(\omega_2-\omega_k) \\
&+\tfrac{1}{16}\delta(\omega_2-\omega_i)\delta(\omega_1-\omega_j)\delta(\omega_3-\omega_k) + \tfrac{1}{16}\delta(\omega_2-\omega_i)\delta(\omega_3-\omega_j)\delta(\omega_1-\omega_k) \\
&+\tfrac{1}{16}\delta(\omega_3-\omega_i)\delta(\omega_1-\omega_j)\delta(\omega_2-\omega_k) + \tfrac{1}{16}\delta(\omega_3-\omega_i)\delta(\omega_2-\omega_j)\delta(\omega_1-\omega_k) \\
&+\tfrac{1}{16}\delta(\omega_1+\omega_i)\delta(\omega_2+\omega_j)\delta(\omega_3+\omega_k) + \tfrac{1}{16}\delta(\omega_1+\omega_i)\delta(\omega_3+\omega_j)\delta(\omega_2+\omega_k) \\
&+\tfrac{1}{16}\delta(\omega_2+\omega_i)\delta(\omega_1+\omega_j)\delta(\omega_3+\omega_k) + \tfrac{1}{16}\delta(\omega_2+\omega_i)\delta(\omega_3+\omega_j)\delta(\omega_1+\omega_k) \\
&+\tfrac{1}{16}\delta(\omega_3+\omega_i)\delta(\omega_1+\omega_j)\delta(\omega_2+\omega_k) + \tfrac{1}{16}\delta(\omega_3+\omega_i)\delta(\omega_2+\omega_j)\delta(\omega_1+\omega_k) \\
&-\tfrac{1}{16}\delta(\omega_1+\omega_2+\omega_3+\omega_i)\delta(\omega_1+\omega_2+\omega_3+\omega_j)\delta(\omega_1+\omega_2+\omega_3-\omega_k) \\
&-\tfrac{1}{16}\delta(\omega_1+\omega_2+\omega_3+\omega_i)\delta(\omega_1+\omega_2+\omega_3-\omega_j)\delta(\omega_1+\omega_2+\omega_3+\omega_k) \\
&-\tfrac{1}{16}\delta(\omega_1+\omega_2+\omega_3+\omega_i)\delta(\omega_1+\omega_2+\omega_3-\omega_j)\delta(\omega_1+\omega_2+\omega_3-\omega_k) \\
&-\tfrac{1}{16}\delta(\omega_1+\omega_2+\omega_3-\omega_i)\delta(\omega_1+\omega_2+\omega_3+\omega_j)\delta(\omega_1+\omega_2+\omega_3+\omega_k) \\
&-\tfrac{1}{16}\delta(\omega_1+\omega_2+\omega_3-\omega_i)\delta(\omega_1+\omega_2+\omega_3+\omega_j)\delta(\omega_1+\omega_2+\omega_3-\omega_k) \\
&-\tfrac{1}{16}\delta(\omega_1+\omega_2+\omega_3-\omega_i)\delta(\omega_1+\omega_2+\omega_3-\omega_j)\delta(\omega_1+\omega_2+\omega_3+\omega_k) \\
&+\tfrac{1}{16}\delta(\omega_1+\omega_2+\omega_3+\omega_i)\delta(\omega_1-\omega_j)\delta(\omega_2-\omega_k) \\
&+\tfrac{1}{16}\delta(\omega_1+\omega_2+\omega_3+\omega_i)\delta(\omega_2-\omega_j)\delta(\omega_1-\omega_k) \\
&+\tfrac{1}{16}\delta(\omega_1+\omega_2+\omega_3+\omega_i)\delta(\omega_2-\omega_j)\delta(\omega_3-\omega_k)
\end{aligned}
$$

$$
\begin{aligned}
&+\tfrac{1}{16}\delta(\omega_1+\omega_2+\omega_3+\omega_i)\delta(\omega_3-\omega_j)\delta(\omega_2-\omega_k)\\
&+\tfrac{1}{16}\delta(\omega_1+\omega_2+\omega_3+\omega_i)\delta(\omega_1-\omega_j)\delta(\omega_3-\omega_k)\\
&+\tfrac{1}{16}\delta(\omega_1+\omega_2+\omega_3+\omega_i)\delta(\omega_3-\omega_j)\delta(\omega_1-\omega_k)\\
&+\tfrac{1}{16}\delta(\omega_1+\omega_2+\omega_3-\omega_i)\delta(\omega_1+\omega_j)\delta(\omega_2+\omega_k)\\
&+\tfrac{1}{16}\delta(\omega_1+\omega_2+\omega_3-\omega_i)\delta(\omega_2+\omega_j)\delta(\omega_1+\omega_k)\\
&+\tfrac{1}{16}\delta(\omega_1+\omega_2+\omega_3-\omega_i)\delta(\omega_2+\omega_j)\delta(\omega_3+\omega_k)\\
&+\tfrac{1}{16}\delta(\omega_1+\omega_2+\omega_3-\omega_i)\delta(\omega_3+\omega_j)\delta(\omega_2+\omega_k)\\
&+\tfrac{1}{16}\delta(\omega_1+\omega_2+\omega_3-\omega_i)\delta(\omega_1+\omega_j)\delta(\omega_3+\omega_k)\\
&+\tfrac{1}{16}\delta(\omega_1+\omega_2+\omega_3-\omega_i)\delta(\omega_3+\omega_j)\delta(\omega_1+\omega_k)\\
&+\tfrac{1}{16}\delta(\omega_1+\omega_2+\omega_3+\omega_j)\delta(\omega_1-\omega_i)\delta(\omega_2-\omega_k)\\
&+\tfrac{1}{16}\delta(\omega_1+\omega_2+\omega_3+\omega_j)\delta(\omega_2-\omega_i)\delta(\omega_1-\omega_k)\\
&+\tfrac{1}{16}\delta(\omega_1+\omega_2+\omega_3+\omega_j)\delta(\omega_2-\omega_i)\delta(\omega_3-\omega_k)\\
&+\tfrac{1}{16}\delta(\omega_1+\omega_2+\omega_3+\omega_j)\delta(\omega_3-\omega_i)\delta(\omega_2-\omega_k)\\
&+\tfrac{1}{16}\delta(\omega_1+\omega_2+\omega_3+\omega_j)\delta(\omega_1-\omega_i)\delta(\omega_3-\omega_k)\\
&+\tfrac{1}{16}\delta(\omega_1+\omega_2+\omega_3+\omega_j)\delta(\omega_3-\omega_i)\delta(\omega_1-\omega_k)\\
&+\tfrac{1}{16}\delta(\omega_1+\omega_2+\omega_3-\omega_j)\delta(\omega_1+\omega_i)\delta(\omega_2+\omega_k)\\
&+\tfrac{1}{16}\delta(\omega_1+\omega_2+\omega_3-\omega_j)\delta(\omega_2+\omega_i)\delta(\omega_1+\omega_k)\\
&+\tfrac{1}{16}\delta(\omega_1+\omega_2+\omega_3-\omega_j)\delta(\omega_2+\omega_i)\delta(\omega_3+\omega_k)\\
&+\tfrac{1}{16}\delta(\omega_1+\omega_2+\omega_3-\omega_j)\delta(\omega_3+\omega_i)\delta(\omega_2+\omega_k)\\
&+\tfrac{1}{16}\delta(\omega_1+\omega_2+\omega_3-\omega_j)\delta(\omega_1+\omega_i)\delta(\omega_3+\omega_k)\\
&+\tfrac{1}{16}\delta(\omega_1+\omega_2+\omega_3-\omega_j)\delta(\omega_3+\omega_i)\delta(\omega_1+\omega_k)\\
&+\tfrac{1}{16}\delta(\omega_1+\omega_2+\omega_3+\omega_k)\delta(\omega_1-\omega_j)\delta(\omega_2-\omega_i)\\
&+\tfrac{1}{16}\delta(\omega_1+\omega_2+\omega_3+\omega_k)\delta(\omega_2-\omega_j)\delta(\omega_1-\omega_i)\\
&+\tfrac{1}{16}\delta(\omega_1+\omega_2+\omega_3+\omega_k)\delta(\omega_2-\omega_j)\delta(\omega_3-\omega_i)\\
&+\tfrac{1}{16}\delta(\omega_1+\omega_2+\omega_3+\omega_k)\delta(\omega_3-\omega_j)\delta(\omega_2-\omega_i)\\
&+\tfrac{1}{16}\delta(\omega_1+\omega_2+\omega_3+\omega_k)\delta(\omega_1-\omega_j)\delta(\omega_3-\omega_i)
\end{aligned}
\tag{2.35}
$$

$$+\tfrac{1}{16}\delta(\omega_1+\omega_2+\omega_3+\omega_k)\delta(\omega_3-\omega_j)\delta(\omega_1-\omega_i)$$
$$+\tfrac{1}{16}\delta(\omega_1+\omega_2+\omega_3-\omega_k)\delta(\omega_1+\omega_j)\delta(\omega_2+\omega_i)$$
$$+\tfrac{1}{16}\delta(\omega_1+\omega_2+\omega_3-\omega_k)\delta(\omega_2+\omega_j)\delta(\omega_1+\omega_i)$$
$$+\tfrac{1}{16}\delta(\omega_1+\omega_2+\omega_3-\omega_k)\delta(\omega_2+\omega_j)\delta(\omega_3+\omega_i)$$
$$+\tfrac{1}{16}\delta(\omega_1+\omega_2+\omega_3-\omega_k)\delta(\omega_3+\omega_j)\delta(\omega_2+\omega_i)$$
$$+\tfrac{1}{16}\delta(\omega_1+\omega_2+\omega_3-\omega_k)\delta(\omega_1+\omega_j)\delta(\omega_3+\omega_i)$$
$$+\tfrac{1}{16}\delta(\omega_1+\omega_2+\omega_3-\omega_k)\delta(\omega_3+\omega_j)\delta(\omega_1+\omega_i)$$

In the first octant, where all frequency components are positive, ($\omega_i > 0, \omega_j > 0, \omega_k > 0$), the trispectrum $S_{xxxx}(\omega_i, \omega_j, \omega_k)$ reduces to

$$\begin{aligned}
&S_{xxxx}(\omega_i,\omega_j,\omega_k) = \\
&+\tfrac{1}{16}\delta(\omega_1-\omega_i)\delta(\omega_2-\omega_j)\delta(\omega_3-\omega_k)+\tfrac{1}{16}\delta(\omega_1-\omega_i)\delta(\omega_3-\omega_j)\delta(\omega_2-\omega_k)\\
&+\tfrac{1}{16}\delta(\omega_2-\omega_i)\delta(\omega_1-\omega_j)\delta(\omega_3-\omega_k)+\tfrac{1}{16}\delta(\omega_2-\omega_i)\delta(\omega_3-\omega_j)\delta(\omega_1-\omega_k)\\
&+\tfrac{1}{16}\delta(\omega_3-\omega_i)\delta(\omega_1-\omega_j)\delta(\omega_2-\omega_k)+\tfrac{1}{16}\delta(\omega_3-\omega_i)\delta(\omega_2-\omega_j)\delta(\omega_1-\omega_k)
\end{aligned} \tag{2.36}$$

Note that $S_{xxxx}(\omega_i, \omega_j, \omega_k)$ has peaks in the first octant at $(\omega_i, \omega_j, \omega_k)$, where i, j, k take all permutations of $(1, 2, 3)$. Therefore, the phase coupling between four frequency components is identifiable through the trispectrum. Because this coupling is usually generated by cubic nonlinearity, the trispectrum could be used to identify cubic nonlinearities in time series.

2.2.3 Application of the Trispectrum to Analytic Signals

To demonstrate how the auto-trispectrum can be used to detect cubic phase coupling, we consider two processes. Each of these processes consists of four frequency components that satisfy the frequency summation rule $f_4 =$

$f_1 + f_2 + f_3$. The first process, described by $x_1(t)$, is given by

$$\begin{aligned} x_1(t) &= cos(2 * pi * 0.1 * t + \phi_1) + cos(2 * pi * 0.2 * t + \phi_2) \\ &+cos(2 * pi * 0.35 * t + \phi_3) + cos(2 * pi * 0.65 * t + \phi_4) \end{aligned} \tag{2.37}$$

where ϕ_1,ϕ_2, and ϕ_3 are independent and uniformly distributed random variables, and $\phi_4 = \phi_1 + \phi_2 + \phi_3$. The second process, $x_2(t)$, is given by

$$\begin{aligned} x_2(t) &= cos(2 * pi * 0.1 * t + \phi_1) + cos(2 * pi * 0.2 * t + \phi_2) \\ &+cos(2 * pi * 0.35 * t + \phi_3) + cos(2 * pi * 0.65 * t + \phi_4) \end{aligned} \tag{2.38}$$

where ϕ_1, ϕ_2, ϕ_3, and ϕ_4 are independent and uniformly distributed random variables.

Figure 2.1 shows the power spectra of both processes. Obviously, both spectra have the same frequency components. It is also clear that the power spectra does not give any information about the difference in the phase relation. Figure 2.2 shows a comparison of auto-trispectra for time series $x_1(t)$ and $x_2(t)$. The auto-trispectra were calculated using 10 data segments with 256 samples for each segment. In the figure, all values above 0.1 of the maximum value of both auto-trispectra are indicated with circles. It is clearly shown that the auto-trispectrum for the signal with cubic phase coupling, $x_1(t)$, has peaks at (0.1, 0.2, 0.35); the auto-trispectrum for the signal without cubic phase coupling, $x_2(t)$, does not show any peak in the figure. This shows that the trispectrum can be applied to detect cubic phase couplings, which is usually a result of cubic nonlinearities.

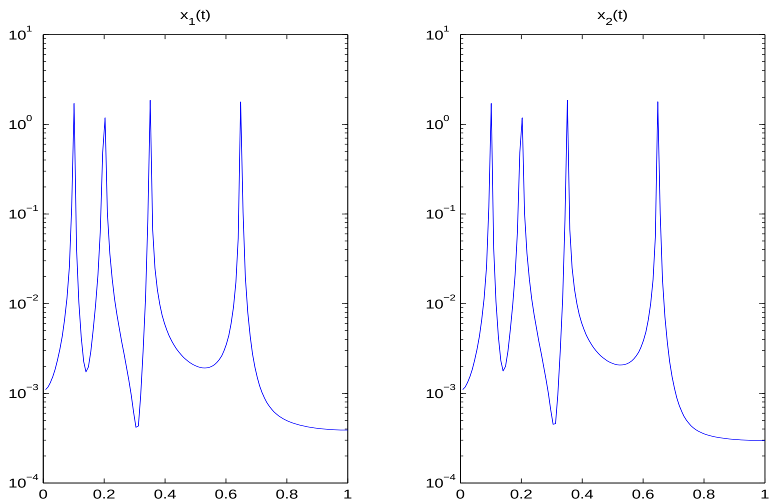

Figure 2.1: Comparison of power spectra for the time series with cubic phase couling and the time series with no cubic phase coupling.

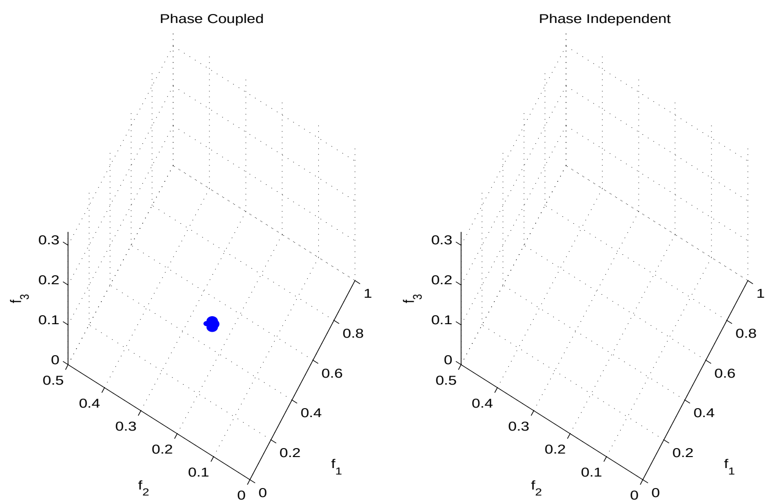

Figure 2.2: Comparison of auto-trispectra for the time series with cubic phase couling and the time series with no cubic phase coupling.

2.3 Data Analysis

Methods developed for the parametric identification in the reduced-order models for the lift and drag over oscillating cylinders are verified by application to data obtained from RANS simulation of the flow field. The data was obtained from Dr. Farouk Owis, previously a Research Associate in the ESM Department. A brief description of the turbulence closure model, the discretization of the different terms in the governing equation and the boundary conditions is given in Nayfeh, Owis and Hajj (2003). The power spectra presented in this work were calculated using 4 segments each consisting of 512 data points. The same number of points was used in the bispectra calculations. The trispectra estimates were obtained by using 8 segments each consisting of 256 data points.

Chapter 3

Drag Modeling on a Stationary Circular Cylinder – a Short Note

Nayfeh, Owis and Hajj(2003)[16] showed that the lift coefficient on a stationary cylinder can be represented by the van der Pol equation

$$\ddot{l} + \omega_s^2 l^2 - \mu_v \dot{l} + \alpha_v l^2 \dot{l} = 0 \tag{3.1}$$

and that the oscillating component of the drag is proportional to $l\dot{l}$, i.e.

$$d = d_m - \frac{k_1}{a_1^2 \omega_s} l\dot{l} \tag{3.2}$$

In this chapter, an improved model is presented. A linear term is added to account for observed linear coupling between the lift and drag at the vortex shedding frequency component and its third harmonic. Additionally, it is determined that the quadratic relation between the lift and drag is given by l^2.

3.1 Parametric Identification

The spectra of the lift and drag coefficients on a stationary cylinder at $Re = 10,000$ are shown in figures 3.1 and 3.2. The spectrum of the lift coefficient shows three peaks at the shedding frequency, ω_s, and its third and fifth harmonics, $3\omega_s$ and $5\omega_s$. The peak at the votex shedding frequency is relatively wide when compared to the others. Additionally, the peak at the third harmonic is about three orders of magnitude (in terms of power) lower than the peak at the vortex shedding frequency. The peak at the fifth harmonic is about four orders of magnitude lower. It should be noted here that the value for ω_s is larger than the reported value of about 0.2Hz. This is most likely due to the fact that the RANS flow simulations are two-dimensional. The spectrum of the drag coefficient shows that the drag has two major peaks, namely, at the second and fourth harmonics of the vortex shedding frequency, ω_s. The peak at the second harmonic is relatively wide and is about one order of magnitude larger than the peak of the fourth harmonic. This suggests that the most important coupling between the drag and lift coefficients is quadratic. The smaller peaks noted at the vortex shedding frequency ω_s and the third and fifth harmonic suggest the possibility of linear coherence of these components.

To determine the extent of coupling between ω_s in the lift time series and $2\omega_s$ in the drag time series, the cross-bispectrum between all pairs of frequency components in the lift that have a nonlinear relation with their sum or difference frequency component in the drag is estimated. The results are shown in Figure 3.3. The high value of cross-bispectrum at the frequency pair (ω_s, ω_s) shows that the second harmonic in the drag coefficient is quadratically related to the shedding frequency in the lift time series. This fact suggests that the drag is a quadratic function of the lift; that is, the drag is proportional to either l^2, $\dot{l}^2$, or $l\dot{l}$. The form of this dependence can be determined from the phase relation, $\phi_{drag}(2\omega_s) - 2\phi_{lift}(\omega_s)$. As shown by Hajj et al (1993)[21], this phase can be determined from the phase of the cross-bispectrum. This phase, along with the magnitude of the cross-bispectrum, is shown in Table 3.1. Because the phase of the cross-bispectrum between the vortex shedding frequency component in the lift and its second harmonic in the drag is close to $-\frac{\pi}{2}$, it is determined that the drag must be proportional to l^2.

Because the drag force contains a mean component and, as shown above, is proportional to l^2, it is modeled as

$$d = (d_m - k_1) + \frac{2k_1}{a_1^2} l^2 \tag{3.3}$$

where d_m is the mean drag and can be obtained independently as a mean value from the time series of the drag. The coefficient a_1 is the amplitude of the vortex shedding frequency component in the lift and can be determined from the spectrum shown in figure 3.1. The coefficient k_1 is the amplitude of the second harmonic, $2\omega_s$ in the drag spectrum. This analysis yields the values of 1.56 for the mean drag coefficient, d_m, and 0.06 for k_1. The estimated value of a_1 is 1.773.

3.2 Validation

The initial validation of the above model and parameters for the drag was performed by using the lift coefficient data and equation 3.3 to calculate the drag coefficient. The initial comparison of the RANS simulated and the modeled time series showed good agreement. However, upon a comparative analysis of the different spectral moments of the lift and drag time series and their linear coherence and nonlinear coupling, it was observed that there is a high level of linear coherence between the drag and lift at the vortex shedding frequency and its third harmonic components. Consequently, because the drag model, as presented above, could not account for this coherence, the drag-lift relation was revised to the following form

$$d = (d_m - k_1) + \frac{2k_1}{a_1^2} l^2 + k_2 l \tag{3.4}$$

where the coefficient k_2 is introduced to account for the linear coupling between the lift and drag coefficients. Dividing the spectral amplitudes of the lift and drag coefficients at the shedding frequency yields a value of -0.0045 for k_2. It should be noted that the value of k_2 is relatively small in comparison to d_m and k_1. Additionally, simulations at different Reynolds numbers yield smaller values for k_2.

To verify the drag coefficient model given in 3.4, we extend the analysis to validate the physics of the simulated and modeled lift and drag coefficients. Specifically, we compare the power spectra & linear coherence, and bispectra & bicoherence. Figure 3.4 shows a comparison of the RANS simulated and modeled time series. The results clearly show that the proposed model, along with the identified parameters, correctly predict the amplitude variations.

Table 3.1: Lift-drag cross-bispectrum for the stationary cylinder - amplitude and phase

$Re\#$	10000
$f_1(Hz)$	0.2344
$f_2(Hz)$	0.2344
Amplitude	0.2331
Phase(rad)	-1.533

This is further confirmed by the comparison of the spectra of the two time series as shown in figure 3.5. The results clearly show accurate predictions of the amplitudes of the dominant peaks at $2\omega_s$ and $4\omega_s$ and of the peaks that are linearly related to the lift at ω_s and $3\omega_s$. The comparison of the linear coherence between the vortex shedding frequency and its harmonic in the RANS simulated and modeled time series, presented in figure 3.6, shows that all linear couplings are accounted for in the model represented by equation 3.4. The cross-bispectral and bicoherence, presented respectively in figure 3.7 and 3.8, show that the governing quadratic couplings in both time series are the same. These comparisons show that the desired model contains all linear and nonlinear relations between the lift and drag coefficients.

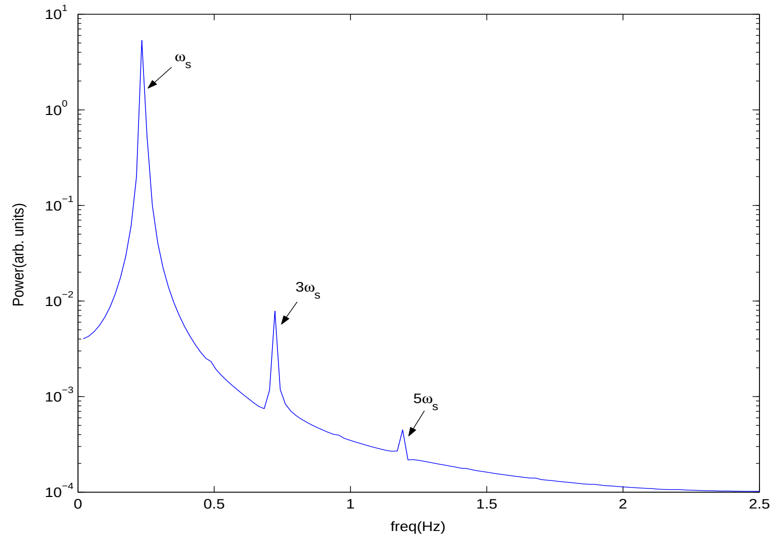

Figure 3.1: Power spectrum of the lift coefficient on the stationary cylinder for $Re = 10000$

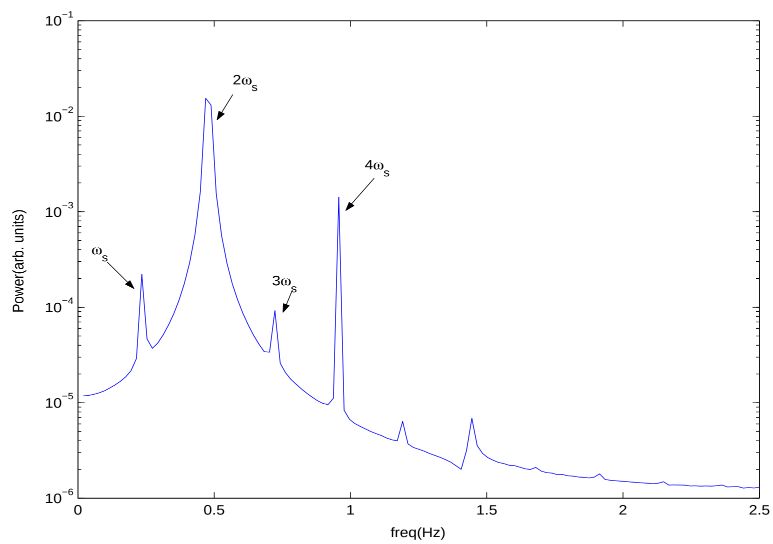

Figure 3.2: Power spectrum of the drag coefficient on the stationary cylinder for $Re = 10000$

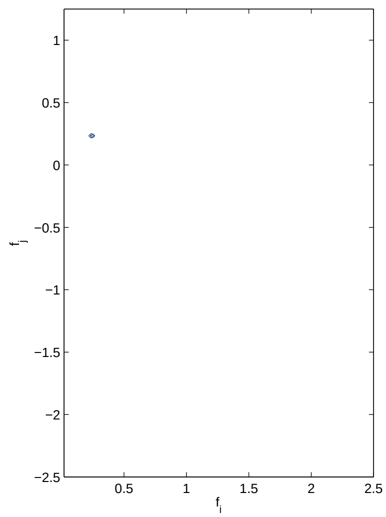

Figure 3.3: Cross-bispectrum of the lift and drag coefficients on the stationary cylinder for $Re = 10000$

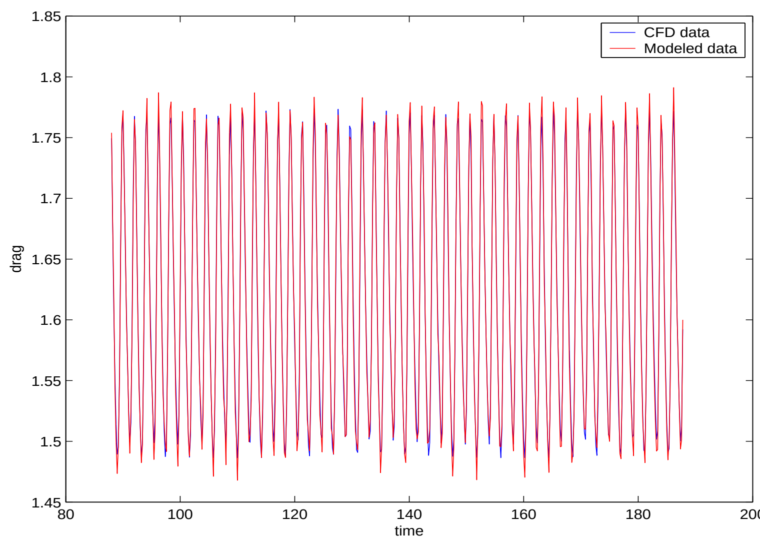

Figure 3.4: Comparison of RANS simulated and modeled time series of the drag coefficient on the stationary cylinder for $Re = 10000$

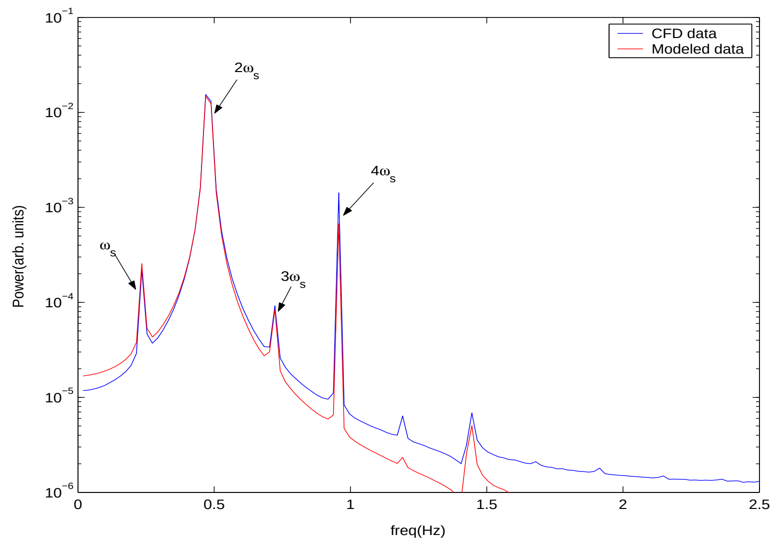

Figure 3.5: Comparison of power spectra of the RANS simulated and modeled drag coefficient on the stationary cylinder for $Re = 10000$

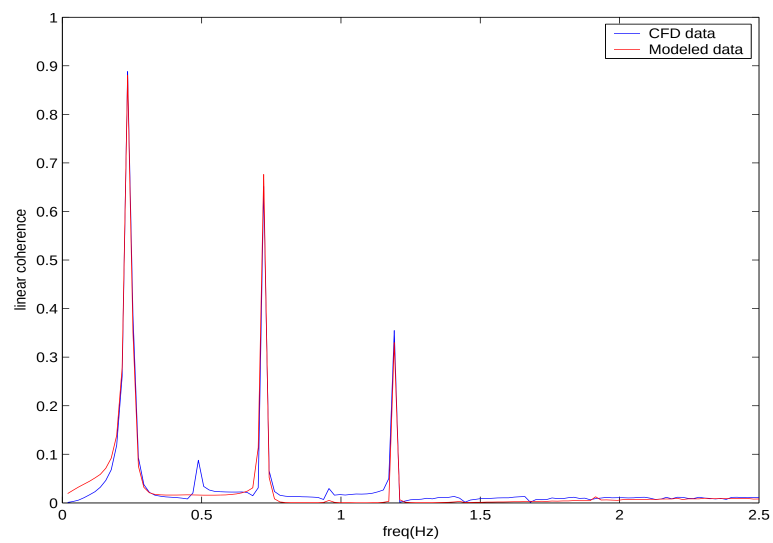

Figure 3.6: Comparison of linear coherence between the lift and drag coefficients on the stationary cylinder in the RANS simulated and modeled time series for $Re = 10000$

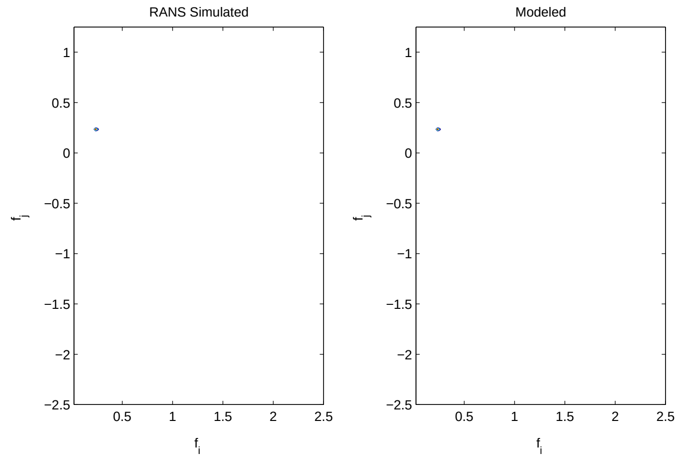

Figure 3.7: Comparison of cross-bispectrum between the lift and drag coefficients on the stationary cylinder in the RANS simulated and modeled time series for $Re = 10000$

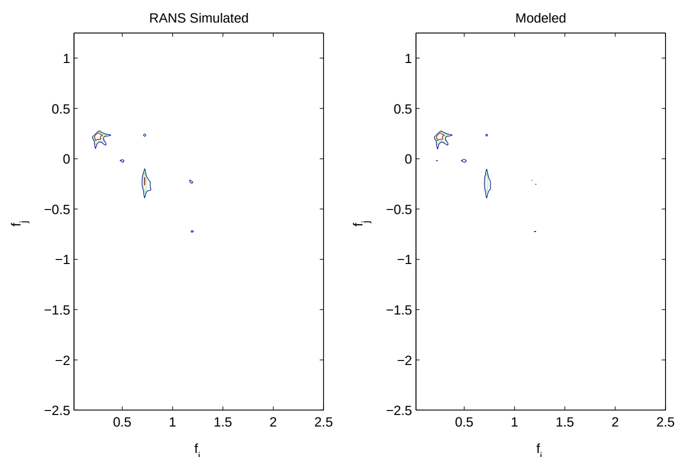

Figure 3.8: Comparison of cross-bicoherence between the lift and drag coefficients on the stationary cylinder in the RANS simulated and modeled time series for $Re = 10000$. Contour levels are set at 0.3, 0.6, 0.9

Chapter 4

Lift and Drag Modeling on a Forced Transversely Oscillating Cylinder

In this chapter, the lift and drag coefficients on a transversely oscillating cylinder under different forced conditions are modeled. The lift coefficient is modeled by the van der Pol oscillator that is externally excited by a harmonic function and described by

$$\ddot{l} + \omega_s^2 l^2 - \mu_v \dot{l} + \alpha_v l^2 \dot{l} = F cos(\Omega t + \tau_e) \tag{4.1}$$

where ω_s is the shedding frequency, μ_v and α_v represent the linear and nonlinear damping coefficients, and F and τ_e are respectively the amplitude and phase of the external harmonic force. Based on equation 3.3, the drag coefficient is modeled as

$$d = (d_m - c_1) + k_2(l + k_1 cos(\Omega t + \tau_e) + k_3 cos(\Omega t + 3\tau_e))^2 \tag{4.2}$$

where the cosine terms on the right hand side are added to account for the drag induced by the transverse motion of the cylinder.

Analytical procedures that combine the trispectrum and approximate solutions for determining the nonlinear and damping coefficients in the van der Pol equation under different excitation conditions are presented. These procedures include cases of soft and hard excitations with no resonance and the case of resonance. A procedure to determine the coefficients in the drag model and that makes use of the bispectrum is also presented. The dependence of these coefficients on the type of excitation is examined through the application of these procedures to lift and drag data on a cylinder oscillating in the transverse direction.

4.1 Modeling the Lift Coefficient under Different Excitation Conditions

4.1.1 Case of No Resonance with Soft Excitation

In this case, the excitation is assumed to be soft, and F is scaled as ϵF. μ_v and α_v are scaled as $\epsilon\mu_v$ and $\epsilon\alpha_v$ respectively. The forced van der Pol equation is then written as

$$\ddot{l} + \omega_s^2 l^2 - \epsilon\mu_v \dot{l} + \epsilon\alpha_v l^2 \dot{l} = \epsilon F cos(\Omega t + \tau_e) \tag{4.3}$$

Using the method of multiple scales[22][23], an analytical approximate solution is derived for equation 4.3 for the no-resonance condition, i.e. Ω is away from 0, ω, 3ω, and $\omega/3$. The approximate solution is of the form

$$l(t) \approx \quad acos(\omega_s t + \beta) + \frac{F}{\omega_s^2 - \Omega^2} cos(\Omega t + \tau_e) + \frac{a^3 \alpha_v}{32\omega_s} cos(3(\omega_s t + \beta) + \frac{\pi}{2}) \tag{4.4}$$

where the amplitude a and phase β are governed by

$$\begin{aligned} \dot{a} &= \frac{\mu_v}{2} a - \frac{\alpha_v}{8} a^3 \\ \dot{\beta} &= 0 \end{aligned} \tag{4.5}$$

Under steady-state oscillations, a and β are constants and the solution given in equation 4.4 represents a periodic motion which can be written in complex form as

$$\begin{aligned} l(t) \approx \quad & \frac{a}{2}\{e^{i(\omega_s t+\beta)} + e^{-i(\omega_s t+\beta)}\} + \frac{F}{2(\omega_s^2-\Omega^2)}\{e^{i(\Omega t+\tau_e)} + e^{-i(\Omega t+\tau_e)}\} \\ & + \frac{a^3\alpha_v}{64\omega_s}\{e^{3i(\omega_s t+\beta)+i\frac{\pi}{2}} + e^{-3i(\omega_s t+\beta)-i\frac{\pi}{2}}\} \end{aligned} \tag{4.6}$$

The Fourier transform of $l(t)$, $L(\omega)$, is given by

$$\begin{aligned} & L(\omega) \approx \\ & \frac{a}{2}\{e^{i\beta}\delta(\omega-\omega_s) + e^{-i\beta}\delta(\omega+\omega_s)\} + \frac{F}{2(\omega_s^2-\Omega^2)}\{e^{i\tau_e}\delta(\omega-\Omega) + e^{-i\tau_e}\delta(\omega+\Omega)\} \\ & + \frac{a^3\alpha_v}{64\omega_s}\{e^{3i\beta+i\frac{\pi}{2}}\delta(\omega-3\omega_s) + e^{-3i\beta-i\frac{\pi}{2}}\delta(\omega+3\omega_s)\} \end{aligned} \tag{4.7}$$

The solution thus contains components with three major frequency components at the shedding frequency ω_s, the excitation frequency Ω, and the third harmonic of the shedding frequency $3\omega_s$. The amplitudes and phases of these compoents are given by

$$L(\omega_s) = \frac{1}{2} a e^{i\beta} \tag{4.8}$$

$$L(\Omega) = \frac{F}{2(\omega_s^2 - \Omega^2)} e^{i\tau_e} \tag{4.9}$$

and

$$L(3\omega_s) = \frac{a^3 \alpha_v}{64\omega_s} e^{3i\beta + i\frac{\pi}{2}} \tag{4.10}$$

Based on the definition of the auto-trispectrum, which is given by

$$S_{llll}(\omega_k, \omega_l, \omega_m) = \lim_{T \to \infty} \frac{1}{T} E[L^*(\omega_k) L^*(\omega_l) L^*(\omega_m) L(\omega_k + \omega_l + \omega_m)] \tag{4.11}$$

one obtains, for the case where $\omega_k = \omega_l = \omega_m = \omega_s$, the auto-trispectrum

$$S_{llll}(\omega_s, \omega_s, \omega_s) \approx \frac{a^6 \alpha_v}{512\omega_s} e^{i\frac{\pi}{2}} \tag{4.12}$$

which relates the vortex shedding frequency and its third harmonic. It is important to note here that the amplitude of the trispectrum is dependent on the coefficient of cubic nonlinearity, α_v, and its phase establishes a phase relation, given by $\phi(3\omega_s) - 3\phi(\omega_s)$, between the vortex shedding frequency and its third harmonic that is equal to $\frac{\pi}{2}$. Thus, the amplitude of the trispectrum should be used to determine the coefficient of nonlinearity and its phase should be used to determine the validity of modeling the nonlinear system with a van der Pol equation.

The normalized auto-trispectrum, referred to as the auto-tricoherence, for ($\omega_k = \omega_l = \omega_m = \omega_s$) is defined by

$$t^2(\omega_s, \omega_s, \omega_s) \approx \frac{|S_{llll}(\omega_s, \omega_s, \omega_s)|^2}{|L(\omega_s)L(\omega_s)L(\omega_s)|^2 \, |L(3\omega_s)|^2} \tag{4.13}$$

A unit value for the auto-tricoherence indicates perfect cubic phase coupling between the vortex shedding frequency and its third harmonic. A zero value indicates no coupling. Any value between zero and one indicates partial coupling. Thus, the auto-tricoherence can be used to determine the extent of coupling in a time series and the validity of using the magnitude and phase of the trispectrum to model physical phenomenon. In this case, the value of the auto-tricoherence should be used as a measure of the level of confidence in the estimated value for α_v from the magnitude of the auto-trispectrum and in the departure of its phase from $\frac{\pi}{2}$.

The steady state value of the amplitude a can be obtained by setting $\dot{a} = 0$ in equation 4.5, i.e.

$$a = 2\sqrt{\frac{\mu_v}{\alpha_v}} \tag{4.14}$$

In order to determine the linear and nonlinear damping coefficients, and the excitation parameter in equation 4.3 from the amplitudes and phases of the Fourier components in the time series, the lift coefficient is re-written as

$$l(t) \approx \quad a_1 cos(\omega_s t + \beta) + a_2 cos(\Omega t + \tau_e) + a_3 cos(3(\omega_s t + \beta) + \tfrac{\pi}{2}) \tag{4.15}$$

Comparing equation 4.15 with equations 4.4 and applying equation 4.14, one obtains

$$\alpha_v = \frac{32\omega_s a_3}{a_1^3} \tag{4.16}$$

$$\mu_v = \frac{1}{4}\alpha_v a_1^2 \tag{4.17}$$

and

$$F = a_2(\omega_s^2 - \Omega^2) \tag{4.18}$$

Alternatively, and as explained above, the coefficient of nonlinearity α_v can be obtained from the magnitude of the auto-trispectrum. Rearranging equation 4.12, one obtains

$$\alpha_v = \frac{512\omega_s \left|S_{llll}(\omega_s, \omega_s, \omega_s)\right|}{a^6} \tag{4.19}$$

It is important to note here that under conditions where the excitation and response conditions contain a high level of noise, the auto-trispectrum should yield a better estimate for α_v. From the Fourier transform of $l(t)$ at frequency Ω, i.e. equation 4.9, the phase of the external force τ_e can be obtained as the phase of the $L(\Omega)$, i.e.

$$\tau_e = \Phi(L(\Omega)) \tag{4.20}$$

Results and Discussion

To show the applicability of the analysis presented above, the case of no resonance with soft excitation was obtained by forcing the cylinder to oscillate in the transverse direction with a frequency $\Omega = 0.1Hz$ at a nondimensional amplitude $\frac{y}{D} = 0.1$, where D is the cylinder's diameter. The Reynolds number was set at 10,000. The power spectrum of the resulting lift coefficient, obtained from the RANS siumlation, is shown in figure 4.1. The spectrum shows three peaks, at 0.1 Hz, the oscillation frequency, at 0.2393 Hz, the vortex shedding frequency and at the third harmonic of the vortex shedding frequency. The auto-trispectrum of the lift coefficient is presented in Figure 4.2. The plot clearly shows that the third harmonic is coupled with the vortex shedding frequency. In that plot, the three axes represent the interacting frequency components. The extent of interacting is represented by the size of the circle used to indicate the interaction. In the plot, all values above 10% of the maximum estimate level are indicated by the circles. The amplitude and phase of the autotrispectrum at the shedding frequency are given in Table 4.1. The phase is near $\pi/2$ which indicates, and based on the approximate solution and equation 4.57, that the van der Pol equation should be used to model the lift on the transversely oscillating cylinder.

The amplitude of the excitation and the different frequency components in the response along with the phase of the excitation are given in Table 4.2. Using equations 4.16, 4.17, 4.18, 4.19 and 4.20, the spectral parameters in Table 4.2 are used to obtain estimates for the parameters F, τ_e, μ_v and α_v in the forced van der Pol model as given in equation 4.1. Estimates of these parameters are given in Table 4.3. The closeness of the estimates of α_v obtained from equations 4.16 and 4.19 is noted. Additionally, the estimated values for the damping and nonlinear coefficients, μ_v and α_v for the cylinder undergoing transverse oscillations are about 5% lower than the values obtained for the stationary cylinder. This shows that these coefficients can be considered as independent of the cylinder's motions.

To verify the validity of the estimated parameters, the time series of the simulated response, obtained with RANS simulation, and the modeled response, obtained by integrating equation 4.1, are superimposed in figure

Table 4.1: Lift auto-trispectrum for the transversely oscillating cylinder - amplitude and phase (no resonance with soft excitation)

$\Omega(Hz)$	0.1
$\frac{y}{D}$	0.1
$f_1(Hz)$	0.2393
$f_2(Hz)$	0.2393
$f_3(Hz)$	0.2393
Amplitude	0.0166
Phase(rad)	1.7453

4.3. The results show a high level of agreement. A higher level of confidence in the proposed model and estimated parameters is obtained when comparing the power spectra and auto-trispectra given in figures 4.4 and 4.5. The comparison of the auto-power spectra shows that all peaks in the frequency distribution were correctly simulated. The auto-trispectra comparison shows that the same cubic nonlinearities exist in both time series. A comparison of the auto-tricoherence levels, presented in figure 4.6, shows that all involved nonlinear interactions identified from the RANS simulations are captured by the proposed model. In the auto-tricoherence plot circles are used to identify the levels of the auto-tricoherence with the larger circles indicating a higher level of interaction. In the plot, only the values above 0.1 are plotted.

Table 4.2: Lift spectral parameters for the transversely oscillating cylinder (no resonance wit soft excitation)

$\Omega(Hz)$	0.1
$\frac{y}{D}$	0.1
$f(Hz)$	0.2393
a_1	1.79
a_2	0.06
a_3	0.0463
$\Phi(L(\Omega))(rad)$	-0.778

Table 4.3: Lift model parameters in forced van der Pol equation (no resonance with soft excitation)

$\Omega(Hz)$	0.1
$\frac{y}{D}$	0.1
$f(Hz)$	0.2393
F	0.112
$\tau_e(rad)$	-0.778
μ_v	0.311
α_v from $L(3\omega_s)$	0.389
α_v from S_{llll}	0.3882

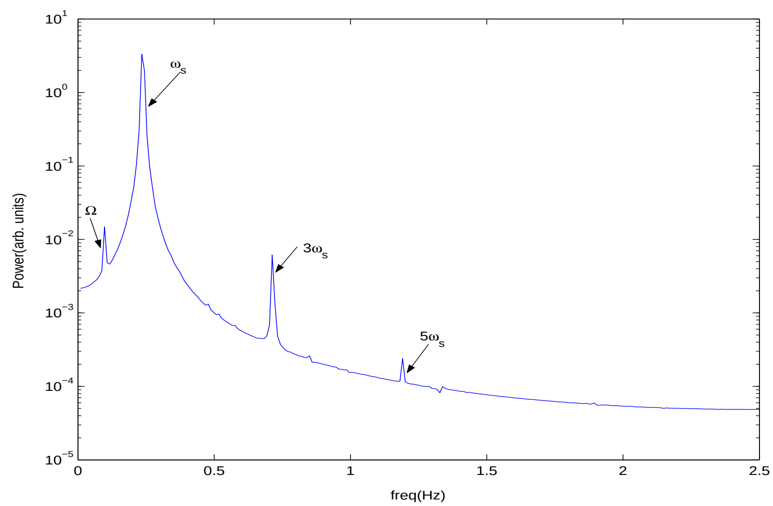

Figure 4.1: Power spectrum of the lift coefficient for the transversely oscillating cylinder at frequency $\Omega = 0.1Hz$ and amplitude $\frac{y}{D} = 0.1$

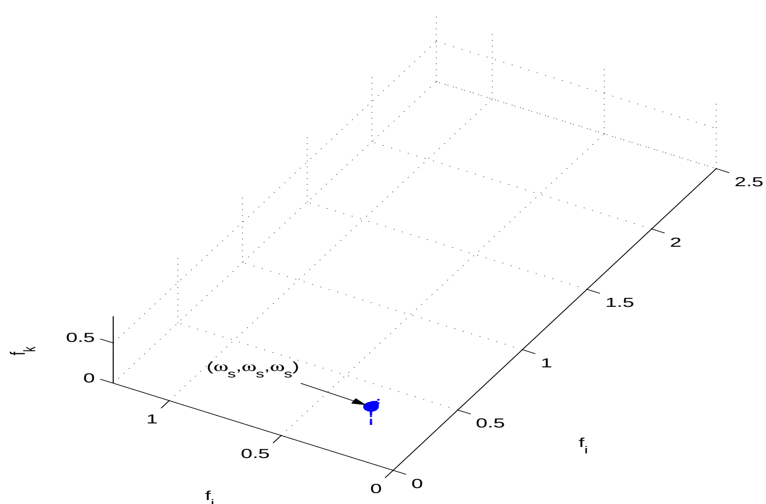

Figure 4.2: Auto-trispectrum of the lift coefficient for the transversely oscillating cylinder at frequency $\Omega = 0.1Hz$ and amplitude $\frac{y}{D} = 0.1$. Only values above 10% of maximum level are indicated.

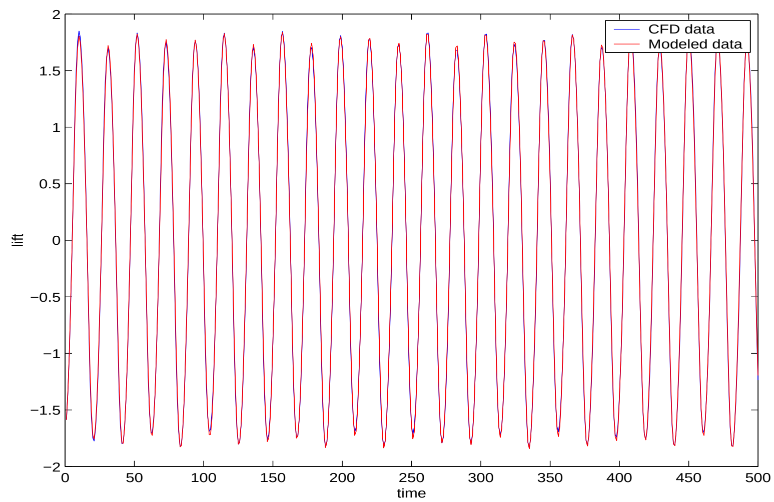

Figure 4.3: Comparison of RANS simulated and modeled time series of the lift coefficients for the transversely oscillating cylinder at frequency $\Omega = 0.1Hz$ and amplitude $\frac{y}{D} = 0.1$

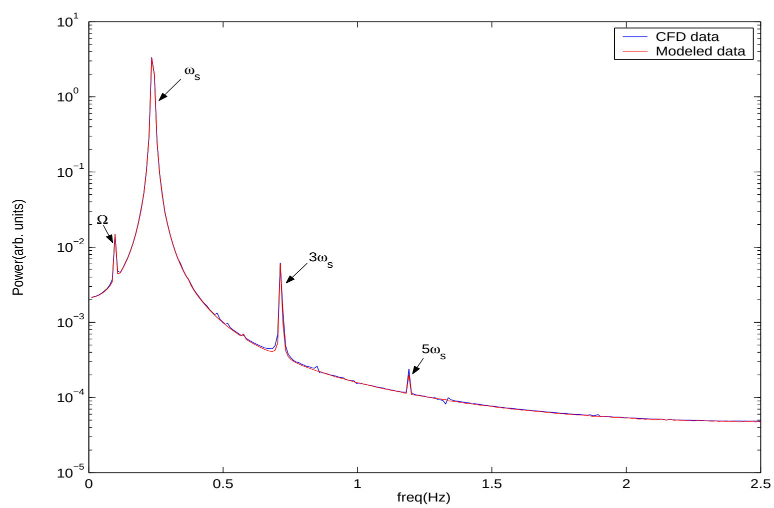

Figure 4.4: Comparison of power spectra of the RANS simulated and modeled lift coefficients for the transversely oscillating cylinder at frequency $\Omega = 0.1Hz$ and amplitude $\frac{y}{D} = 0.1$

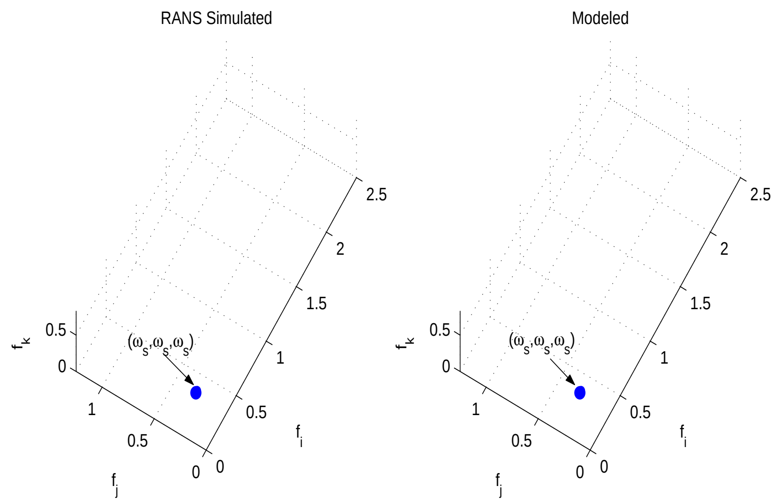

Figure 4.5: Comparison of auto-trispectra of the RANS simulated and modeled lift coefficients for the transversely oscillating cylinder at frequency $\Omega = 0.1Hz$ and amplitude $\frac{y}{D} = 0.1$. Levels plotted are 10% of the maximal value

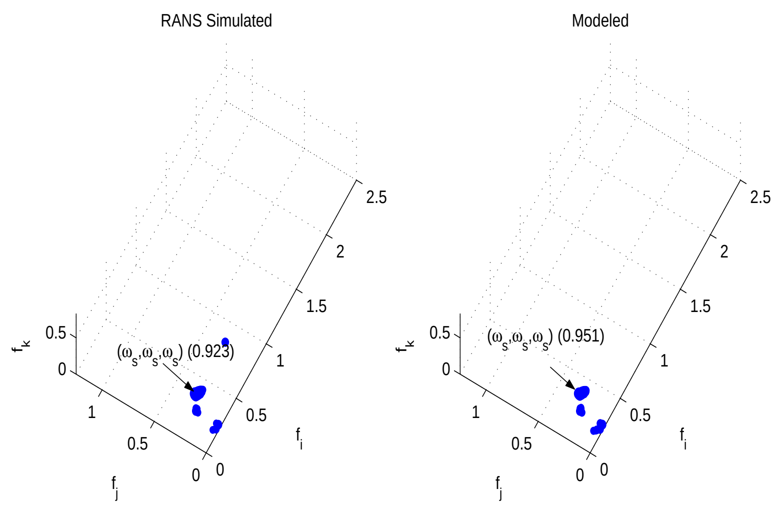

Figure 4.6: Comparison of auto-tricoherence of the RANS simulated and modeled lift coefficients for the transversely oscillating cylinder at frequency $\Omega = 0.1Hz$ and amplitude $\frac{y}{D} = 0.1$. Circles are used to identify coherence levels above 0.1 with the larger circles indicating a higher level of tricoherence.

4.1.2 Case of Primary Resonance

In this case, the excitation is also assumed to be soft, and F is scaled as ϵF. μ_v and α_v are scaled as $\epsilon\mu_v$ and $\epsilon\alpha_v$ respectively. The forced van der Pol equation is then written as

$$\ddot{l} + \omega_s^2 l^2 - \epsilon\mu_v \dot{l} + \epsilon\alpha_v l^2 \dot{l} = \epsilon F cos(\Omega t + \tau_e) \tag{4.21}$$

Using the method of multiple scales, an analytical approximate solution is derived for equation 4.21 for the following primary resonance condition

$$\Omega = \omega_s + \epsilon\sigma \tag{4.22}$$

where σ is the external detuning parameter. The approximate solution is then written as

$$l(t) \approx \quad acos(\Omega t + \tau_e - \gamma) + \tfrac{a^3\alpha_v}{32\omega_s} cos(3(\Omega + \tau_e - \gamma) + \tfrac{\pi}{2}) \tag{4.23}$$

where γ is given by

$$\gamma = \epsilon\sigma t + \tau_e - \beta \tag{4.24}$$

In equation 4.23, the amplitude a and phase γ are governed by

$$\begin{aligned} \dot{a} &= \tfrac{\mu_v}{2} a - \tfrac{\alpha_v}{8} a^3 + \tfrac{F}{2\omega_s} sin\gamma \\ a\dot{\gamma} &= a\sigma - \tfrac{F}{2\omega_s} cos\gamma \end{aligned} \tag{4.25}$$

An examination of the expression for γ reveals its dependency on the phase of excitation, τ_e and the phase of the response, β. When a and γ are constants in equation 4.25, i.e., for steady-state oscillations, the solution given in equation 4.23 represents a periodic motion which can be written in complex form as

$$\begin{aligned} l(t) \approx \;& \tfrac{a}{2}\{e^{i(\Omega t+\tau_e-\gamma)} + e^{-i(\Omega t+\tau_e-\gamma)}\} \\ & + \tfrac{a^3\alpha_v}{64\omega_s}\{e^{3i(\Omega t+\tau_e-\gamma)+i\frac{\pi}{2}} + e^{-3i(\Omega t+\tau_e-\gamma)-i\frac{\pi}{2}}\} \end{aligned} \tag{4.26}$$

The Fourier transform of $l(t)$ represented by $L(\omega)$ is then given by

$$\begin{aligned} L(\omega) \approx \;& \tfrac{a}{2}\{e^{i(\tau_e-\gamma)}\delta(\omega-\Omega) + e^{-i(\tau_e-\gamma)}\delta(\omega+\Omega)\} \\ & + \tfrac{a^3\alpha_v}{64\omega_s}\{e^{3i(\tau_e-\gamma)+i\frac{\pi}{2}}\delta(\omega-3\Omega) + e^{-3i(\tau_e-\gamma)-i\frac{\pi}{2}}\delta(\omega+3\Omega)\} \end{aligned} \tag{4.27}$$

Examining the expression for $L(\omega)$, it is noted that the solution contains components with frequencies at Ω and 3Ω. The amplitudes and phases of these components are given by

$$L(\Omega) = \frac{1}{2}ae^{i(\tau_e-\gamma)} \tag{4.28}$$

and

$$L(3\Omega) = \frac{a^3\alpha_v}{64\omega_s}e^{3i(\tau_e-\gamma)+i\frac{\pi}{2}} \tag{4.29}$$

The auto-trispectrum, defined as

$$S_{llll}(\omega_k,\omega_l,\omega_m) = \lim_{T\to\infty}\frac{1}{T}E[L^*(\omega_k)L_*(\omega_l)L_*(\omega_m)L(\omega_k+\omega_l+\omega_m)] \tag{4.30}$$

is then used to relate the two components, Ω and 3Ω. For $(\omega_k = \omega_l = \omega_m = \omega_s)$, this relation is written as

$$S_{llll}(\Omega,\Omega,\Omega) \approx \frac{a^6\alpha_v}{512\omega_s}e^{i\frac{\pi}{2}} \tag{4.31}$$

Equation 4.31 shows that the magnitude of the auto-trispectrum can be used to determine the coefficient of the cubic nonlinearity α_v. The phase of the auto-trispectrum $S_{llll}(\Omega, \Omega, \Omega)$, given by $\phi(3\Omega) - 3\phi(\Omega)$, and equal to $\frac{\pi}{2}$, should be used to establish the validity of the proposed model.

The auto-tricoherence for ($\omega_k = \omega_l = \omega_m = \Omega$) defined as

$$t^2(\Omega, \Omega, \Omega) \approx \frac{|S_{llll}(\Omega, \Omega, \Omega)|^2}{|L(\Omega)L(\Omega)L(\Omega)|^2 \, |L(3\Omega)|^2} \tag{4.32}$$

should be used to determine the extent of cubic coupling between the two frequency components Ω and 3Ω and its level should be used to establish a level of confidence in the estimated values of the magnitude and phase of the auto-trispectrum and any derived parameters. A high level of the auto-tricoherence indicates a high level of confidence in the reduced-order model and derived parameters.

For the forced van der Pol equation with primary resonance and soft excitation, the steady state value of amplitude a and phase γ can be obtained by setting $\dot{a} = 0$ and $\dot{\gamma} = 0$ in equation 4.25, i.e.

$$\begin{aligned} 0 &= \tfrac{\mu_v}{2} a - \tfrac{\alpha_v}{8} a^3 + \tfrac{F}{2\omega_s} sin\gamma \\ 0 &= a\sigma - \tfrac{F}{2\omega_s} cos\gamma \end{aligned} \tag{4.33}$$

In order to determine the damping and nonlinear coefficients, and the external force parameters in the forced van der Pol equation from the amplitudes and phases of the Fourier components in the time series, the lift coefficient is written as

$$l(t) \approx \quad a_1 cos(\Omega t + \tau_e - \gamma) + a_3 cos(3(\Omega t + \tau_e - \gamma) + \tfrac{\pi}{2}) \tag{4.34}$$

By comparing equation 4.34 with equation 4.23, one obtains

$$\alpha_v = \frac{32\omega_s a_3}{a_1^3} \tag{4.35}$$

Alternatively and as explained above, α_v can be obtained from the magnitude of the auto-trispectrum. Rearranging equation 4.12, one obtains

$$\alpha_v = \frac{512\omega_s \left|S_{llll}(\omega_s, \omega_s, \omega_s)\right|}{a^6} \tag{4.36}$$

From the Fourier transform of $l(t)$ at frequency Ω, i.e. equation 4.28, one obtains

$$\tau_e - \gamma = \Phi(L(\Omega)) \tag{4.37}$$

where $\Phi(L(\Omega))$ is the phase angle of $L(\Omega)$. Therefore,

$$\gamma = \tau_e - \Phi(L(\Omega)) \tag{4.38}$$

Substituting equation 4.38 in equation 4.33 yields

$$F = \frac{(\omega_s - \Omega)2\omega_s a}{cos\gamma}\mu_v = \frac{1}{4}\alpha_v a_1^2 + \frac{F}{2\omega_s} sin\gamma \tag{4.39}$$

Thus, given τ_e, one can identify F, μ_v, and α_v.

4.1.3 Case of No Resonance with Hard Excitation

In this case, the excitation is assumed to be hard, and only the damping and nonlinear parameters, μ_v and α_v, are scaled as $\epsilon\mu_v$ and $\epsilon\alpha_v$, respectively. The forced van der Pol equation is then written as

$$\ddot{l} + \omega_s^2 l^2 - \epsilon\mu_v \dot{l} + \epsilon\alpha_v l^2 \dot{l} = Fcos(\Omega t + \tau_e) \tag{4.40}$$

Using the method of multiple scales, an analytical approximate solution can be derived for equation 4.40 for the no-resonance condition, i.e. Ω is away from 0, ω, 3ω, and $\omega/3$. This solution is of the form

$$\begin{aligned} l(t) \approx \quad & acos(\omega_s t+\beta)+\tfrac{F}{\omega_s^2-\Omega^2}cos(\Omega t+\tau_e)+\tfrac{a^3\alpha_v}{32\omega_s}cos(3(\omega_s t+\beta)+\tfrac{\pi}{2}) \\ & +\tfrac{F^3\Omega\alpha_v}{4(\omega_s^2-\Omega^2)^3(9\Omega^2-\omega_s^2)}cos(3(\Omega t+\tau_e)+\tfrac{\pi}{2}) \\ & +\tfrac{F\Omega((F^2+2a^2(\omega_s^2-\Omega^2)^2)\alpha_v-4(\omega_s^2-\Omega^2)^2\mu_v)}{4(\omega_s^2-\Omega^2)^4}cos(\Omega t+\tau_e+\tfrac{\pi}{2}) \\ & +\tfrac{F(2\omega_s-\Omega)a^2\alpha_v}{4(\omega_s-\Omega)^2(3\omega_s^2+2\Omega\omega_s-\Omega^2)}cos((2\omega_s-\Omega)t+2\beta-\tau_e-\tfrac{\pi}{2}) \\ & +\tfrac{F^2(2\Omega-\omega_s)a\alpha_v}{16(\omega_s-\Omega)^3\Omega(\Omega+\omega_s)^2}cos((2\Omega-\omega_s)t+2\tau_e-\beta-\tfrac{\pi}{2}) \\ & +\tfrac{F(2\omega_s+\Omega)a^2\alpha_v}{4(\omega_s+\Omega)^2(3\omega_s^2-2\Omega\omega_s-\Omega^2)}cos((2\omega_s+\Omega)t+2\beta+\tau_e+\tfrac{\pi}{2}) \\ & +\tfrac{F^2(2\Omega+\omega_s)a\alpha_v}{16(\omega_s-\Omega)^2\Omega(\Omega+\omega_s)^3}cos((2\Omega-\omega_s)t+2\tau_e+\beta+\tfrac{\pi}{2}) \end{aligned} \tag{4.41}$$

In equation 4.41, the amplitude a and phase β are govened by

$$\dot{a}=[\frac{\mu_v}{2}-\frac{F^2\alpha_v}{4(\omega_s^2-\Omega^2)^2}]a-\frac{\alpha_v}{8}a^3 \tag{4.42}$$

and

$$\dot{\beta}=0 \tag{4.43}$$

Under steady state conditions, the amplitude and phase of the vortex shedding frequency components are given by

$$a^2 = \frac{4\eta}{\alpha_v - e^{-\eta t + 8\eta a_0}}$$

$$\beta = constant \tag{4.44}$$

where a_0 is the initial amplitude and $\eta = \mu_v - \frac{F^2\alpha_v}{2(\omega_s^2-\Omega^2)^2}$. The significance of this parameter can be explained by considering the first approximation for equation 4.41 written as

$$l(t) \approx \quad acos(\omega_s t + \beta) + \frac{F}{\omega_s^2 - \Omega^2} cos(\Omega t + \tau_e) + O(\epsilon) \tag{4.45}$$

This equation shows that the steady-state motion depends on the sign of η[24]. When $\eta > 0$, i.e. $\frac{\mu_v}{\alpha_v} > \frac{F^2}{2(\omega_s^2-\Omega^2)^2}$, $a \to 2\sqrt{\frac{\eta}{\alpha_v}}$ as $t \to \infty$, and the steady-state motion consists of a combination of the forced and free solutions according to equation 4.45. However, when $\eta < 0$, i.e. $\frac{\mu_v}{\alpha_v} < \frac{F^2}{2(\omega_s^2-\Omega^2)^2}$, $a \to 0$ as $t \to \infty$, and the steady-state motion consists of the forced solution only. Hence a small force permits the free oscillation to approach a nonzero value, while a large force causes the free oscillation term to decay.

When a and β are constants in equation 4.41, i.e., for steady-state oscillations, the solution given in equation 4.41 represents a periodic motion which can be written in complex form as

$$
\begin{aligned}
l(t) \approx\ & \tfrac{a}{2}\{e^{i(\omega_s t+\beta)} + e^{-i(\omega_s t+\beta)}\} + \tfrac{F}{2(\omega_s^2-\Omega^2)}\{e^{i(\Omega t+\tau_e)} + e^{-i(\Omega t+\tau_e)}\} \\
& + \tfrac{a^3\alpha_v}{64\omega_s}\{e^{3i(\omega_s t+\beta)+i\frac{\pi}{2}} + e^{-3i(\omega_s t+\beta)-i\frac{\pi}{2}}\} \\
& + \tfrac{F^3\Omega\alpha_v}{8(\omega_s^2-\Omega^2)^3(9\Omega^2-\omega_s^2)})\{e^{3i(\Omega t+\tau_e)+i\frac{\pi}{2}} + e^{-3i(\Omega t+\tau_e)-i\frac{\pi}{2}}\} \\
& + \tfrac{F\Omega((F^2+2a^2(\omega_s^2-\Omega^2)^2)\alpha_v-4(\omega_s^2-\Omega^2)^2\mu_v)}{8(\omega_s^2-\Omega^2)^4}\{e^{i(\Omega t+\tau_e)+i\frac{\pi}{2}} + e^{-i(\Omega t+\tau_e)-i\frac{\pi}{2}}\} \\
& + \tfrac{F(2\omega_s-\Omega)a^2\alpha_v}{8(\omega_s-\Omega)^2(3\omega_s^2+2\Omega\omega_s-\Omega^2)}\{e^{i(2\omega_s t-\Omega t+2\beta-\tau_e-\frac{\pi}{2})} + e^{-i(2\omega_s t-\Omega t+2\beta-\tau_e-\frac{\pi}{2})}\} \\
& + \tfrac{F^2(2\Omega-\omega_s)a\alpha_v}{32(\omega_s-\Omega)^3\Omega(\Omega+\omega_s)^2}\{e^{i(2\Omega t-\omega_s t+2\tau_e-\beta-\frac{\pi}{2})} + e^{-i(2\Omega t-\omega_s t+2\tau_e-\beta-\frac{\pi}{2})}\} \\
& + \tfrac{F(2\omega_s+\Omega)a^2\alpha_v}{8(\omega_s+\Omega)^2(3\omega_s^2-2\Omega\omega_s-\Omega^2)}\{e^{i(2\omega_s t+\Omega t+2\beta+\tau_e+\frac{\pi}{2})} + e^{-i(2\omega_s t+\Omega t+2\beta+\tau_e+\frac{\pi}{2})}\} \\
& + \tfrac{F^2(2\Omega+\omega_s)a\alpha_v}{32(\omega_s-\Omega)^2\Omega(\Omega+\omega_s)^3}\{e^{i(2\Omega t+\omega_s t+2\tau_e+\beta+\frac{\pi}{2})} + e^{-i(2\Omega t+\omega_s t+2\tau_e+\beta+\frac{\pi}{2})}\}
\end{aligned}
\tag{4.46}
$$

The Fourier transform of $l(t)$, represented by $L(\omega)$, is then given by

$$
\begin{aligned}
& l(t) \approx \\
& \tfrac{a}{2}\{e^{i\beta}\delta(\omega-\omega_s)+e^{-i\beta}\delta(\omega+\omega_s)\}+\tfrac{F}{2(\omega_s^2-\Omega^2)}\{e^{i\tau_e}\delta(\omega-\Omega)+e^{-i\tau_e}\delta(\omega+\Omega)\} \\
& +\tfrac{a^3\alpha_v}{64\omega_s}\{e^{3i\beta+i\frac{\pi}{2}}\delta(\omega-3\omega_s)+e^{-3i\beta-i\frac{\pi}{2}}\delta(\omega+3\omega_s)\} \\
& +\tfrac{F^3\Omega\alpha_v}{8(\omega_s^2-\Omega^2)^3(9\Omega^2-\omega_s^2)})\{e^{3i\tau_e+i\frac{\pi}{2}}\delta(\omega-3\Omega)+e^{-3i\tau_e-i\frac{\pi}{2}}\delta(\omega+3\Omega)\} \\
& +\tfrac{F\Omega((F^2+2a^2(\omega_s^2-\Omega^2)^2)\alpha_v-4(\omega_s^2-\Omega^2)^2\mu_v)}{8(\omega_s^2-\Omega^2)^4}\{e^{i\tau_e+i\frac{\pi}{2}}\delta(\omega-\Omega)+e^{-i\tau_e-i\frac{\pi}{2}}\delta(\omega+\Omega)\} \\
& +\tfrac{F(2\omega_s-\Omega)a^2\alpha_v}{8(\omega_s-\Omega)^2(3\omega_s^2+2\Omega\omega_s-\Omega^2)}\{e^{i(2\beta-\tau_e-\frac{\pi}{2})}\delta(\omega-2\omega_s+\Omega)+e^{-i(2\beta-\tau_e-\frac{\pi}{2})}\delta(\omega+2\omega_s-\Omega)\} \\
& +\tfrac{F^2(2\Omega-\omega_s)a\alpha_v}{32(\omega_s-\Omega)^3\Omega(\Omega+\omega_s)^2}\{e^{i(2\tau_e-\beta-\frac{\pi}{2})}\delta(\omega-2\Omega+\omega_s)+e^{-i(2\tau_e-\beta-\frac{\pi}{2})}\delta(\omega+2\Omega-\omega_s)\} \\
& +\tfrac{F(2\omega_s+\Omega)a^2\alpha_v}{8(\omega_s+\Omega)^2(3\omega_s^2-2\Omega\omega_s-\Omega^2)}\{e^{i(2\beta+\tau_e+\frac{\pi}{2})}\delta(\omega-2\omega_s-\Omega)+e^{-i(2\beta+\tau_e+\frac{\pi}{2})}\delta(\omega+2\omega_s+\Omega)\} \\
& +\tfrac{F^2(2\Omega+\omega_s)a\alpha_v}{32(\omega_s-\Omega)^2\Omega(\Omega+\omega_s)^3}\{e^{i(2\tau_e+\beta+\frac{\pi}{2})}\delta(\omega-2\Omega-\omega_s)+e^{-i(2\tau_e+\beta+\frac{\pi}{2})}\delta(\omega+2\Omega+\omega_s)\}
\end{aligned}
\tag{4.47}
$$

Examining the expression for $L(\omega)$, it is noted that the solution contains components with frequencies at $\omega_s, \Omega, 3\omega_s, 5\omega_s, 2\omega_s+\Omega$, and $2\omega_s-\Omega$. The amplitudes and phases of these components are given by

$$L(\omega_s) = \frac{1}{2}ae^{i\beta} \tag{4.48}$$

$$\begin{aligned} L(\Omega) &= \frac{F}{2(\omega_s^2 - \Omega^2)}e^{i\tau_e} \\ &+ \frac{F(2\omega_s - \Omega)a^2\alpha_v}{8(\omega_s - \Omega)^2(3\omega_s^2 + 2\Omega\omega_s - \Omega^2)}e^{i\tau_e + i\frac{\pi}{2}} \end{aligned} \tag{4.49}$$

$$L(3\omega_s) = \frac{a^3\alpha_v}{64\omega_s}e^{3i\beta + i\frac{\pi}{2}} \tag{4.50}$$

$$L(3\Omega) = \frac{F^3\Omega\alpha_v}{8(\omega_s^2 - \Omega^2)^3(9\Omega^2 - \omega_s^2)})e^{3i\tau_e + i\frac{\pi}{2}} \tag{4.51}$$

$$L(2\omega_s - \Omega) = \frac{F(2\omega_s - \Omega)a^2\alpha_v}{8(\omega_s - \Omega)^2(3\omega_s^2 + 2\Omega\omega_s - \Omega^2)}e^{i(2\beta - \tau_e - \frac{\pi}{2})} \tag{4.52}$$

$$L(2\Omega - \omega_s) = \frac{F^2(2\Omega - \omega_s)a\alpha_v}{32(\omega_s - \Omega)^3\Omega(\Omega + \omega_s)^2}e^{i(2\tau_e - \beta - \frac{\pi}{2})} \tag{4.53}$$

$$L(2\omega_s + \Omega) = \frac{F(2\omega_s + \Omega)a^2\alpha_v}{8(\omega_s + \Omega)^2(3\omega_s^2 - 2\Omega\omega_s - \Omega^2)}e^{i(2\beta + \tau_e + \frac{\pi}{2})} \tag{4.54}$$

and

$$L(2\Omega + \omega_s) = \frac{F^2(2\Omega + \omega_s)a\alpha_v}{32(\omega_s - \Omega)^2\Omega(\Omega + \omega_s)^3}e^{i(2\tau_e + \beta + \frac{\pi}{2})} \tag{4.55}$$

Based on the definition of the auto-trispectrum, i.e.

$$S_{llll}(\omega_k, \omega_l, \omega_m) = \lim_{T \to \infty} \frac{1}{T} E[L^*(\omega_k)L_*(\omega_l)L_*(\omega_m)L(\omega_k + \omega_l + \omega_m)] \tag{4.56}$$

several auto-trispectral moments can be identified between the frequency components in the above solution. One of these moments relates the vortex shedding response and its third harmonic. By letting $\omega_k = \omega_l = \omega_m = \omega_s$, one obtains

$$S_{llll}(\omega_s, \omega_s, \omega_s) \approx \frac{a^6 \alpha_v}{512\omega_s} e^{i\frac{\pi}{2}} \tag{4.57}$$

Equation 4.57 shows that the magnitude of the auto-trispectrum $S_{llll}(\omega_s, \omega_s, \omega_s)$ is related to the coefficient of the cubic nonlinearity α_v. Thus, this magnitude can be used to determine α_v. Additionally, the phase of the auto-trispectrum $S_{llll}(\omega_s, \omega_s, \omega_s)$, given by $\phi(3\omega_s) - 3\phi(\omega_s)$, is equal to $\frac{\pi}{2}$. The estimate of this phase should be used to validate the use of the van der Pol equation as a model. The level of auto-tricoherence for ($\omega_k = \omega_l = \omega_m = \omega_s$), defined as

$$t^2(\omega_s, \omega_s, \omega_s) \approx \frac{|S_{llll}(\omega_s, \omega_s, \omega_s)|^2}{|L(\omega_s)L(\omega_s)L(\omega_s)|^2 \, |L(3\omega_s)|^2} \tag{4.58}$$

should be used to determine the extent of coupling between ω_s and $3\omega_s$ and the validity of using the magnitude and phase of the trispectrum to estimate the parameters in a model of a physical phenomenon. A high level for the tricoherence indicates a high level of confidence in the measured phase relation and the value of the identified nonlinear coefficient.

For the forced van der Pol equation with no resonance and hard excitation, the steady state value of amplitude a is obtained by setting $\dot{a} = 0$ in equation 4.42, i.e.

$$0 = [\frac{\mu_v}{2} - \frac{F^2\alpha_v}{4(\omega_s^2 - \Omega^2)^2}]a - \frac{\alpha_v}{8}a^3 \tag{4.59}$$

In order to determine the linear and nonlinear damping coefficients, and the external force in the forced van der Pol equation from the amplitudes and phases of the Fourier components in the time series, the lift coefficient is written as

$$\begin{aligned} l(t) \approx \quad & a_1 cos(\omega_s t + \beta) + a_2 cos(\Omega t + \tau_e) + a_3 cos(3(\omega_s t + \beta) + \tfrac{\pi}{2}) \\ & + a_4 cos(3(\Omega t + \tau_e) + \tfrac{\pi}{2}) \end{aligned} \tag{4.60}$$

By comparing equation 4.60 with equations 4.41 and applying equation 4.59, one obtains

$$\alpha_v = \frac{32\omega_s a_3}{a_1^3} \tag{4.61}$$

$$F = \left\{ \frac{4(\omega_s^2 - \Omega^2)^3(9\Omega^2 - \omega_s^2)}{\Omega\alpha_v} \right\}^{\frac{1}{3}} \tag{4.62}$$

and

$$\mu_v = \frac{F^2\alpha_v}{2(\omega_s^2 - \Omega^2)^2} + \frac{\alpha_v}{4}a^2 \tag{4.63}$$

Alternatively, and as shown above, α_v can be obtained from the magnitude of the auto-trispectrum. Rearranging equation 4.57, one obtains

$$\alpha_v = \frac{512\omega_s \left| S_{llll}(\omega_s, \omega_s, \omega_s) \right|}{a^6} \tag{4.64}$$

which provides a way to determine the nonlinear damping coefficient α_v.

From the Fourier transform of $l(t)$ at frequency 3Ω, i.e. equation 4.51, the phase of the external force τ_e is obtained as

$$\tau_e = \frac{\Phi(L(3\Omega)) - \frac{\pi}{2}}{3} \tag{4.65}$$

where $\Phi(L(3\Omega))$ is used to denote the phase angle of $L(3\Omega)$.

Results and Discussion

As an example for the case of no resonance with hard exciation, the cylinder was forced to oscillate in the transverse direction at a frequency $\Omega = 0.22Hz$ at a nondimensional amplitude $\frac{y}{D} = 0.1$. The Reynolds number was set at 10,000. The power spectrum of the resulting lift coefficient, obtained from the RANS siumlation, is shown in figure 4.7. The spectrum shows several peaks. The two peaks at $\Omega = 0.22Hz$, the oscillation frequency, and at $\omega_s = 0.2637Hz$, the vortex shedding frequency, have the highest amplitude. Several other peaks are noted and they match with the components presented in equations 4.50 to 4.55. The lift auto-trispectrum, presented in Figure 4.8 shows the highest level of coupling between the vortex shedding frequency and its third harmonic. The amplitude and phase of the auto-trispectrum at the shedding frequency are given in Table 4.4. The phase angle is again near $\pi/2$ which indicates, and based on the approximate solution and equation 4.57, that the van der Pol equation should be used to model the lift on the transversely oscillating cylinder.

Values of the shedding frequency, $f = \frac{\omega_s}{2\pi}$, along with the amplitudes as defined in equation 4.60, a_1, a_2, a_3, a_4 and the phase, $\Phi(3L(\Omega))$, are given in

Table 4.5. Based on equations 4.61 - 4.64, the spectral parameters presented in Table 4.5 are used to estimate the F, τ_e, μ_v and α_v. These parameters are given in Table 4.6. It is of significant interest to note that the values determined for μ_v and α_v for the cases of soft and hard excitations and at two different frequencies are very close to values determined for the case of stationary cylinder. This shows that while the different excitations can include a slight variation in the added mass, stiffness or damping, the forced van der Pol equation can be used to model the forced transverse oscillations of circular cylinders. It should, however, be noted that under conditions where these quantities constitute a large part of the total mass, damping or stiffness, the model must be varied to take them into consideration. This point will be discussed in more details in Chapter 6.

Time series of the RANS simulated response and the integrated response based on equation 4.40 are compared in figure 4.9. The results clearly show that the identified parameters can be used to correctly determine the amplitude variations in the lift time series. This is further stressed by comparing the spectra, the auto-trispectra and the auto-tricoherence of both responses in figure 4.10, 4.11 and 4.12, respectively. The auto-spectra comparison shows that the two time series contain the same frequency components and that all major peaks have the same amplitude. The trispectra and tricoherence estimates show that both time series are characterized by the same cubic nonlinearities. This indicates that the reduced-order model accounted for all nonlinearities detected in the original time series.

Table 4.4: Lift auto-trispectrum for the transversely oscillating cylinder - amplitude and phase (no resonance with hard excitation)

$\Omega(Hz)$	0.22
$\frac{y}{D}$	0.1
$f_1(Hz)$	0.2637
$f_2(Hz)$	0.2637
$f_3(Hz)$	0.2637
Amplitude	6.298e-7
Phase(rad)	1.7017

Table 4.5: Lift spectral parameters for the transversely oscillating cylinder (no resonance with hard excitation)

$\Omega(Hz)$	0.22
$\frac{y}{D}$	0.1
$f(Hz)$	0.2637
a_1	0.335
a_2	1.83
a_3	2.76e-4
a_4	0.0181
$\Phi(3L(\Omega))(rad)$	-1.16

Table 4.6: Lift model parameters in forced van der Pol equation (no resonance with hard excitation)

$\Omega(Hz)$	0.22
$f(Hz)$	0.2637
F	1.039
$\tau_e(rad)$	-0.9
μ_v	0.3132
α_v from $L(3\omega_s)$	0.3892
α_v from S_{llll}	0.3899

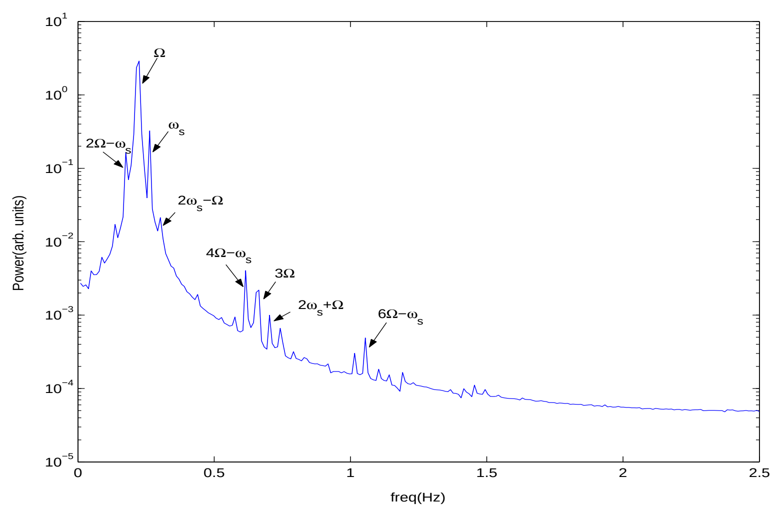

Figure 4.7: Power spectrum of the lift coefficient for the transversely oscillating cylinder at frequency $\Omega = 0.22Hz$ and amplitude $\frac{y}{D} = 0.1$

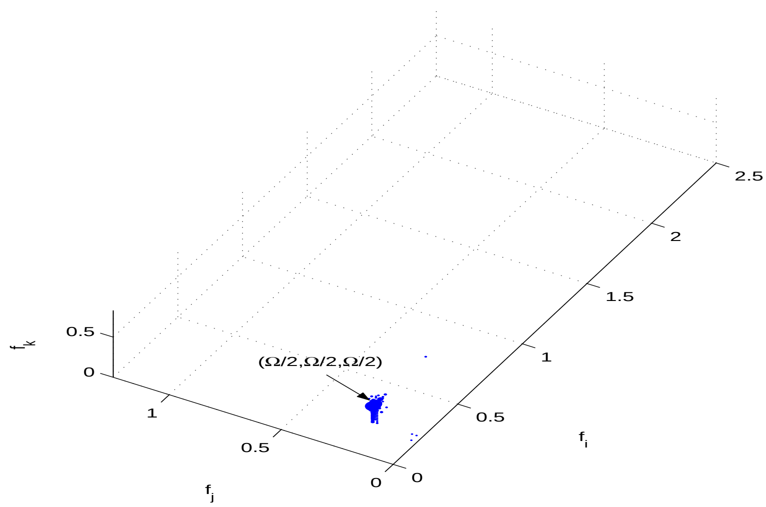

Figure 4.8: Auto-trispectrum of the lift coefficient for the transversely oscillating cylinder at the frequency $\Omega = 0.22Hz$ and amplitude $\frac{y}{D} = 0.1$. Only values above 10% of maximum level are indicated.

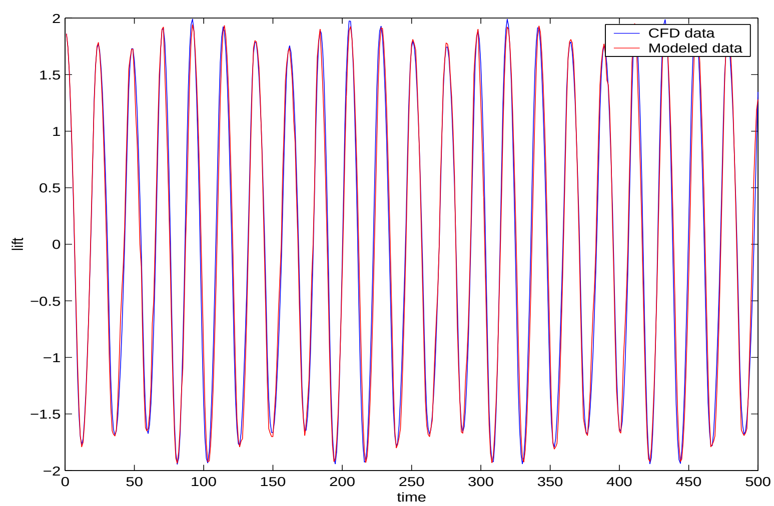

Figure 4.9: Comparison of RANS simulated and modeled time series of the lift coefficients for the transversely oscillating cylinder $\Omega = 0.22Hz$ and amplitude $\frac{y}{D} = 0.1$

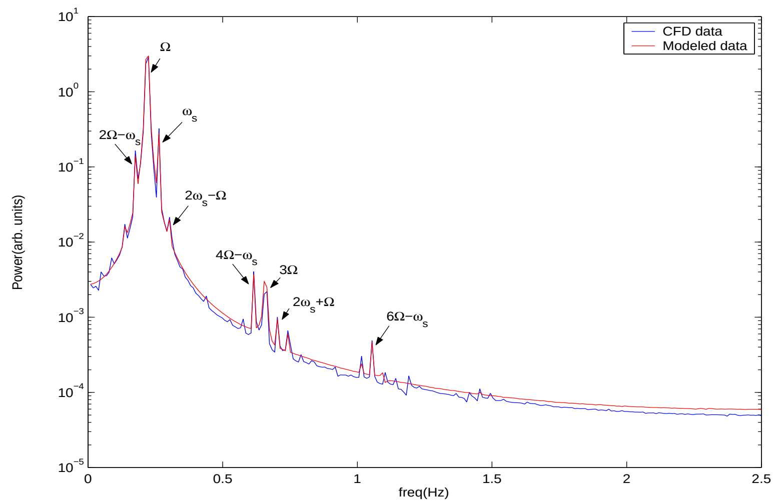

Figure 4.10: Comparison of power spectra of the RANS simulated and modeled lift coefficients for the transversely oscillating cylinder at the frequency $\Omega = 0.22Hz$ and amplitude $\frac{y}{D} = 0.1$

4.2 Drag Model for Transversely Oscillating Cylinder

In chapter 3, it was shown that the drag coefficient is proportional to l^2. As such, the drag coefficient on the transversely oscillating cylinder is modeled as

$$d = (d_m - c_1) + k_2(l + k_1 cos(\Omega t + \tau_e) + k_3 cos(3\Omega t + 3\tau_e))^2 \tag{4.66}$$

where d_m is the mean drag and can be obtained independently as a mean value from the time series of the drag, l represents the lift from the vortex shedding and the components Ω and 3Ω are used to relate the drag to forced oscillations in the transverse direction at a frequency Ω.

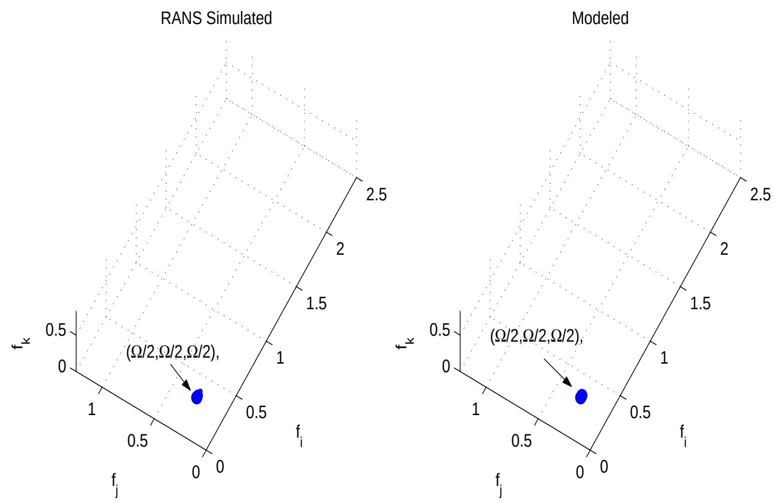

Figure 4.11: Comparison of auto-trispectra of the RANS simulated and modeled lift coefficients for the transversely oscillating cylinder at the frequency $\Omega = 0.22Hz$ and amplitude $\frac{y}{D} = 0.1$. Only values above 10% of maximum level are indicated.

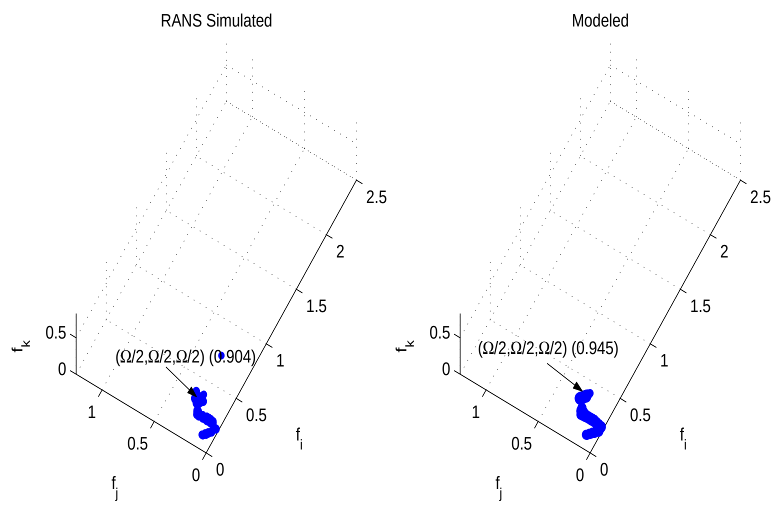

Figure 4.12: Comparison of auto-tricoherence of the RANS simulated and modeled lift coefficients for the transversely oscillating cylinder at the frequency $\Omega = 0.22Hz$ and amplitude $\frac{y}{D} = 0.1$. Circles are used to identify coherence levels above 0.1 with the larger circles indicating a higher level of tricoherence.

To determine the coefficient k_1 and k_3, we define an effective lift coefficient, $\hat{l}$, as

$$\hat{l} = l + k_1 cos(\Omega t + \tau_e) + k_3 cos(3\Omega t + 3\tau_e) \tag{4.67}$$

The cross-bispectrum between the drag and the effective lift is then defined as

$$\hat{B}(\omega_1, \omega_2) = \hat{L}(\omega_1)\hat{L}(\omega_2)D^*(\omega_1 + \omega_2) \tag{4.68}$$

where $\hat{L}$ is the Fourier transform of the effective lift coefficient $\hat{l}$ and D is the Fourier transform of the drag coefficient d. The Fourier transform of equation 4.67 yields

$$\hat{L}(\omega) = L(\omega) + k_1 e^{\tau_e}\delta(\omega - \Omega) + k_3 e^{3\tau_e}\delta(\omega - 3\Omega) \tag{4.69}$$

Thus, the cross-bispectrum can be rewritten as

$$\begin{aligned} \hat{B}(\omega_1, \omega_2) \quad = \quad & (L(\omega_1) + k_1 e^{\tau_e}\delta(\omega_1 - \Omega) + k_3 e^{3\tau_e}\delta(\omega_1 - 3\Omega) \\ & (L(\omega_2) + k_1 e^{\tau_e}\delta(\omega_2 - \Omega) + k_3 e^{3\tau_e}\delta(\omega_2 - 3\Omega)) \\ & D^*(\omega_1 + \omega_2) \end{aligned} \tag{4.70}$$

Substituting ω_1 and ω_2 in equation 4.70 with ω_s and Ω respectively, one obtains

$$\begin{aligned} \hat{B}(\omega_s, \Omega) &= L(\omega_s)(L(\Omega) + k_1 e^{\tau_e})D^*(\omega_s + \Omega) \\ &= L(\omega_s)L(\Omega)D^*(\omega_s + \Omega) + L(\omega_s)k_1 e^{\tau_e}D^*(\omega_s + \Omega) \end{aligned} \tag{4.71}$$

Substituting ω_1 and ω_2 in equation 4.70 with ω_s and 3Ω respectively, one obtains

$$\begin{aligned} \hat{B}(\omega_s, 3\Omega) &= L(\omega_s)(L(3\Omega) + k_3 e^{3\tau_e})D^*(\omega_s + 3\Omega) \\ &= L(\omega_s)L(3\Omega)D^*(\omega_s + 3\Omega) + L(\omega_s)k_3 e^{3\tau_e}D^*(\omega_s + 3\Omega) \end{aligned} \tag{4.72}$$

Expressing the different Fourier components and their bispetral moments in the form of amplitude and phase, i.e.

$$\begin{aligned} L(\omega_s) &= a_1 e^{i\beta} && (4.73)\\ D(\omega_s+\Omega) &= a_{12} e^{i\beta_{12}} && (4.74)\\ D(\omega_s+3\Omega) &= a_{13} e^{i\beta_{13}} && (4.75)\\ B(\omega_s,\Omega) &= L(\omega_s)L(\Omega)D^*(\omega_s+\Omega) = B_0 e^{ib_0} && (4.76) \end{aligned}$$

and

$$B(\omega_s,3\Omega) = L(\omega_s)L(3\Omega)D^*(\omega_s+3\Omega) = B_1 e^{ib_1} \tag{4.77}$$

one obtains

$$\begin{aligned} \hat{B}(\omega_s,\Omega) &= B_0 e^{ib_0} + a_1 e^{i\beta} k_1 e^{i\tau_e} a_{12} e^{-i\beta_{12}}\\ &= B_0 e^{ib_0} + a_1 k_1 a_{12} e^{i(\beta+\tau_e-\beta_{12})}\\ &= [B_0 cos(b_0) + a_1 k_1 a_{12} cos(\beta+\tau_e-\beta_{12})]\\ &\quad +[B_0 sin(b_0) + a_1 k_1 a_{12} sin(\beta+\tau_e-\beta_{12})] \end{aligned} \tag{4.78}$$

and

$$\begin{aligned} \hat{B}(\omega_s,3\Omega) &= B_1 e^{ib_1} + a_1 e^{i\beta} k_3 e^{3i\tau_e} a_{13} e^{-i\beta_{13}}\\ &= B_1 e^{ib_1} + a_1 k_3 a_{13} e^{i(\beta+3\tau_e-\beta_{13})}\\ &= [B_1 cos(b_1) + a_1 k_3 a_{13} cos(\beta+3\tau_e-\beta_{13})]\\ &\quad +[B_1 sin(b_1) + a_1 k_3 a_{13} sin(\beta+3\tau_e-\beta_{13})] \end{aligned} \tag{4.79}$$

Realizing that the effective lift and drag are related by a phase difference of -$\frac{\pi}{2}$, i.e. the phase of $\hat{B}(\omega_s,\Omega)$ and $\hat{B}(\omega_s,3\Omega)$ should be set to -$\frac{\pi}{2}$, one obtains

$$B_0 cos(b_0) + a_1 k_1 a_{12} cos(\beta+\tau_e-\beta_{12}) = 0 \tag{4.80}$$

and

$$B_1cos(b_1) + a_1k_3a_{13}cos(\beta + 3\tau_e - \beta_{13}) = 0 \tag{4.81}$$

Therefore, the parameters k_1 and k_3 can be determined from the bispectral moment according to

$$k_1 = -\frac{B_0cos(b_0)}{a_1a_{12}cos(\beta + \tau_e - \beta_{12})} \tag{4.82}$$

$$k_3 = -\frac{B_1cos(b_1)}{a_1a_{13}cos(\beta + 3\tau_e - \beta_{13})} \tag{4.83}$$

Once k_1 and k_3 are identified, k_2 and c_1 can be identified via the fitting of a straight line given by

$$d = \hat{c}_1 + k_2\tilde{l} \tag{4.84}$$

where $\hat{c}_1 = d_m - c_1$ and $\tilde{l} = (l + k_1cos(\Omega t + \tau_e) + k_3cos(\Omega t + 3\tau_e))^2$

Results and Discussion

The power spectrum of the drag coefficient on the transversely oscillating cylinder, obtained from the RANS siumlation corresponding to the case of soft excitation with no resonance, i.e. at the oscillating frequency of 0.1Hz and a nondimensional amplitude $\frac{y}{D} = 0.1$ is shown in figure 4.13. The spectrum shows four major peaks at $2\omega_s$, $\omega_s + \Omega$, $\omega_s - \Omega$ and $4\omega_s$, where $\omega_s = 0.2393Hz$ and $\Omega = 0.1Hz$. This suggests that the most important coupling between the drag and lift coefficients is quadratic. The cross-bispectrum and cross-bicoherence between the lift and drag coefficients are presented in figures 4.14 and 4.15, respectively. In the cross-bispectrum plot, only values above 10% of the maximum level are plotted. In the cross-bicoherence plot, the contour levels are set at 0.3, 0.6, and 0.9. The results clerly show a high level of quadratic coupling between the peaks observed in the power spectrum.

The power spectrum of the drag coefficient for the case of hard exciation with no resonance, i.e. at an oscillating frequency of 0.22Hz and a nondimensional amplitude $\frac{y}{D} = 0.1$ is shown in figure 4.16. The spectrum is characterized by major peaks with significant sidebands. The corresponding cross-bispectrum and cross-bicoherence plots, presented in figures 4.17 and 4.18 show quadratic couplings between these peaks. These couplings extend to the sidebands. Estimates of the amplitudes and phases of the cross-bispectra of the different frequency components in both excitation cases are shown in Table 4.7.

Values of Ω, a_1, a_2, a_{12}, a_{13}, β_1, β_{12}, β_{13}, $B_0cos(b_0)$, and $B_1cos(b_1)$, as defined above and for both excitation conditions, are shown in Table 4.8. These parameters were used to estimate k_1, k_2, and k_3 based on equations 4.82, 4.83 and 4.84. The values shown in Table 4.9 were then used to predict the drag coefficient by applying equation 4.66. It is of interest to note that the determined parameters show small levels of variations for the two transverse excitation cases of soft and hard excitations with no resonance. This shows that the proposed model and identification procedure are robust enough to model the drag coefficient on transverely oscillating cylinders.

To verify the drag coefficient model, we compare the RANS simulated

Table 4.7: Lift-drag cross-bispectrum for the transversely oscillating cylinder - amplitude and phase (no resonance with soft (0.1Hz) and hard (0.22Hz) excitations)

$\Omega(Hz)$	0.1	0.22	0.22
$\frac{y}{D}$	0.1	0.1	0.1
$f_1(Hz)$	0.2393	0.2637	0.2637
$f_2(Hz)$	0.1	0.22	0.66
Amplitude	B_0=0.0050	B_0=0.0085	B_1=1.053e-5
Phase(rad)	b_0=-2.2794	b_0=2.5115	b_1=-3.0718

and modeled time series, power spectra, cross-bispectra and cross-bicoherence. The comparisons for the case of oscillating frequency $\Omega = 0.1$ are shown in figures 4.19-4.22. Figure 4.19 shows that the model given in equation 4.66 along with the parameters presented in Table 4.9 yield the correct amplitude variations in the time series. This is further stressed by the comparison of the spectra for both RANS simulated and modeled time series, as shown in Figure 4.20. The results clearly show that the amplitudes of the spectral peaks are correctly predicted. The comparison of the cross-bispectra and cross-bicoherence, presented in figures 4.21 and 4.22, show that the model accounts for all quadratic couplings that are a part of the original time series. As for the case of hard excitation with no resonance, i.e. transverse oscillations at a frequency of 0.22Hz, the comparisons of time series in figure 4.23, power spectra in figure 4.24, and cross-bispectra and cross-bicoherence in figures 4.25 and 4.26, show that the basic dynamics can also be predicted with the model presented in equation 4.66.

Table 4.8: Drag spectral parameters for the transversely oscillating cylinder (no resonance with soft (0.1Hz) and hard (0.22Hz) excitations)

$\Omega(Hz)$	0.1	0.22
a_1	1.79	0.335
a_2	0.06	1.83
a_{12}	0.0468	0.1112
a_{13}	N/A	0.0139
$\beta_1(rad)$	-1.274	1.26
$\beta_{12}(rad)$	-0.5	-1.71
$\beta_{13}(rad)$	N/A	-3.1
$B_0cos(b_0)$	-0.0033	-0.0069
$B_1cos(b_1)$	N/A	-1.05e-5

Table 4.9: Drag model parameters as proposed in Equation 4.66 (no resonance with soft (0.1Hz) and hard (0.22Hz) excitations)

$\Omega(Hz)$	0.1	0.22
d_m	1.6536	1.6759
c_1	0.31	0.35
k_1	-2.02	-2.0
k_2	0.12	0.115
k_3	0	-0.095

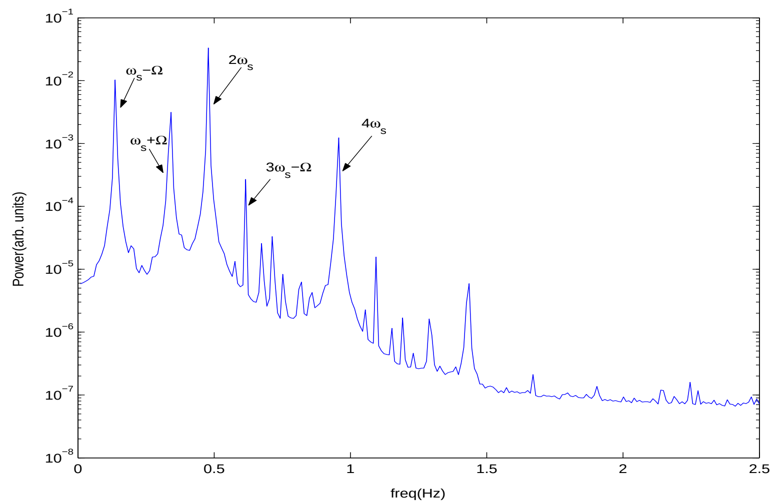

Figure 4.13: Power spectrum of the drag coefficient for the transversely oscillating cylinder at frequency $\Omega = 0.1Hz$ and amplitude $\frac{y}{D} = 0.1$

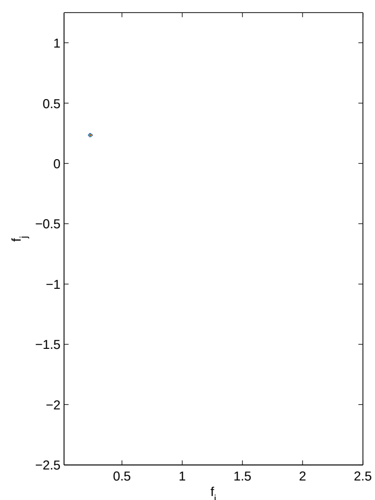

Figure 4.14: Cross-bispectrum of the lift and drag coefficients for the transversely oscillating cylinder at frequency $\Omega = 0.1Hz$ and amplitude $\frac{y}{D} = 0.1$

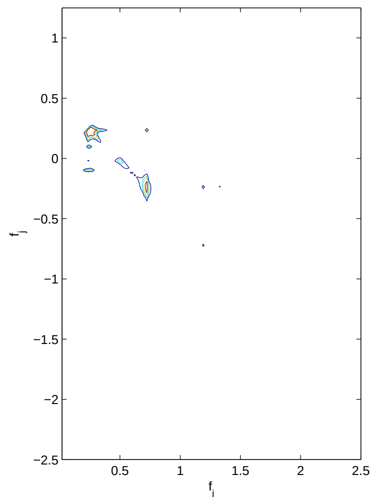

Figure 4.15: Cross-bicoherence of the lift and drag coefficients for the transversely oscillating cylinder at frequency $\Omega = 0.1Hz$ and amplitude $\frac{y}{D} = 0.1$. Contour levels are set at 0.3, 0.6, 0.9

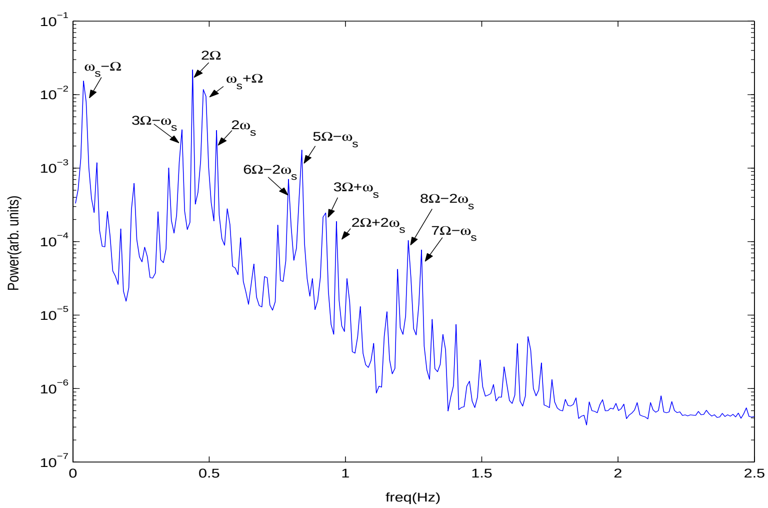

Figure 4.16: Power spectrum of the drag coefficient for the transversely oscillating cylinder at frequency $\Omega = 0.22Hz$ and amplitude $\frac{y}{D} = 0.1$

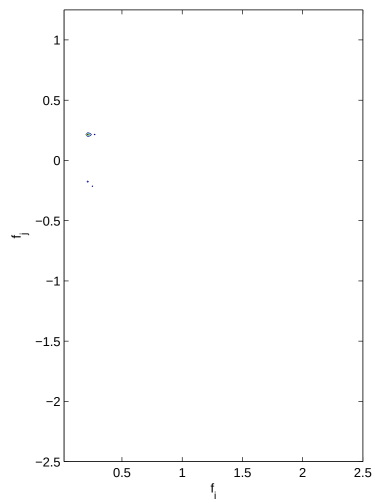

Figure 4.17: Cross-bispectrum of the lift and drag coefficients for the transversely oscillating cylinder at frequency $\Omega = 0.22Hz$ and amplitude $\frac{y}{D} = 0.1$

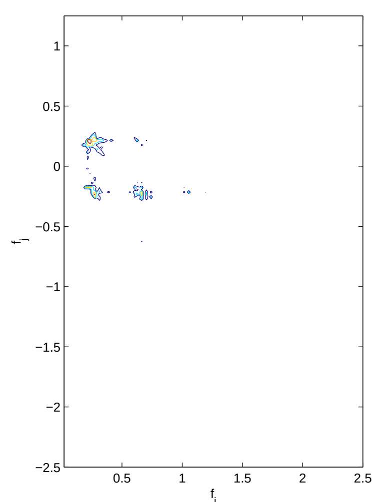

Figure 4.18: Cross-bicoherence of the lift and drag coefficients for the transversely oscillating cylinder at frequency $\Omega = 0.22Hz$ and amplitude $\frac{y}{D} = 0.1$. Contour levels are set at 0.3, 0.6, 0.9.

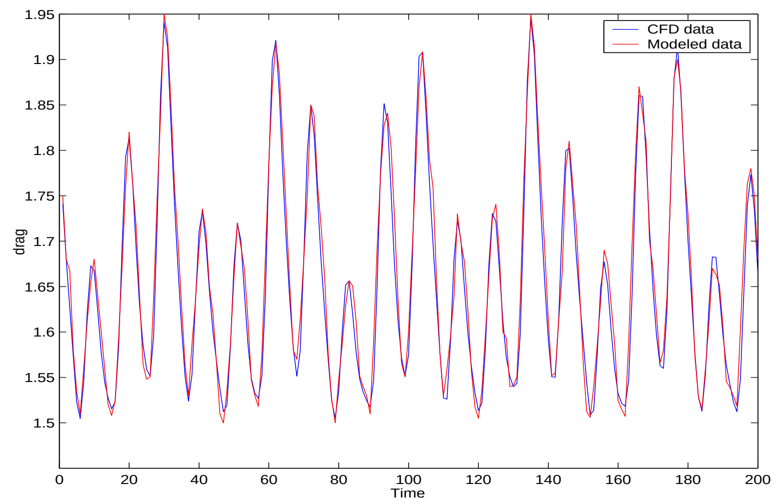

Figure 4.19: Comparison of time series of the RANS simulated and modeled drag coefficient for the transversely oscillating cylinder at frequency $\Omega = 0.1Hz$ and amplitude $\frac{y}{D} = 0.1$

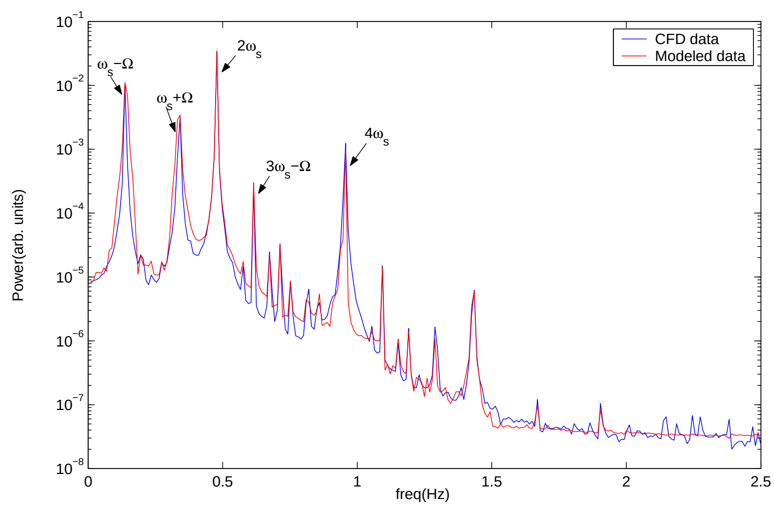

Figure 4.20: Comparison of power spectra of the RANS simulated and modeled drag coefficient for the transversely oscillating cylinder at frequency $\Omega = 0.1Hz$ and amplitude $\frac{y}{D} = 0.1$

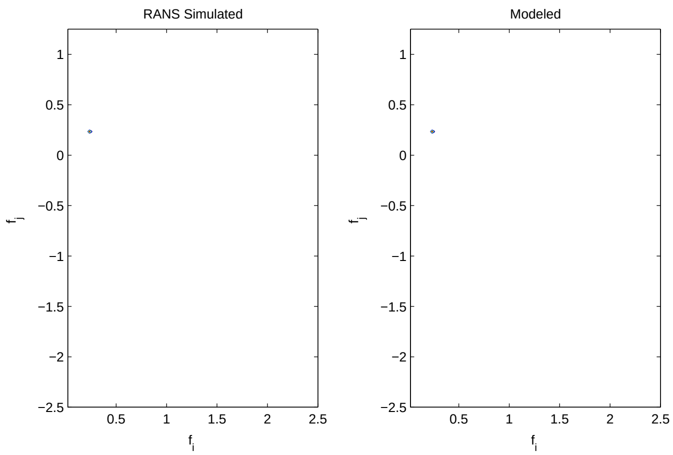

Figure 4.21: Comparison of cross-bispectra between the lift and drag coefficients of the RANS simulated and modeled time series for the transversely oscillating cylinder at frequency $\Omega = 0.1Hz$ and amplitude $\frac{y}{D} = 0.1$

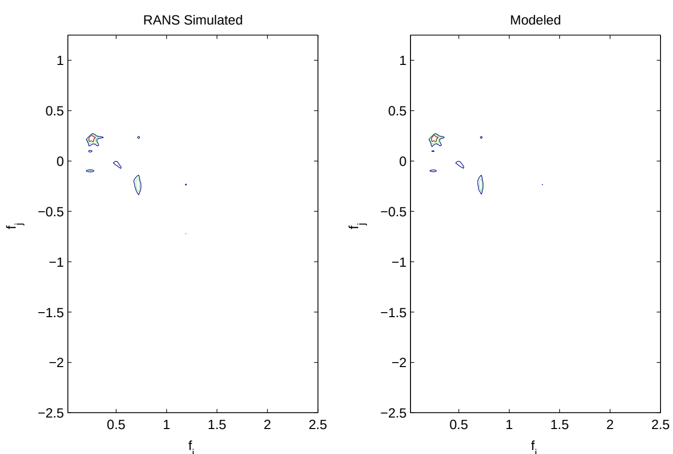

Figure 4.22: Comparison of cross-bicoherence between the lift and drag coefficients of the RANS simulated and modeled time series for the transversely oscillating cylinder at frequency $\Omega = 0.1Hz$ and amplitude $\frac{y}{D} = 0.1$. Contour levels are set at 0.3, 0.6, 0.9

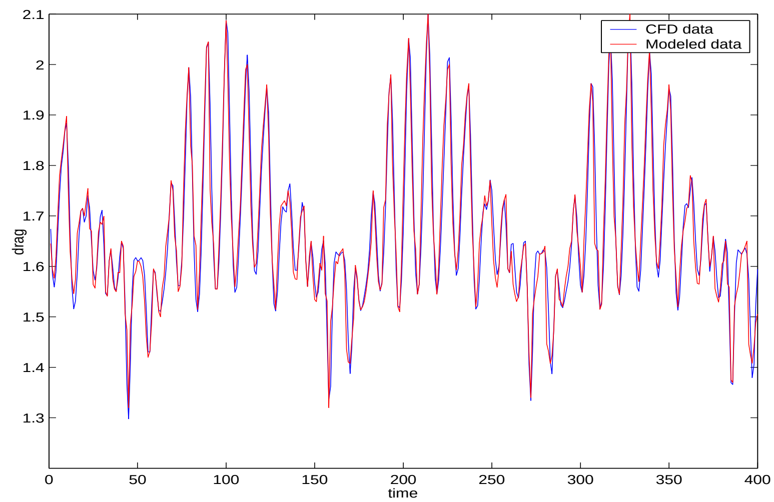

Figure 4.23: Comparison of the RANS simulated and modeled time series of the drag coefficient for the transversely oscillating cylinder at frequency $\Omega = 0.22Hz$ and amplitude $\frac{y}{D} = 0.1$

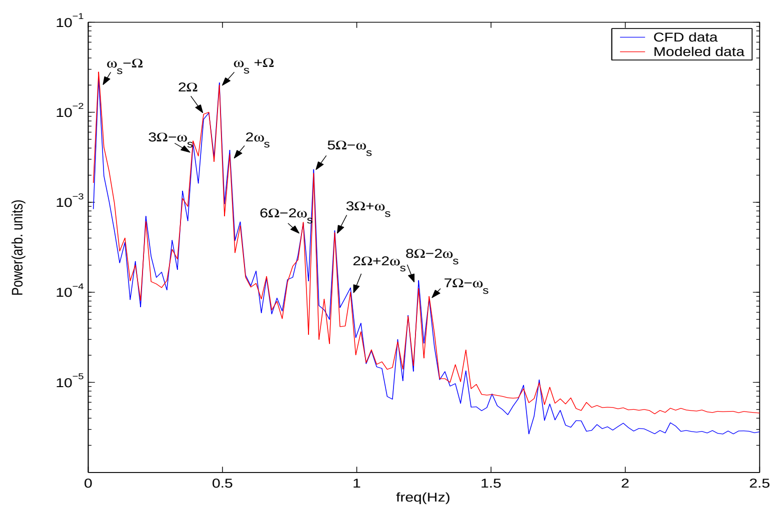

Figure 4.24: Comparison of power spectra of the RANS simulated and modeled drag coefficient for the transversely oscillating cylinder at frequency $\Omega = 0.22Hz$ and amplitude $\frac{y}{D} = 0.1$

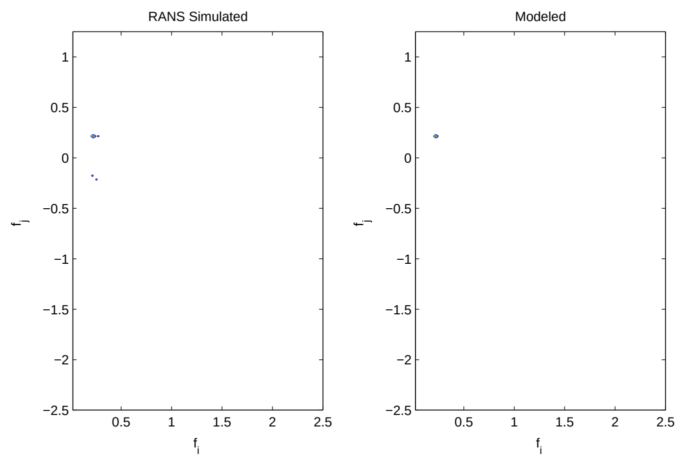

Figure 4.25: Comparison of cross-bispectra between the lift and drag coefficients of the RANS simulated and modeled time series for the transversely oscillating cylinder at frequency $\Omega = 0.22Hz$ and amplitude $\frac{y}{D} = 0.1$

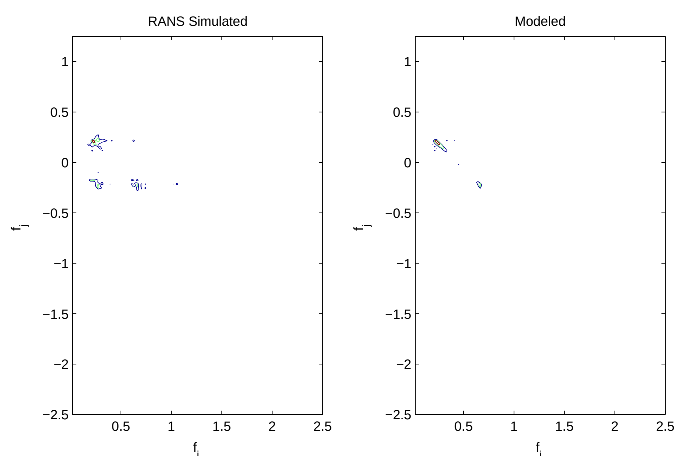

Figure 4.26: Comparison of cross-bicoherence between the lift and drag coefficients of the RANS simulated and modeled time series for the transversely oscillating cylinder at frequency $\Omega = 0.22Hz$ and amplitude $\frac{y}{D} = 0.1$. Contour levels are set at 0.3, 0.6, 0.9

Chapter 5

Lift and Drag Modeling on a Forced Inline Oscillating Cylinder

In this chapter, the lift and drag coefficients on an inline oscillating cylinder under different forced conditions are modeled. The lift coefficient is modeled by a parametrically excited van der Pol oscillator which is written as

$$\ddot{l} + \omega_s^2 l^2 - \mu_v \dot{l} + \alpha_v l^2 \dot{l} + \xi cos(\Omega t + \tau) l = 0 \tag{5.1}$$

where ω_s is the frequency, μ_v and α_v represent the linear and nonlinear damping coefficients, and ξ and τ are respectively the amplitude and phase of the excitation harmonic function which represents the inline oscillations. Based on equation 3.3, the drag coefficient is modeled as

$$d = (d_m - c_1) + k_2 l^2 + k_1 cos(\Omega t + \tau_e) \tag{5.2}$$

where d_m is the mean drag and can be obtained independently as a mean value from the time series of the drag. The term $k_1 cos(\Omega t + \tau_e)$ is added to account for the drag induced by the inline oscillations.

Different resonance conditions that represent different physical phenomena and can be exploited to identify the parameters in equations 5.1 and 5.2 are considered. The identification is performed by combining approximate solutions of 5.1 with amplitude and phase relations of higher-order spectral moments.

5.1 Parametically Excited Van Der Pol Equation as a Model for the Lift Coefficient on Inline Oscillating Circular Cylinders

To balance the damping, nolinearities, and parametric excitation in equation 5.1, we scale μ_v, α_v and ξ as $\epsilon\mu_v$, $\epsilon\alpha_v$ and $\epsilon\xi$. The parametrically excited van der Pol equation is then written as

$$\ddot{l} + \omega_s^2 l^2 - \epsilon\mu_v \dot{l} + \epsilon\alpha_v l^2 \dot{l} + \epsilon\xi cos(\Omega t + \tau) l = 0 \tag{5.3}$$

Next, parametric identification of the different terms in equation 5.3 is carried out for both resonance and no resonance conditions. Amplitude and phase relations of higher-order spectral moments are combined with approximate solutions for these different conditions to determine the different parameters.

5.1.1 Case of No Resonance

Using the method of multiple scales, an analytical approximate solution is derived for equation 5.3 for the no-resonance condition, i.e. Ω is away from $2\omega_s$. The approximate solution is of the form

$$\begin{aligned} l(t) \approx \quad & a cos(\omega_s t + \beta) + \tfrac{a^3\alpha_v}{32\omega_s} cos(3(\omega_s t + \beta) + \tfrac{\pi}{2}) \\ & + \tfrac{a\xi}{2\omega_s - \Omega)2\Omega} cos((\Omega - \omega_s)t + \tau - \beta + \pi) \\ & + \tfrac{a\xi}{2\omega_s + \Omega)2\Omega} cos((\Omega + \omega_s)t + \tau + \beta) \end{aligned} \tag{5.4}$$

In equation 5.4, the amplitude a and phase β are govened by

$$\begin{aligned} & \dot{a} = \tfrac{\mu_v}{2} a - \tfrac{\alpha_v}{8} a^3 \\ & \dot{\beta} = 0 \end{aligned} \tag{5.5}$$

When a and β are constants in equation 5.5, i.e., for steady-state oscillations, the solution given in equation 5.4 represents a periodic motion which can be written in complex form as

$$\begin{aligned} l(t) \approx \quad & \tfrac{a}{2}\{e^{i(\omega_s t+\beta)} + e^{-i(\omega_s t+\beta)}\} + \tfrac{a^3\alpha_v}{64\omega_s}\{e^{3i(\omega_s t+\beta)+i\frac{\pi}{2}} + e^{-3i(\omega_s t+\beta)-i\frac{\pi}{2}}\} \\ & + \tfrac{a\xi}{2\omega_s - \Omega)4\Omega}\{e^{i[(\Omega-\omega_s)t+\tau-\beta+\pi]} + e^{-i[(\Omega-\omega_s)t+\tau-\beta+\pi]}\} \\ & + \tfrac{a\xi}{2\omega_s + \Omega)4\Omega}\{e^{i[(\Omega+\omega_s)t+\tau+\beta]} + e^{-i[(\Omega+\omega_s)t+\tau+\beta]}\} \end{aligned} \tag{5.6}$$

The Fourier transform of $l(t)$ represented by $L(\omega)$ is then given by

$$l(t) \approx$$
$$\tfrac{a}{2}\{e^{i\beta}\delta(\omega-\omega_s)+e^{-i\beta}\delta(\omega+\omega_s)\}$$
$$+\tfrac{a^3\alpha_v}{64\omega_s}\{e^{3i\beta+i\frac{\pi}{2}}\delta(\omega-3\omega_s)+e^{-3i\beta-i\frac{\pi}{2}}\delta(\omega+3\omega_s)\}$$
$$+\tfrac{a\xi}{(2\omega_s-\Omega)4\Omega}\{e^{i(\tau-\beta+\pi)}\delta(\omega+\omega_s-\Omega)+e^{-i(\tau-\beta+\pi)}\delta(\omega-\omega_s+\Omega)\}$$
$$+\tfrac{a\xi}{(2\omega_s+\Omega)4\Omega}\{e^{i(\tau+\beta)}\delta(\omega-\omega_s-\Omega)+e^{-i(\tau+\beta)}\delta(\omega+\omega_s+\Omega)\} \tag{5.7}$$

Examining the expression for $L(\omega)$ given in 5.7, it is noted that the solution contains components with frequencies at ω_s, $3\omega_s$, $\Omega-\omega_s$ and $\Omega+\omega_s$. These components are given by

$$L(\omega_s) = \frac{1}{2}ae^{i\beta} \tag{5.8}$$

$$L(3\omega_s) = \frac{a^3\alpha_v}{64\omega_s}e^{3i\beta+i\frac{\pi}{2}} \tag{5.9}$$

$$L(\Omega-\omega_s) = \frac{a\xi}{(2\omega_s-\Omega)4\Omega}e^{i(\tau-\beta+\pi)} \tag{5.10}$$

and

$$L(\Omega+\omega_s) = \frac{a\xi}{(2\omega_s+\Omega)4\Omega}e^{i(\tau+\beta)} \tag{5.11}$$

Based on the definition of the auto-trispectrum, which is given by

$$S_{llll}(\omega_k,\omega_l,\omega_m) = \lim_{T\to\infty}\frac{1}{T}E[L^*(\omega_k)L_*(\omega_l)L_*(\omega_m)L(\omega_{k+l+m})] \tag{5.12}$$

several trispectral moments that involve the different frequency components in equations 5.8 - 5.11 can be identified in the above solution. Two of these moments are

$$S_{llll}(\omega_s, \omega_s, \omega_s) \approx \frac{a^6 \alpha_v}{512\omega_s} e^{i\frac{\pi}{2}} \tag{5.13}$$

which relates the vortex shedding frequency and its third harmonic, and

$$S_{llll}(\Omega - \omega_s, \omega_s, \omega_s) \approx \frac{a^4 \xi^2}{64\Omega^2(2\omega_s - \Omega)(2\omega_s + \Omega)} e^{-i\pi} \tag{5.14}$$

which relates the vortex shedding frequency to its sum and difference with the excitation frequency. The magnitude of the auto-trispectrum $S_{llll}(\omega_s, \omega_s, \omega_s)$ depends on the coefficient of the cubic nonlinearity α_v. Its phase, given by $\phi(3\omega_s) - 3\phi(\omega_s)$, is equal to $\frac{\pi}{2}$. The magnitude of the auto-trispectrum $S_{llll}(\Omega - \omega_s, \omega_s, \omega_s)$ depends on the coefficient of the parametric excitation ξ. Its phase is equal to $-\pi$. For nonlinear systems that can be modeled by the parametrically excited van der Pol equation, these quantities can be used to determine α_v and ξ and determine the suitability of using the harmonically-excited van der Pol equation to model the lift on a forced inline oscillating cylinder.

The normalized value for the auto-trispectrum, namely, the auto-tricoherence for $(\omega_k = \omega_l = \omega_m = \omega_s)$ is defined by

$$t^2(\omega_s, \omega_s, \omega_s) \approx \frac{|S_{llll}(\omega_s, \omega_s, \omega_s)|^2}{|L(\omega_s)L(\omega_s)L(\omega_s)|^2 \, |L(3\omega_s)|^2} \tag{5.15}$$

The auto-tricoherence for the case where $(\omega_k = \Omega - \omega_s, \text{and } \omega_l = \omega_m = \omega_s)$

is defined by

$$t^2(\Omega-\omega_s,\omega_s,\omega_s) \approx \frac{|S_{llll}(\Omega-\omega_s,\omega_s,\omega_s)|^2}{|L(\Omega-\omega_s)L(\omega_s)L(\omega_s)|^2\,|L(\Omega+\omega_s)|^2} \tag{5.16}$$

A unit value for the auto-tricoherence indicates perfect cubic phase coupling among the four frequency components. A near zero value indicates no coupling and any value in between indicates partial coupling among the four frequency components. Thus, the auto-tricoherence gives the level of confidence in the measured values of the magnitude and phase of the auto-trispectrum. Consequently, the auto-tricoherence should be used to determine the validity of using the magnitude and phase of the trispectrum to model any physical phenomenon characterized by a cubic nonlinearity.

For the parametrically excited van der Pol equation with no resonance, the steady state oscillations are obtained by setting $\dot{a}=0$ in equation 5.5. Under those conditions, the amplitude of the vortex shedding frequency component, a, is related to the damping and nonlinear coefficients by

$$a = 2\sqrt{\frac{\mu_v}{\alpha_v}} \tag{5.17}$$

In order to determine the linear and nonlinear damping coefficients, and the excitation parameter in the parametrically excited van der Pol equation from the amplitudes and phases of the Fourier components in the time series, we represent the lift coefficient as

$$\begin{aligned} l(t) \approx \quad & a_1 cos(\omega_s t+\beta) + a_2 cos((\Omega-\omega_s)t+\tau-\beta+\pi) \\ & + a_3 cos(3(\omega_s t+\beta)+\tfrac{\pi}{2}) \qquad (5.18) \\ & + a_4 cos((\Omega+\omega_s)t+\tau+\beta) \end{aligned}$$

By comparing equation 5.18 with equation 5.4 and applying equation 5.17, one obtains

$$\alpha_v = \frac{32\omega_s a_3}{a_1^3} \tag{5.19}$$

$$\mu_v = \frac{1}{4}\alpha_v a_1^2 \tag{5.20}$$

$$\xi = \frac{a_2(2\omega_s - \Omega)2\Omega}{a_1} \tag{5.21}$$

or

$$\xi = \frac{a_4(2\omega_s + \Omega)2\Omega}{a_1} \tag{5.22}$$

Alternatively, and as explained above, α_v and ξ can be obtained from the magnitude of the auto-trispectra defined in equations 5.13 and 5.14. Rearranging equation 5.13, one obtains

$$\alpha_v = \frac{512\omega_s \left|S_{llll}(\omega_s, \omega_s, \omega_s)\right|}{a^6} \tag{5.23}$$

and rearranging equation 5.14, one obtains

$$\xi = \sqrt{\frac{64\Omega^2(2\omega_s - \Omega)(2\omega_s + \Omega)\left|S_{llll}(\Omega - \omega_s, \omega_s, \omega_s)\right|}{a^4}} \tag{5.24}$$

From the Fourier transform of $l(t)$ at frequency $\Omega - \omega_s$, $\Omega + \omega_s$ and ω_s, one can detrmine the phase of the parametric excitation τ which is given by

$$\tau = \Phi(L(\Omega - \omega_s)) + \Phi(L(\omega_s)) - \pi \tag{5.25}$$

or

$$\tau = \Phi(L(\Omega + \omega_s)) - \Phi(L(\omega_s)) \tag{5.26}$$

where $\Phi(L(\omega_s))$ is the phase angle of $L(\omega_s)$, $\Phi(L(\Omega - \omega_s))$ is the phase angle of $L(\Omega - \omega_s)$, and $\Phi(L(\Omega + \omega_s))$ is the phase angle of $L(\Omega + \omega_s)$.

Results and Discussion

The power spectrum of the lift coefficient on the inline oscillating cylinder, obtained from the RANS siumlation at an excitation frequency of 0.4 Hz and amplitude near 0.01 is shown in figure 5.1. In this figure, peaks at ω_s, $3\omega_s$, $\Omega - \omega_s$, and $\Omega + \omega_s$ are noted. These peaks show that there is no resonance under these conditions. The auto-trispectrum plot, presented in figure 5.2, clearly shows that the vortex shedding frequency component, ω_s, is coupled with its third harmonic, $3\omega_s$. The auto-tricoherence plot, presented in figure 5.3, shows that other modes are coupled. Two triplets of these modes include , $(\omega_s, \omega_s, \omega_s)$ and $(\Omega - \omega_s, \omega_s, \omega_s)$. The amplitude and phase of the auto-trispectra at $(\omega_s, \omega_s, \omega_s)$ and $(\Omega - \omega_s, \omega_s, \omega_s)$ are given in Table 5.1. The phase relation, $\phi(3\omega_s) - 3\phi(\omega_s)$, is near $\pi/2$ which indicates, and based on the approximate solutions and equation 5.13, that the van der Pol equation should be used to model the lift on the inline oscillating cylinder. The phase relation, $\phi(\Omega + \omega_s) - 2\phi(\omega_s) - \phi(\Omega - \omega_s)$, is near $-\pi$ which indicates, and based on the aproximate solutions and equation 5.14, that the parametrically excited van der Pol equation should be used to model the lift on the inline oscillating cylinder.

Values of the spectral parameters f, a_1, a_2, a_3 a_4, $\Phi(L(\omega_s))$, $\Phi(L(\Omega - \omega_s))$, and $\Phi(L(\Omega + \omega_s))$ are shown in Table 5.2. These values are used to estimate ξ, τ, μ_v and α_v based on equations 5.19, 5.20, 5.23, and 5.25. These parameters are given in Table 5.3. They can be used to predict the steady-state lift by integrating equation 5.1.

To verify the lift coefficient model, we not only compare the simulated and modeled time series for lift coefficients, but also validate the physics of the simulated and modeled lift coefficients. Specifically, we compare the power spectra and auto-trispectra. Comparisons of the simulated and modeled lift coefficients in both time and frequency domains are shown in figures 5.4 - 5.7. Comparison of the two time series in figure 5.4 shows that the identified parameters can be used to correctly determine the amplitude variations in the lift time series. This conclusion is strengthened by the comparison of the power spectra presented in figure 5.5, which shows that the model accounts for all peaks. The trispectra and tricoherence estimates, presented in figures 5.6 and 5.7, show that both RANS simulated and modeled time series are characterized by the same cubic nonlinearities.

5.1.2 Case of Subharmonic Resonance ($\Omega \approx 2\omega$)

Using the method of multiple scales, an analytical approximate solution is derived for equation 5.3 for the subharmonic resonance condition set by

$$\Omega = 2\omega_s + \epsilon\sigma \tag{5.27}$$

Table 5.1: Lift auto-trispectra for the inline oscillating cylinder - amplitude and phase (no resonance case)

$\Omega(Hz)$	0.4	0.4
$\frac{y}{D}$	0.01	0.01
$f_1(Hz)$	0.2393	0.1607
$f_2(Hz)$	0.2393	0.2393
$f_3(Hz)$	0.2393	0.2393
Amplitude	0.0156	9.01e-5
Phase(rad)	1.74	-3.20

Table 5.2: Lift spectral parameters for the inline oscillating cylinder (no resonance case)

$\Omega(Hz)$	0.4
$\frac{y}{D}$	0.01
$f(Hz)$	0.2393
a_1	1.77
a_2	0.075
a_3	0.045
a_4	0.0069
$\Phi(L(\omega_s))(rad)$	2.18
$\Phi(L(\Omega-\omega_s))(rad)$	1.86
$\Phi(L(\Omega+\omega_s))(rad)$	3.02

Table 5.3: Lift model parameters in parametrically excited van der Pol equation (no resonance case)

$\Omega(Hz)$	0.4
$\frac{y}{D}$	0.01
$f(Hz)$	0.2393
ξ from $L(\Omega-\omega_s)$	0.099
ξ from $L(\Omega+\omega_s)$	0.101
$\tau(rad)$	0.9
μ_v	0.3058
α_v from $L(3\omega_s)$	0.3904
α_v from S_{llll}	0.3943

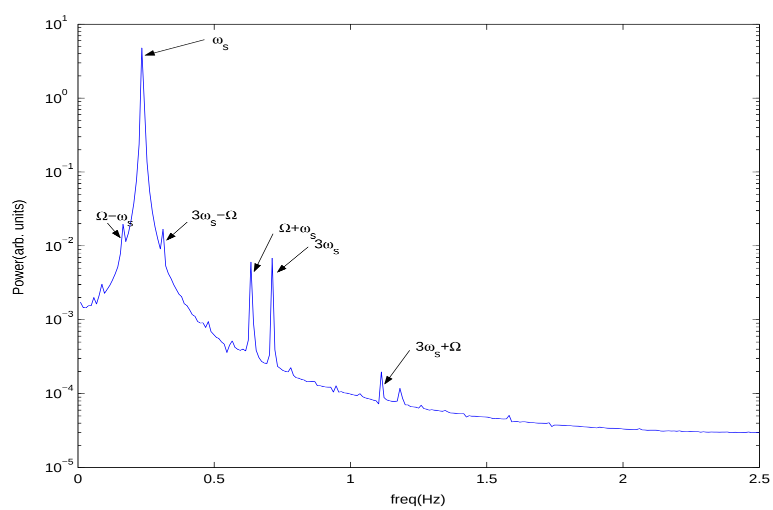

Figure 5.1: Power spectrum of the lift coefficient for the inline oscillating cylinder at frequency $\Omega = 0.4Hz$ and amplitude $\frac{y}{D} = 0.01$

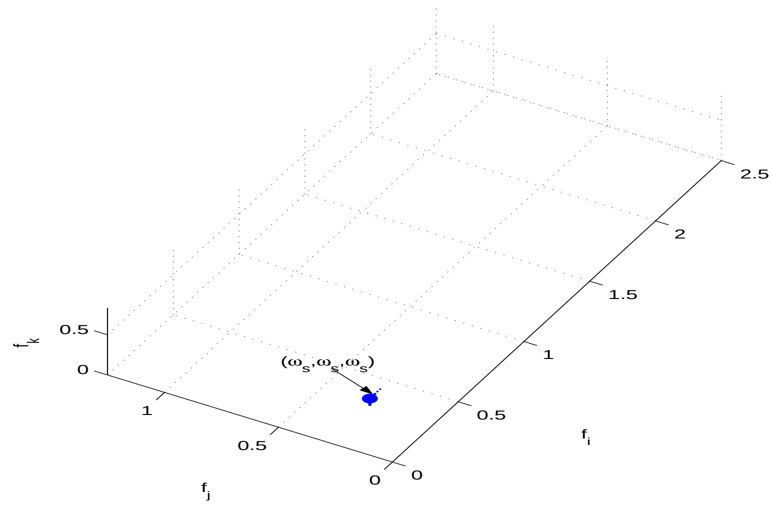

Figure 5.2: Auto-trispectrum of the lift coefficient for the inline oscillating cylinder at the frequency $\Omega = 0.4Hz$ and amplitude $\frac{y}{D} = 0.01$

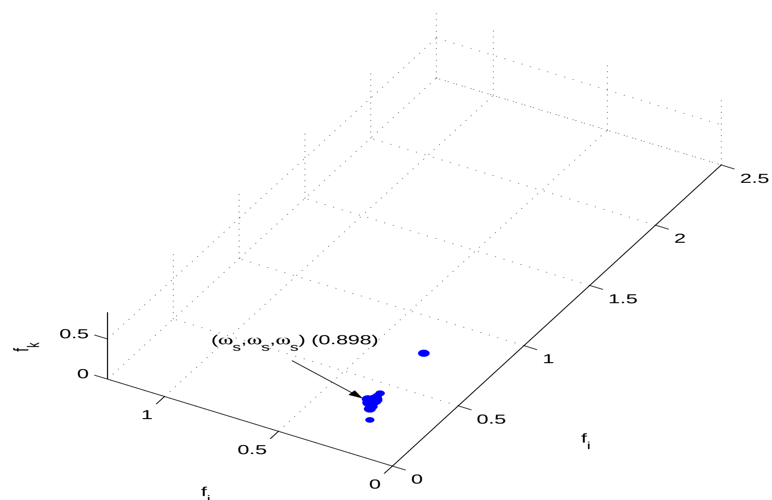

Figure 5.3: Auto-tricoherence of the lift coefficient for the inline oscillating cylinder at the frequency $\Omega = 0.4Hz$ and amplitude $\frac{y}{D} = 0.01$

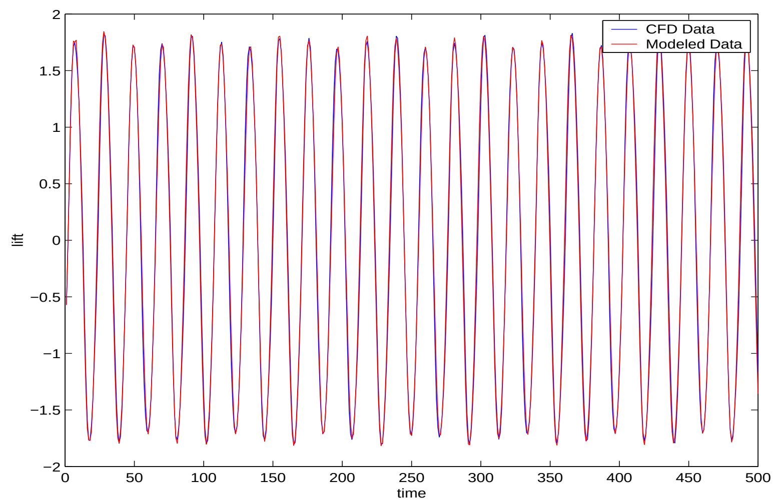

Figure 5.4: Comparison of RANS simulated and modeled time series of the lift coefficients for the inline oscillating cylinder $\Omega = 0.4Hz$ and amplitude $\frac{y}{D} = 0.01$

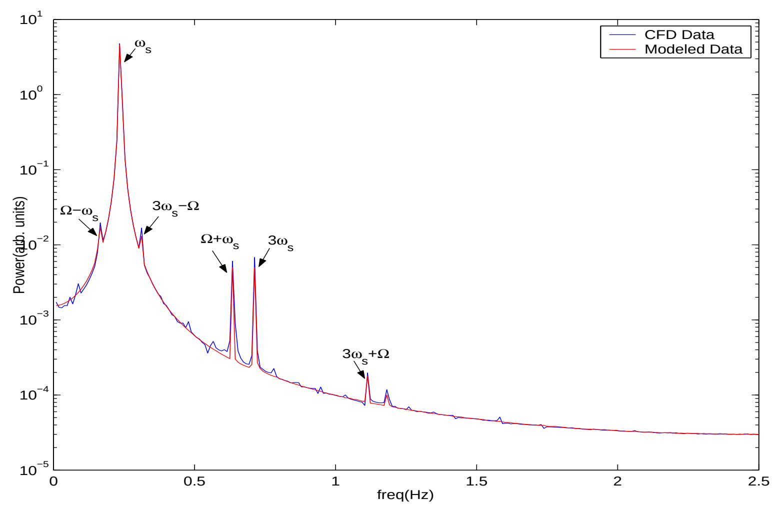

Figure 5.5: Comparison of power spectra of the RANS simulated and modeled lift coefficients for the inline oscillating cylinder at the frequency $\Omega = 0.4Hz$ and amplitude $\frac{y}{D} = 0.01$

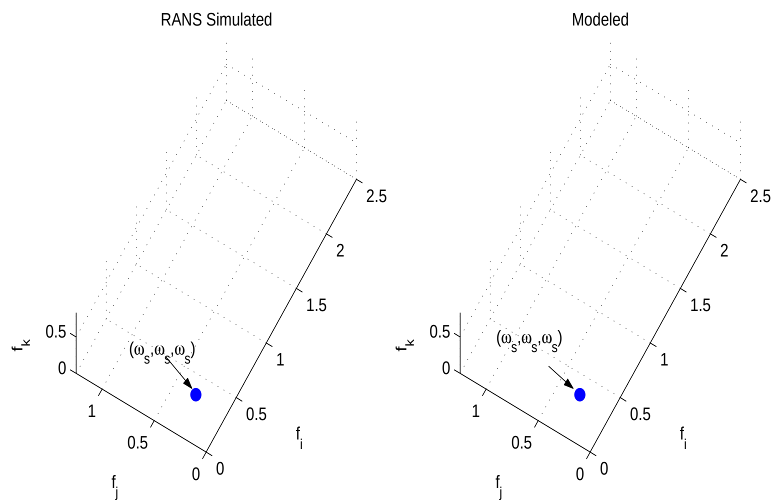

Figure 5.6: Comparison of auto-trispectra of the RANS simulated and modeled lift coefficients for the inline oscillating cylinder at the frequency $\Omega = 0.4Hz$ and amplitude $\frac{y}{D} = 0.01$

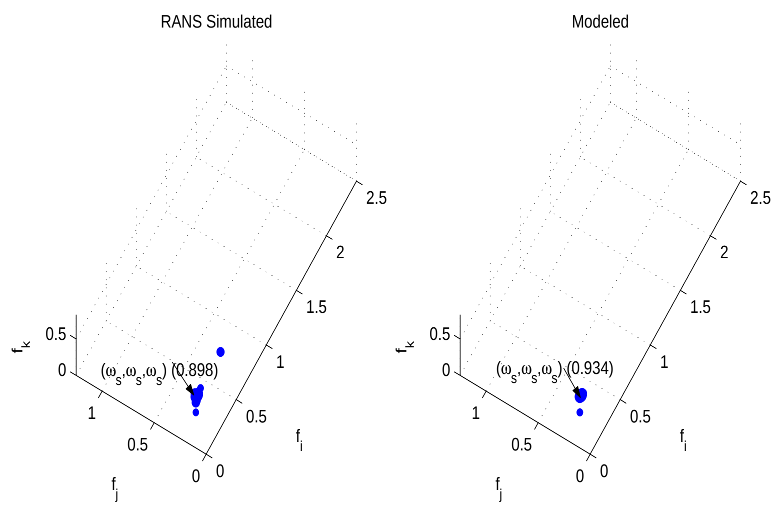

Figure 5.7: Comparison of auto-tricoherence of the RANS simulated and modeled lift coefficients for the inline oscillating cylinder at the frequency $\Omega = 0.4Hz$ and amplitude $\frac{y}{D} = 0.01$

where σ is the detuning parameter. Under this condition, the approximate solution is of the form

$$
\begin{aligned}
l(t) \approx \quad & acos(\tfrac{\Omega}{2}t + \tfrac{\tau}{2} - \tfrac{\gamma}{2}) + \tfrac{a^3\alpha_v}{32\omega_s} cos(3(\tfrac{\Omega}{2}t + \tfrac{\tau}{2} - \tfrac{\gamma}{2}) + \tfrac{\pi}{2}) \\
& + \tfrac{a\xi}{16\omega_s^2} cos(\tfrac{3\Omega}{2}t + \tfrac{3\tau}{2} - \tfrac{\gamma}{2}) \\
& + \tfrac{a^3\alpha_v\xi}{256\omega_s^3} cos(\tfrac{5\Omega}{2}t + \tfrac{5\tau}{2} - \tfrac{3\gamma}{2} + \tfrac{\pi}{2}) \\
& + \tfrac{a\xi^2}{768\omega_s^4} cos(\tfrac{5\Omega}{2}t + \tfrac{5\tau}{2} - \tfrac{\gamma}{2})
\end{aligned}
\tag{5.28}
$$

where γ is given by

$$
\gamma = \epsilon\sigma t + \tau - 2\beta \tag{5.29}
$$

In equation 5.28, the amplitude a and phase γ are governed by

$$
\begin{aligned}
\dot{a} &= \tfrac{\mu_v}{2}a - \tfrac{\alpha_v}{8}a^3 - \tfrac{a\xi}{4\omega_s} sin\gamma \\
\dot{\gamma} &= \sigma - \tfrac{\xi}{2\omega_s} cos\gamma
\end{aligned}
\tag{5.30}
$$

An examination of the expression for γ reveals its dependency on the phase of parametric excitation, τ and the phase of the response, β.

When a and γ in equation 5.30 are constants, i.e., for steady-state oscillations, the solution given in equation 5.28 represents a periodic motion which can be written in complex form as

$$\begin{aligned} l(t) \approx\ & \tfrac{a}{2}\{e^{i(\frac{\Omega}{2}t+\frac{\tau}{2}-\frac{\gamma}{2})} + e^{-i(\frac{\Omega}{2}t+\frac{\tau}{2}-\frac{\gamma}{2}}\} \\ & +\tfrac{a^3\alpha_v}{64\omega_s}\{e^{3i(\frac{\Omega}{2}t+\frac{\tau}{2}-\frac{\gamma}{2})+i\frac{\pi}{2}} + e^{-3i(\frac{\Omega}{2}t+\frac{\tau}{2}-\frac{\gamma}{2})-i\frac{\pi}{2}}\} \\ & +\tfrac{a\xi}{32\omega_s^2}\{e^{i\frac{3\Omega}{2}t+i\frac{3\tau}{2}-i\frac{\gamma}{2})} + e^{-i\frac{3\Omega}{2}t-i\frac{3\tau}{2}+i\frac{\gamma}{2})}\} \\ & +\tfrac{a^3\alpha_v\xi}{512\omega_s^3}\{e^{i\frac{5\Omega}{2}t+i\frac{5\tau}{2}-i\frac{3\gamma}{2}+i\frac{\pi}{2}} + e^{-i\frac{5\Omega}{2}t-i\frac{5\tau}{2}+i\frac{3\gamma}{2}-i\frac{\pi}{2}}\} \\ & +\tfrac{a\xi^2}{1536\omega_s^4}\{e^{i\frac{5\Omega}{2}t+i\frac{5\tau}{2}-i\frac{\gamma}{2}} + e^{-i\frac{5\Omega}{2}t-i\frac{5\tau}{2}+i\frac{\gamma}{2}}\} \end{aligned} \tag{5.31}$$

The Fourier transform of $l(t)$, represented by $L(\omega)$, is then given by

$$\begin{aligned} l(t) \approx\ & \tfrac{a}{2}\{e^{i(\frac{\tau}{2}-\frac{\gamma}{2})}\delta(\omega-\tfrac{\Omega}{2}) + e^{-i(\frac{\tau}{2}-\frac{\gamma}{2}}\delta(\omega+\tfrac{\Omega}{2})\} \\ & +\tfrac{a^3\alpha_v}{64\omega_s}\{e^{3i(\frac{\tau}{2}-\frac{\gamma}{2})+i\frac{\pi}{2}}\delta(\omega-\tfrac{3\Omega}{2}) + e^{-3i(\frac{\tau}{2}-\frac{\gamma}{2})-i\frac{\pi}{2}}\delta(\omega+\tfrac{3\Omega}{2})\} \\ & +\tfrac{a\xi}{32\omega_s^2}\{e^{i\frac{3\tau}{2}-i\frac{\gamma}{2}}\delta(\omega-\tfrac{3\Omega}{2}) + e^{-i\frac{3\tau}{2}+i\frac{\gamma}{2}}\delta(\omega+\tfrac{3\Omega}{2})\} \\ & +\tfrac{a^3\alpha_v\xi}{512\omega_s^3}\{e^{i\frac{5\tau}{2}-i\frac{3\gamma}{2}+i\frac{\pi}{2}}\delta(\omega-\tfrac{5\Omega}{2}) + e^{-i\frac{5\tau}{2}+i\frac{3\gamma}{2}-i\frac{\pi}{2}}\delta(\omega+\tfrac{5\Omega}{2})\} \\ & +\tfrac{a\xi^2}{1536\omega_s^4}\{e^{i\frac{5\tau}{2}-i\frac{\gamma}{2}}\delta(\omega-\tfrac{5\Omega}{2}) + e^{-i\frac{5\tau}{2}+i\frac{\gamma}{2}}\delta(\omega+\tfrac{5\Omega}{2})\} \end{aligned} \tag{5.32}$$

Examining the expression for $L(\omega)$, it is noted that the solution contains components with frequencies at $\frac{\Omega}{2}$, $\frac{3\Omega}{2}$ and $\frac{5\Omega}{2}$. In terms of their amplitudes and phases, these components are written as

$$L(\frac{\Omega}{2}) \quad = \quad \frac{a}{2}e^{i(\frac{\tau}{2}-\frac{\gamma}{2})} \tag{5.33}$$

$$L(\frac{3\Omega}{2}) \quad = \quad \frac{a^3\alpha_v}{64\omega_s}e^{3i(\frac{\tau}{2}-\frac{\gamma}{2})+i\frac{\pi}{2}} + \frac{a\xi}{32\omega_s^2}e^{i\frac{3\tau}{2}-i\frac{\gamma}{2}} \tag{5.34}$$

and

$$L(\frac{5\Omega}{2}) \quad = \quad \frac{a^3\alpha_v\xi}{512\omega_s^3}e^{i\frac{5\tau}{2}-i\frac{3\gamma}{2}+i\frac{\pi}{2}} + \frac{a\xi^2}{1536\omega_s^4}e^{i\frac{5\tau}{2}-i\frac{\gamma}{2}} \tag{5.35}$$

The auto-trispectrum defined in equation 2.17 and given by

$$S_{llll}(\omega_k, \omega_l, \omega_m) = \lim_{T\to\infty}\frac{1}{T}E[L^*(\omega_k)L_*(\omega_l)L_*(\omega_m)L(\omega_{k+l+m})] \tag{5.36}$$

yields the following expression for $\omega_k = \omega_l = \omega_m = \frac{\Omega}{2}$

$$S_{llll}(\frac{\Omega}{2}, \frac{\Omega}{2}, \frac{\Omega}{2}) \approx \frac{a^6\alpha_v}{512\omega_s}e^{i\frac{\pi}{2}} + \frac{a^4\xi}{256\omega_s^2} \tag{5.37}$$

The magnitude and phase of the auto-trispectrum $S_{llll}(\frac{\Omega}{2}, \frac{\Omega}{2}, \frac{\Omega}{2})$ depend on the coefficient of the cubic nonlinearity α_v and the parametric excitation coefficient ξ. The real part of the auto-trispectrum $S_{llll}(\frac{\Omega}{2}, \frac{\Omega}{2}, \frac{\Omega}{2})$, can be used to identify ξ. The imaginary part of the auto-trispectrum $S_{llll}(\frac{\Omega}{2}, \frac{\Omega}{2}, \frac{\Omega}{2})$, can be used to identify α_v.

The normalized auto-trispectrum, namely, the auto-tricoherence for ($\omega_k = \omega_l = \omega_m = \frac{\Omega}{2}$) is written as

$$t^2(\tfrac{\Omega}{2},\tfrac{\Omega}{2},\tfrac{\Omega}{2}) \approx \frac{\left|S_{llll}(\frac{\Omega}{2},\frac{\Omega}{2},\frac{\Omega}{2})\right|^2}{\left|L(\frac{\Omega}{2})L(\frac{\Omega}{2})L(\frac{\Omega}{2})\right|^2\left|L(\frac{3\Omega}{2})\right|^2} \tag{5.38}$$

A unit value of the auto-tricoherence indicates perfect cubic phase coupling. A zero value indicates no coupling and any value in between indicates partial coupling. The auto-tricoherence is a necessary quantity that should be used to determine the extent of couping in a time series and the validity of using the magnitude and phase of the trispectrum to model physical phenomenon by the van der Pol equation.

For the parametrically excited van der Pol equation with the case of subharmonic resonance ($\Omega \approx 2\omega_s$), the steady-state value of the amplitude a and phase γ can be obtained by setting $\dot{a} = 0$ and $\dot{\gamma} = 0$ in equation 5.30. That is

$$\begin{aligned} 0 &= \tfrac{\mu_v}{2}a - \tfrac{\alpha_v}{8}a^3 - \tfrac{a\xi}{4\omega_s}sin\gamma \\ 0 &= \sigma - \tfrac{\xi}{2\omega_s}cos\gamma \end{aligned} \tag{5.39}$$

In order to determine the damping and nonlinear coefficients, as well as the excitation coefficient in the parametrically excited van der Pol equation, we represent the lift coefficient as

$$l(t) \approx \quad a_1cos(\tfrac{\Omega}{2}t + \beta_1) + a_3cos(\tfrac{3\Omega}{2}t + \beta_3)) + a_5cos(\tfrac{5\Omega}{2}t + \beta_5) \tag{5.40}$$

By comparing equation 5.40 with equation 5.28, and using equations 5.30 and 5.37, one obtains

$$\alpha_v = \frac{512\omega_s Im[S_{llll}(\frac{\Omega}{2},\frac{\Omega}{2},\frac{\Omega}{2})]}{a_1^6} \tag{5.41}$$

$$\xi = \frac{256\omega_s^2 Re[S_{llll}(\frac{\Omega}{2},\frac{\Omega}{2},\frac{\Omega}{2})]}{a_1^4} \tag{5.42}$$

$$cos\gamma = \sigma\frac{2\omega_s}{\xi} \tag{5.43}$$

$$\mu_v = \frac{1}{4}\alpha_v a_1^2 + \frac{\xi}{2\omega_s}sin\gamma \tag{5.44}$$

and

$$\tau = 2\Phi(L(\frac{\Omega}{2})) + \gamma \tag{5.45}$$

where $\Phi(L(\frac{\Omega}{2}))$ is the phase of the frequency component $L(\frac{\Omega}{2})$. The set of equations 5.41 - 5.45 shows how the different spectral parameters can be used to predict the parameters of the model presented in equation 5.1.

Results and Discussion

The power spectrum of the lift coefficient on the inline oscillating cylinder, obtained from the RANS siumlation at an excitation frequency of 0.4 Hz and amplitude near 0.064, is shown in figure 5.8. The spectral peaks at $\frac{\Omega}{2}$, $\frac{3\Omega}{2}$, and $\frac{5\Omega}{2}$ indicate that this is a case of subharmonic resonance. The auto-trispectrum presented in figure 5.9 shows that the frequency component at $\frac{\Omega}{2}$ is coupled with its third harmonic. The extent of this coupling is shown in the auto-tricoherence plot presented in figure 5.10. The amplitude and phase of the autotrispectrum corresponding to this coupling are given in Table 5.4.

Values of f, a_1, a_3 a_5, and $\Phi(L(\frac{\Omega}{2}))$, as obtained from the spectral analysis, are shown in Table 5.5. These values along with the amplitude and phase of the auto-trispectrum, shown in Table 5.4, are used to estimate ξ, τ, γ, μ_v and α_v based on equations 5.41 - 5.45. The results are presented in Table 5.5.

Values of the parameters presented in Table 5.6 were then used to predict the steady-state lift by integrating equation 5.1. To verify the lift coefficient model, we not only compare the simulated and modeled time series for lift coefficients, but also validate the physics of the simulated and modeled lift coefficients. Specifically, we compare the power spectra and auto-trispectra. A comparison of the time series is presented in figure 5.11. The results clearly show that the parametric excitation model along with the derived parameters yield the right frequency and amplitude variations. This argument is further strengthened by the comparison of the power spectra of the RANS simulated and modeled time series which is presented in figure 5.12. The results show that the model correctly predicts all frequency components and their amplitudes. The auto-trispectra and auto-tricoherence plots presented in figures 5.13 and 5.14 show that the model can predict the important cubic interactions as identified in the RANS simulations.

5.2 Drag Model for Inline Oscillating Cylinder

Because the coupling between the drag and lift coefficients is quadratic and based on equation 3.3, the drag coefficient is modeled as

$$d = (d_m - c_1) + k_2 l^2 + k_1 cos(\Omega t + \tau_e) \tag{5.46}$$

Where d_m is the mean drag and can be obtained independently as a mean value from the time series of the drag. To determine the coefficient k_1 and

Table 5.4: Lift auto-trispectrum for the inline oscillating cylinder - amplitude and phase (resonance case)

$\Omega(Hz)$	0.4
$\frac{y}{D}$	0.064
$f_1(Hz)$	0.2
$f_2(Hz)$	0.2
$f_3(Hz)$	0.2
Amplitude	0.0273
Phase(rad)	0.1326

Table 5.5: Lift spectral parameters for the inline oscillating cylinder (resonance case)

$\Omega(Hz)$	0.4
$\frac{y}{D}$	0.064
$f(Hz)$	0.2
a_1	1.88
a_3	0.224
a_5	0.0444
$\Phi(L(\frac{\Omega}{2}))(rad)$	1.25

Table 5.6: Lift model parameters in parametrically excited van der Pol equation (resonance case)

$\Omega(Hz)$	0.4
$\frac{y}{D}$	0.064
$f(Hz)$	0.2
ξ from S_{llll}	0.12
$\tau(rad)$	0.95
μ_v	0.30
α_v from S_{llll}	0.3935

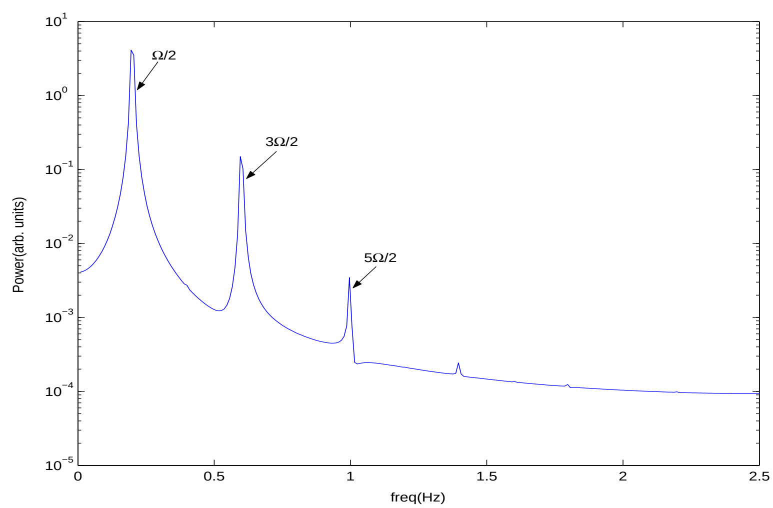

Figure 5.8: Power spectrum of the lift coefficient for the inline oscillating cylinder at frequency $\Omega = 0.4Hz$ and amplitude $\frac{y}{D} = 0.064$

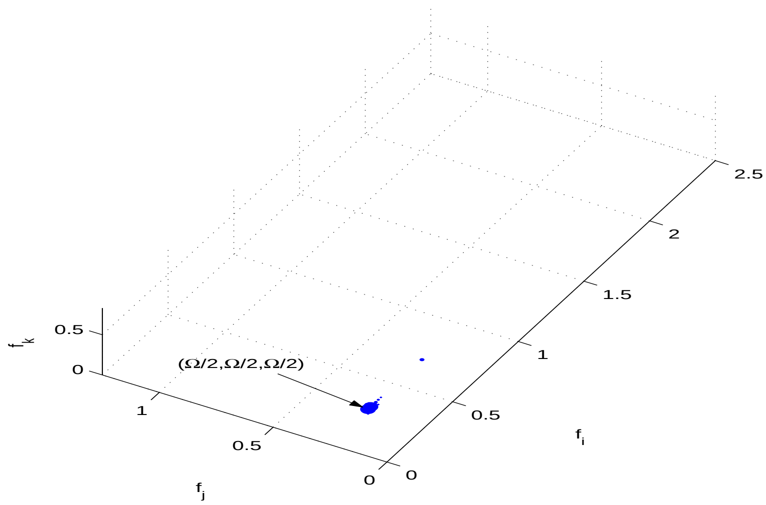

Figure 5.9: Auto-trispectrum of the lift coefficient for the inline oscillating cylinder at the frequency $\Omega = 0.4Hz$ and amplitude $\frac{y}{D} = 0.064$

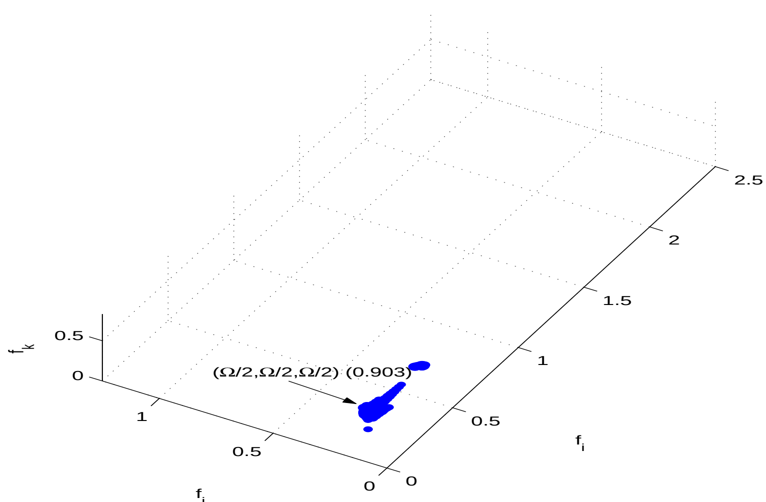

Figure 5.10: Auto-tricoherence of the lift coefficient for the inline oscillating cylinder at the frequency $\Omega = 0.4Hz$ and amplitude $\frac{y}{D} = 0.064$

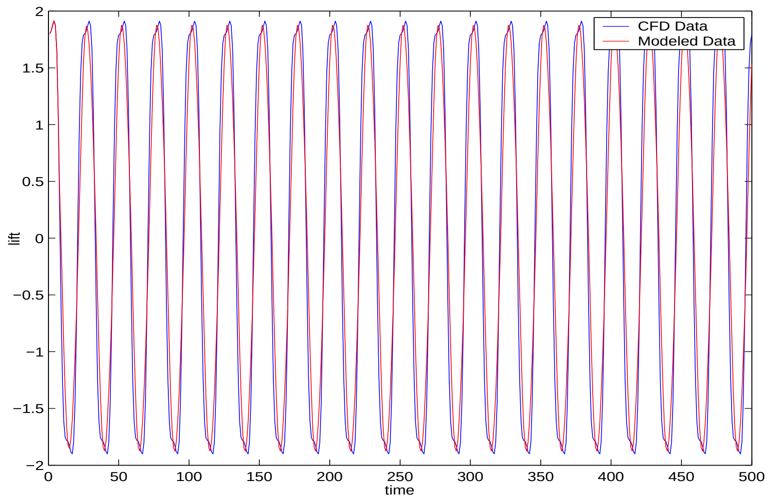

Figure 5.11: Comparison of RANS simulated and modeled time series of the lift coefficients for the inline oscillating cylinder $\Omega = 0.4Hz$ and amplitude $\frac{y}{D} = 0.064$

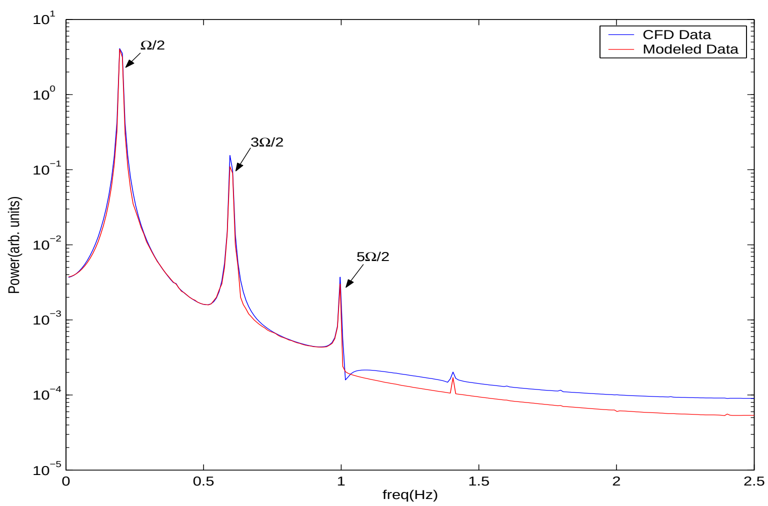

Figure 5.12: Comparison of power spectra of the RANS simulated and modeled lift coefficients for the inline oscillating cylinder at the frequency $\Omega = 0.4Hz$ and amplitude $\frac{y}{D} = 0.064$

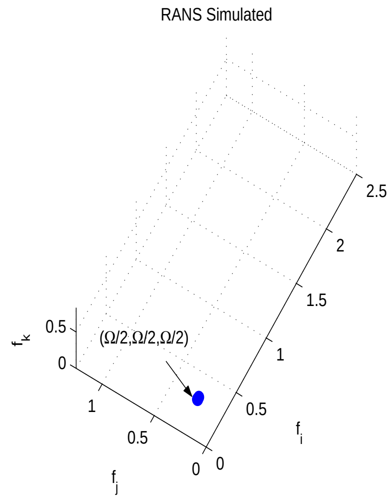

Figure 5.13: Comparison of auto-trispectra of the RANS simulated and modeled lift coefficients for the inline oscillating cylinder at the frequency $\Omega = 0.4Hz$ and amplitude $\frac{y}{D} = 0.064$

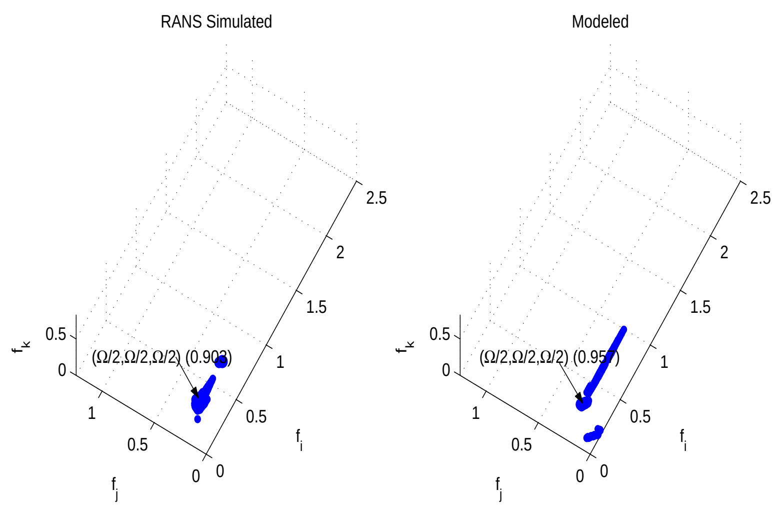

Figure 5.14: Comparison of auto-tricoherence of the RANS simulated and modeled lift coefficients for the inline oscillating cylinder at the frequency $\Omega = 0.4Hz$ and amplitude $\frac{y}{D} = 0.064$

k_2 in equation 5.46, we introduce the effective drag coefficient, $\hat{d}$, defined as

$$\hat{d} = d - k_1 cos(\Omega t + \tau_e) \tag{5.47}$$

By letting $\hat{D}$ represent the Fourier transform of the effective drag coefficient $\hat{d}$ and L represent the Fourier transform of the lift coefficient l, the phase of the cross-bispectrum between any two frequencies in the lift coefficient and their sum or difference in the effective drag coefficient, defined as,

$$\hat{B}(\omega_1, \omega_2) = L(\omega_1)L(\omega_2)\hat{D}^*(\omega_1 + \omega_2) \tag{5.48}$$

is -$\pi/2$.

According to the properties of Fourier transform and equation 5.47, one obtains

$$\hat{D}(\omega) = D(\omega) + k_1 e^{\tau_e}\delta(\omega - \Omega) \tag{5.49}$$

where D represents the Fourier transform of the drag coefficient d. Consequently,

$$\hat{B}(\omega_1, \omega_2) = L(\omega_1)L(\omega_2)\{D^*(\omega_1 + \omega_2) + k_1 e^{-i\tau_e}\delta(\omega_1 + \omega_2 - \Omega)\} \tag{5.50}$$

For the case of subharmonic resonance, substituting ω_1 and ω_2 with $\frac{\Omega}{2}$, one obtains

$$\hat{B}(\frac{\Omega}{2}, \frac{\Omega}{2}) = L(\frac{\Omega}{2})L(\frac{\Omega}{2})\{D^*(\Omega) + k_1 e^{-i\tau_e}\} \tag{5.51}$$

For the case of no-resonance, substituting ω_1 and ω_2 with ω_s and $\Omega - \omega_s$ respectively, one obtains

$$\hat{B}(\omega_s, \Omega - \omega_s) = L(\omega_s)L(\Omega - \omega_s)\{D^*(\Omega) + k_1 e^{-i\tau_e}\} \tag{5.52}$$

Expressing the different Fourier components and their bispectral moments in terms of their respective amplitudes and phases, i.e.

$$\begin{aligned} L(\frac{\Omega}{2}) &= a_1 e^{i\beta_1} && (5.53)\\ L(\omega_s) &= a_2 e^{i\beta_2} && (5.54)\\ L(\Omega-\omega_s) &= a_{21} e^{i\beta_{21}} && (5.55)\\ B(\frac{\Omega}{2},\frac{\Omega}{2}) &= L(\frac{\Omega}{2})L(\frac{\Omega}{2})D^*(\Omega) = B_0 e^{ib_0} && (5.56)\end{aligned}$$

and

$$B(\omega_s,\Omega-\omega_s) = L(\omega_s)L(\Omega-\omega_s)D^*(\Omega) = B_1 e^{ib_1} \quad (5.57)$$

The cross-bispectrum for the case of resonance is re-written as

$$\begin{aligned} \hat{B}(\tfrac{\Omega}{2},\tfrac{\Omega}{2}) &= B_0 e^{ib_0} + a_1 e^{i\beta_1} a_1 e^{i\beta_1} k_1 e^{-i\tau_e}\\ &= B_0 e^{ib_0} + a_1^2 k_1 e^{i(2\beta_1-\tau_e)}\\ &= [B_0 cos(b_0) + a_1^2 k_1 cos(2\beta_1-\tau_e)]\\ &\quad +[B_0 sin(b_0) + a_1^2 k_1 sin(2\beta_1-\tau_e)] \end{aligned} \quad (5.58)$$

Similarly the cross-bispectrum for the no-resonance case is re-written as

$$\begin{aligned} \hat{B}(\omega_s,\Omega-\omega_s) &= B_1 e^{ib_1} + a_2 e^{i\beta_2} a_{21} e^{i\beta_{21}} k_1 e^{-i\tau_e}\\ &= B_1 e^{ib_1} + a_2 a_{21} k_1 e^{i(\beta_2+\beta_{21}-\tau_e)}\\ &= [B_1 cos(b_1) + a_2 a_{21} k_1 cos(\beta_2+\beta_{21}-\tau_e)]\\ &\quad +[B_1 sin(b_1) + a_2 a_{21} k_1 sin(\beta_2+\beta_{21}-\tau_e)] \end{aligned} \quad (5.59)$$

Because the phase of $\hat{B}(\frac{\Omega}{2},\frac{\Omega}{2})$ is equal to -$\frac{\pi}{2}$ and the phase of $\hat{B}(\omega_s,\Omega-\omega_s)$ is also equal to -$\frac{\pi}{2}$, one can write

$$B_0 cos(b_0) + a_1^2 k_1 cos(2\beta_1-\tau_e) = 0 \quad (5.60)$$

and

$$B_1 cos(b_1) + a_2 a_{21} k_1 cos(\beta_2 + \beta_{21} - \tau_e) = 0 \tag{5.61}$$

Consequently, for the case of subharmonic resonance, one obtains

$$k_1 = -\frac{B_0 cos(b_0)}{a_1^2 cos(2\beta_1 - \tau_e)} \tag{5.62}$$

and for the case of no-resonance, one obtains

$$k_1 = -\frac{B_1 cos(b_1)}{a_2 a_{21} cos(\beta_2 + \beta_{21} - \tau_e)} \tag{5.63}$$

Equations 5.62 and 5.63 give two relations from which k_1 in equation 5.46 can be determined for both cases of resonance and no resonance. Once k_1 is identified, k_2 and c_1 can be identified via fitting a straight line according

$$\hat{d} = \hat{c}_1 + k_2 \hat{l} \tag{5.64}$$

where $\hat{c}_1 = d_m - c_1$, $\hat{l} = l^2$ and $\hat{d} = d - k_1 cos(\Omega t + \tau_e)$

Results and Discussion

The power spectrum of the drag coefficient on the inline oscillating cylinder, obtained from the RANS siumlation at an excitation frequency of 0.4 Hz and amplitude near 0.01 is shown in figure 5.15. This is the case of no resonance and the peaks at frequency components $2\omega_s$, $2\omega_s - \Omega$, $2\omega_s + \Omega$, $4\omega_s - \Omega$, $4\omega_s + \Omega$, $4\omega_s$, and Ω imply amplitude and peak modulations of the vortex shedding frequency. The cross-bispectrum and cross-bicoherence contour plots between the lift and drag, presented in figures 5.16 and 5.17, show high level of coupling between the peaks in the power spectrum.

The power spectrum of the drag coefficient on the inline oscillating cylinder, obtained from the RANS siumlation at an excitation frequency of 0.4 Hz and amplitude near 0.064, is shown in figure 5.18. The spectrum shows clear peaks at the excitation component Ω and its harmonics 2Ω, 4Ω and 6Ω. Other peaks at $\frac{\Omega}{2}$, $\frac{3\Omega}{2}$, and $\frac{5\Omega}{2}$ are also noted. The cross-bispectrum and cross-bicoherence contour plots between the lift and drag coefficients, presented in figures 5.19 and 5.20, show high level of quadratic coupling between $\frac{\Omega}{2}$ and $\frac{\Omega}{2}$ in the lift time series and Ω in the drag time series. These couplings extend to the sidebands. Lower levels of coupling are detected between the other peaks noted in the power spectrum.

In Table 5.7, the amplitude and phase of the cross-bispectrum between the coupled compoents for both cases of resonance and no resonance are presented. Other spectral values for Ω, $|L(\omega_s)|$, $\Phi(L(\omega_s))$, $|L(\Omega - \omega_s)|$, $\Phi(L(\Omega - \omega_s))$, $|L(\frac{\Omega}{2})|$, $\Phi(L(\frac{\Omega}{2}))$, $\Phi(L(\frac{\Omega}{2}))$ are presented in Table 5.8. The spectral parameters in Table 5.8 were used to estimate k_1 and k_2 based on equations 5.62, 5.63, and 5.64. The estimates for these parameters along with the constants d_m and c_1 are presented in Table 5.9.

The parameters presented in Table 5.9 were used to predict the drag coefficient by applying equation 5.46. Figure 5.21 shows a comparison of the RANS simulated and modeled time series for the case of no resonance. The results clearly show the effectiveness of the model in predicting both amplitude and phase modulations of the drag coefficient. A comparison of the spectra for both time series in figure 5.22 shows that the model correctly predicts the amplitudes of all spectral peaks. Figures 5.23 and 5.24 which present a comparison of the cross-bispectrum and cross-bicoherence show

Table 5.7: Lift-drag cross-bispectrum for the inline oscillating cylinder - amplitude and phase (no resoance and resonance cases)

$\Omega(Hz)$	0.4	0.4
$\frac{y}{D}$	0.01	0.064
$f_1(Hz)$	0.2393	0.2
$f_2(Hz)$	0.1607	0.2
Amplitude	9.13e-4	0.1767
Phase(rad)	2.341	-2.34

that the model is characterized by the same nonlinearities present in the simulated time series. As for the resonance case, figure 5.25 shows that the modeled time series correctly predicts the time variations of the drag coefficient. This is further strengthened by a comparison of the power spectrum presented in figure 5.26. This figure shows that the modeled time series contains peaks with the same amplitude levels as the RANS simulated time series. The comparison of the cross-bispectra and cross-bicoherence contour plots, presented in figures 5.27 and 5.28, shows that the model accounts for all quadratic nonlinearities in the RANS simulated time series.

Table 5.8: Drag spectral parameters for the inline oscillating cylinder (no resonance and resonance cases)

$\Omega(Hz)$	0.4	0.4
$\frac{y}{D}$	0.01	0.064
$\lvert L(\omega_s)\rvert$	0.885	N/A
$\Phi(L(\omega_s))(rad)$	2.18	N/A
$\lvert L(\frac{\Omega}{2})\rvert$	N/A	0.94
$\Phi(L(\frac{\Omega}{2}))(rad)$	N/A	1.25
$\lvert L(\Omega-\omega_s)\rvert$	0.0375	N/A
$\Phi(L(\Omega-\omega_s))(rad)$	1.86	N/A

Table 5.9: Drag model parameters for the inline oscillating cylinder (no-resonance and resonance cases)

$\Omega(Hz)$	0.4	0.4
$\frac{y}{D}$	0.01	0.064
d_m	1.6488	1.7912
c_1	0.1388	0.21
k_1	0.0756	0.077
k_2	0.0944	0.101

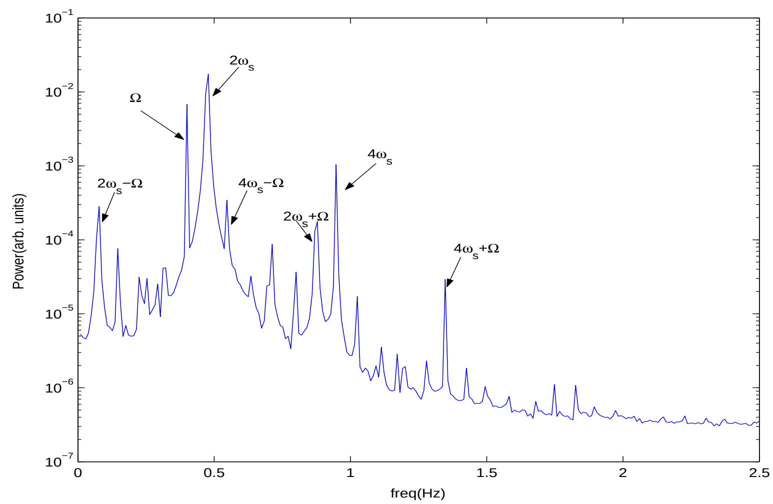

Figure 5.15: Power spectrum of the drag coefficient for the inline oscillating cylinder at frequency $\Omega = 0.4Hz$ and amplitude $\frac{y}{D} = 0.01$

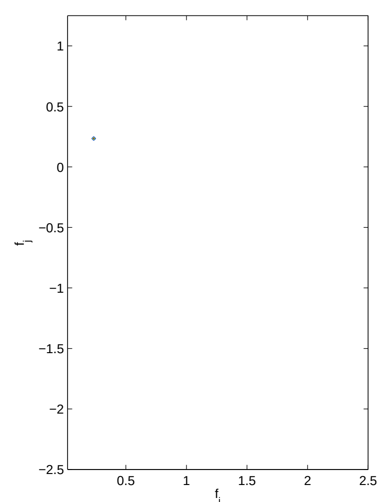

Figure 5.16: Cross-bispectrum of the lift and drag coefficients for the inline oscillating cylinder at frequency $\Omega = 0.4Hz$ and amplitude $\frac{y}{D} = 0.01$

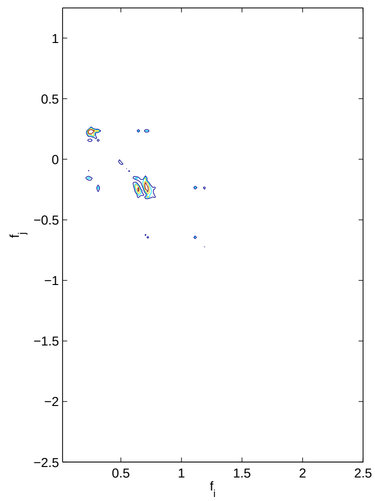

Figure 5.17: Cross-bicoherence of the lift and drag coefficients for the in-line oscillating cylinder at frequency $\Omega = 0.4Hz$ and amplitude $\frac{y}{D} = 0.01$. Contour levels are set at 0.3, 0.6, 0.9.

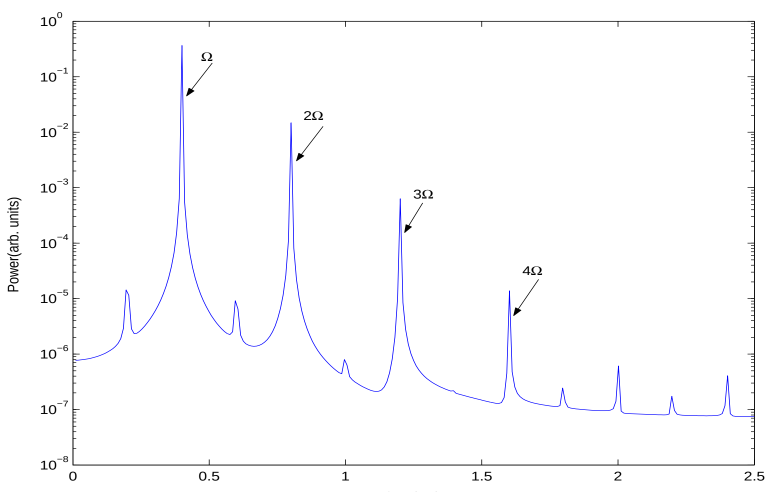

Figure 5.18: Power spectrum of the drag coefficient for the inline oscillating cylinder at frequency $\Omega = 0.4Hz$ and amplitude $\frac{y}{D} = 0.064$

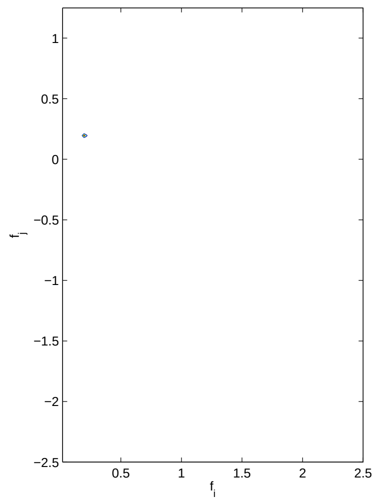

Figure 5.19: Cross-bispectrum of the lift and drag coefficients for the inline oscillating cylinder at frequency $\Omega = 0.4Hz$ and amplitude $\frac{y}{D} = 0.064$

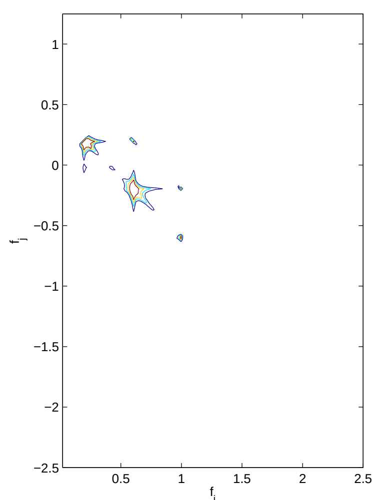

Figure 5.20: Cross-bicoherence of the lift and drag coefficients for the inline oscillating cylinder at frequency $\Omega = 0.4Hz$ and amplitude $\frac{y}{D} = 0.064$. Contour levels are set at 0.3, 0.6, 0.9.

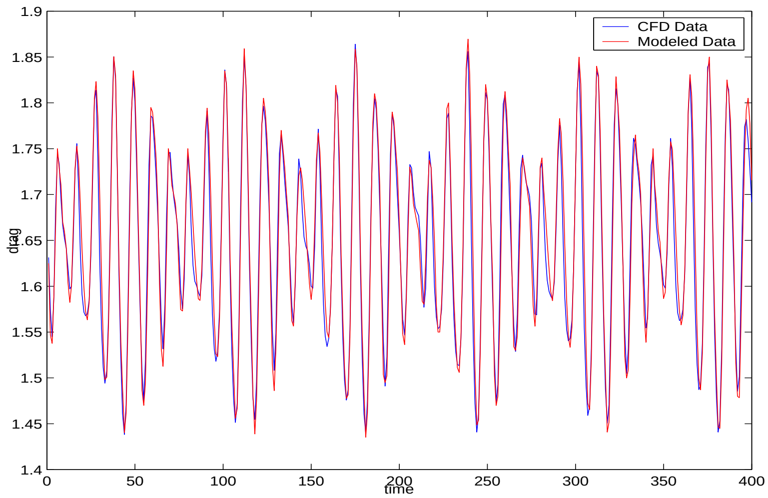

Figure 5.21: Comparison of the RANS simulated and modeled time series of the drag coefficient for the inline oscillating cylinder at frequency $\Omega = 0.4Hz$ and amplitude $\frac{y}{D} = 0.01$

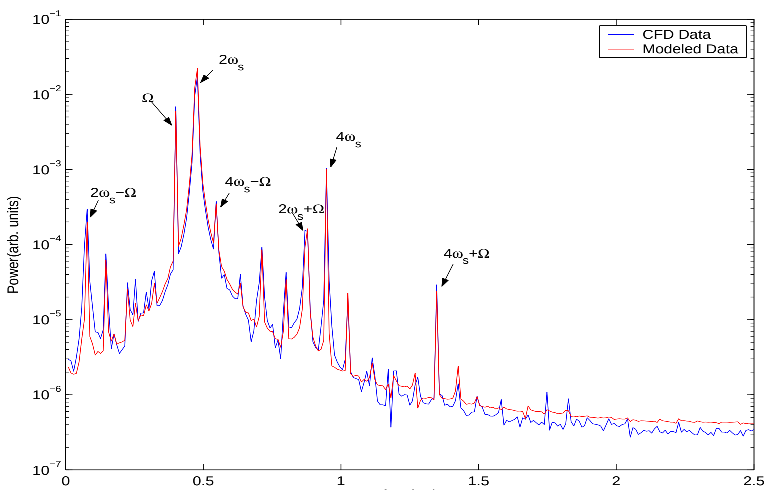

Figure 5.22: Comparison of power spectra of the RANS simulated and modeled drag coefficient for the inline oscillating cylinder at frequency $\Omega = 0.4Hz$ and amplitude $\frac{y}{D} = 0.01$

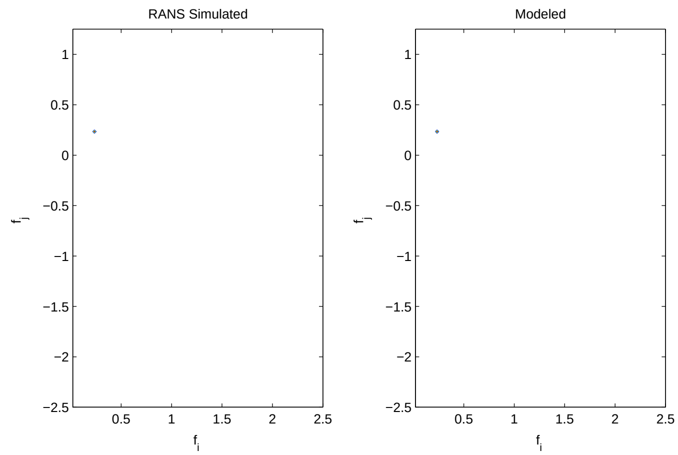

Figure 5.23: Comparison of cross-bispectra between the lift and drag coefficients of the RANS simulated and modeled time series for the inline oscillating cylinder at frequency $\Omega = 0.4Hz$ and amplitude $\frac{y}{D} = 0.01$

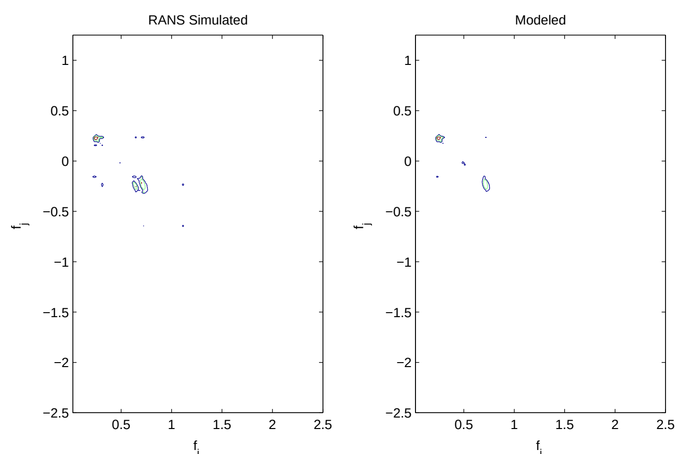

Figure 5.24: Comparison of cross-bicoherence between the lift and drag coefficients of the RANS simulated and modeled time series for the inline oscillating cylinder at frequency $\Omega = 0.4Hz$ and amplitude $\frac{y}{D} = 0.01$. Contour levels are set at 0.3, 0.6, 0.9.

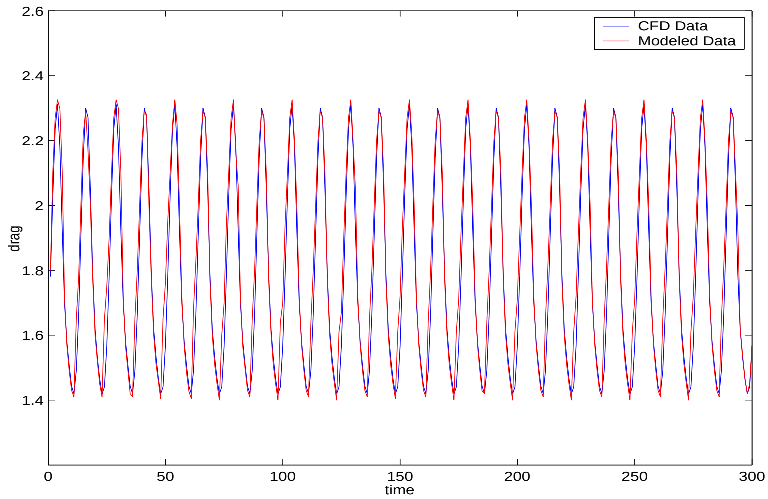

Figure 5.25: Comparison of the RANS simulated and modeled time series of the drag coefficient for the inline oscillating cylinder at frequency $\Omega = 0.4Hz$ and amplitude $\frac{y}{D} = 0.064$

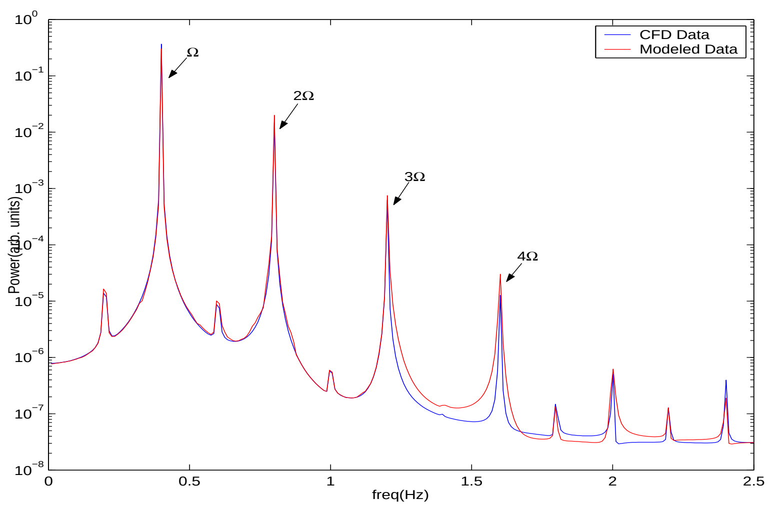

Figure 5.26: Comparison of power spectra of the RANS simulated and modeled drag coefficient for the inline oscillating cylinder at frequency $\Omega = 0.4Hz$ and amplitude $\frac{y}{D} = 0.064$

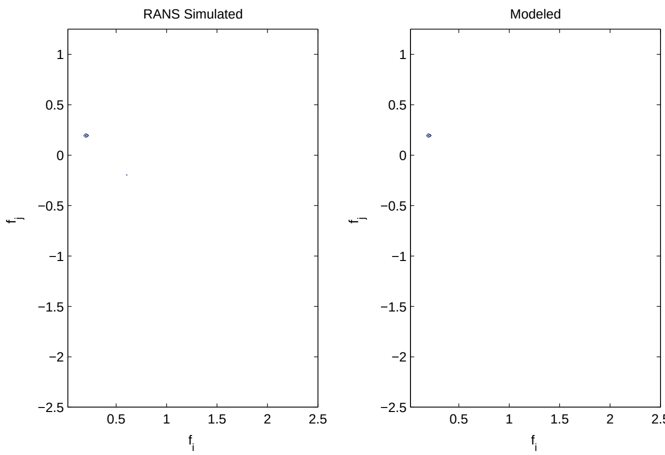

Figure 5.27: Comparison of cross-bispectra between the lift and drag coefficients of the RANS simulated and modeled time series for the inline oscillating cylinder at frequency $\Omega = 0.4Hz$ and amplitude $\frac{y}{D} = 0.064$

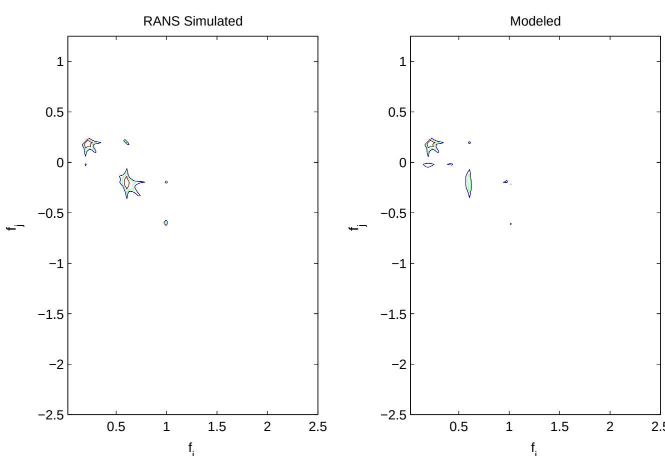

Figure 5.28: Comparison of cross-bicoherence between the lift and drag coefficients of the RANS simulated and modeled time series for the inline oscillating cylinder at frequency $\Omega = 0.4Hz$ and amplitude $\frac{y}{D} = 0.064$. Contour levels are set at 0.3, 0.6, 0.9.

Chapter 6

Prediction of Free Response from Forced Excitation Parameters

In general, and in many fluid-structure interaction applications, the question of whether forced or controlled experiments and/or numerical simulations can be used to accurately predict the free oscillations remains open. The reason lies mainly in the flow characteristics that affect the structural response. Carberry et al.[25] conducted experiments on both forced and free oscillating circular cylinders to compare the wake structures and force properties. Their results showed that, although forced sinusoidal oscillations replicate many features of the flow-induced motion, they cannot predict te free oscillations because they result in negative energy transfer for flow parameters where free oscillations are known to occur.

In this chapter, the free response based on the parameters derived in the previous chapter is numerically simulated. The simulation results are then analyzed to determine whether the models and parameters derived in Chapter 4 for the case of transversely oscillating cylinder would yield the experimental response characteristics observed by Govardhan and Williamson[26].

6.1 Model of Free Response

The equation of motion generally used to represent the vortex-induced vibrations of a cylinder oscillating in the transverse (normal to the flow) direction is written as[26]

$$m\ddot{y} + c\dot{y} + ky = F \tag{6.1}$$

where m is the structural mass, c is the structural damping, k is a spring constant and F is used to represent the fluid forcing. In the regime where the body oscillation frequency is synchronized with the votex shedding, the force and response solutions are given by:

$$F = F_0 sin(\omega t + \phi) \tag{6.2}$$

$$y = y_0 sin(\omega t) \tag{6.3}$$

The relation between the lift coefficient and lift force is given by

$$F = \frac{\rho U^2 DL}{2} l \tag{6.4}$$

where U is the mean flow velocity, D is the cylinder's diameter and L is its length and l is the lift coefficient. In nondimensional parameters, equation

6.1 can be rewritten as

$$\ddot{y} + 2\xi\frac{2\pi}{U^*}\dot{y} + (\frac{2\pi}{U^*})^2 y = \frac{2}{\pi m^*} l \qquad (6.5)$$

where ξ is the damping ratio $(\frac{c}{2\sqrt{k(m+m_A)}})$, U^* is the velocity ratio $(\frac{U}{f_n D})$ and $m^* = \frac{m}{\frac{\pi D^2 \rho L}{4}}$ is the ratio of the mass of the cylinder to the mass of its equivalent volume of the surrounding fluid. For air, m^* is large and for water m^* is smaller.

Govardhan and Williamson[26] discussed the differences in the free vibration of circular cylinders for different values of $m^*\xi$. By comparing results from high $m^*\xi$ and low $m^*\xi$, they concluded that $m^*\xi$ has an effect on the response of the cylinder. The amplitude response of the high $m^*\xi$ experiments shows two branches; an initial branch and a lower one. On the other hand, the amplitude response of low $m^*\xi$ experiments is characterized by three branches, an initial branch, an upper branch and a lower branch. The transition between the initial and upper branch is hysteritic, the transition between the upper and lower branches involves intermittent switching of modes. These differences are shown in Figure 6.1 which is a reproduction of Figure 1 of Grovardhan and Williamson[26]

Several studies, Brika and Laneville (1993), Khalak and Williamson (1999), and Hover et al. (1998), have suggested that the initial branch is associated with the $2S$ vortex formation mode, i.e. when 2 single vortices form per cycle and that the lower branch is associated with the $2P$ vortex formation mode, i.e. when 2 pairs of vortices form per cycle. Gorvardhan and Williamson[26] associate the upper branch with the $2P$ vortex formation mode. They also associate the transition from the initial branch to the upper one with a jump in the phase between the vortex force and displacement and the transition from the upper to the lower branch with a jump in the phase between the total force and displacement. The vortex force is related to the vortex dynamics. The total force includes the potential added-mass force in addition to the vortex force. Obviously, the transition from initial to upper branch response will involve a change in the phase of the vortex force since it involves a change in the vortex formation mode. The upper-lower transition corresponds to a change in the phase of the total force. Figure 6.2 which is a reproduction of Figure 7 from Govardhan and Williamson[26] shows the different regimes and vortex modes as well as jumps in phase.

The mass ratio has its own effects on the amplitude of the response. At high values of $m^* = O(100)$, synchronization takes place when the vortex shedding frequency matches the body oscillation frequency. Griffin and Ramberg (1982) and Khalak and Williamson showed that a reduction in the mass ratio increases the regime of velocity U^* over which synchronization takes place. Govardhan and Williamson [26] showed that for $m^* = O(1)$, the ratio of oscillation frequency to natural frequency can reach large values. As a matter of fact, they concluded that for $m^* < 0.54$, the synchronization regime extends to infinity. It should be noted here that the larger part of this regime is in the lower branch.

Based on the results presented in Chapter 4, and to simulate the free response of the vortex-induced vibration, the nondimensional equations of coupled lift and transverse motion are written as

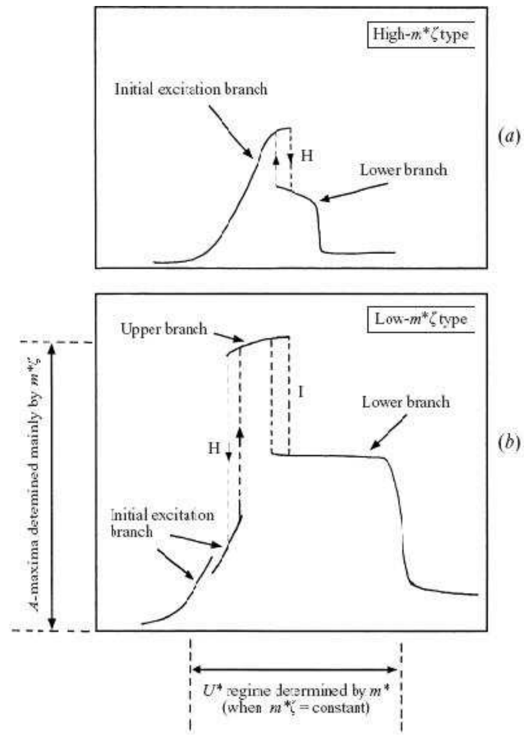

Figure 6.1: The two distinct types of amplitude response are shown here schematically. (Vertical axes represent A^* and horizontal axes represent U^*.) The Feng-type of high-($m^*\xi$) response exhibits only two branches (initial and lower), while the low-($m^*\xi$) type of response (Khalak & Williamson 1999) exhibits three branches (initial, upper and lower). The mode transitions are either hysteretic (H) or involve intermittent switching (I). The range of synchronization is controlled primarily by m^* (when $m^*\xi$ is constant), whereas the peak amplitudes are controlled principally by the product of $m^*\xi$. (Govardhan and Williamson[26] Figure 1)

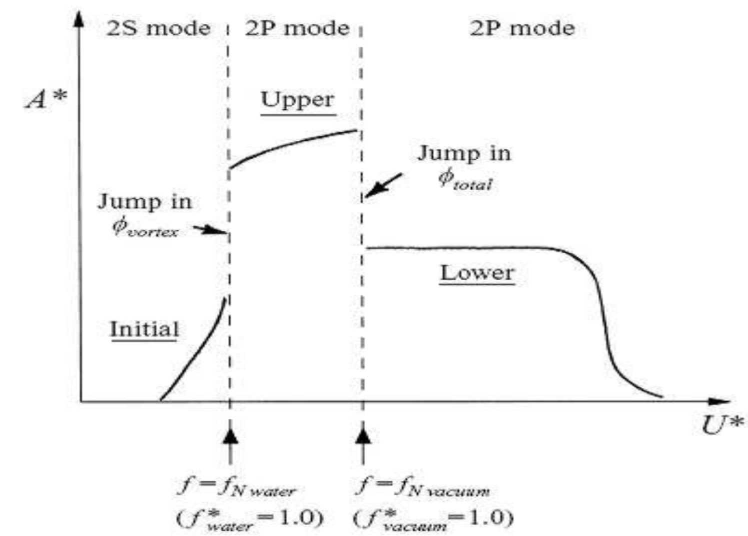

Figure 6.2: Schematic diagram of the low-($m^*\xi$) type of response showing the three principal branches (initial, upper and lower), and correspondingly the two jump phenomena. (Govardhan and Williamson[26] Figure 7)

$$
\begin{cases}
\ddot{l} + \omega_s^2 l - \mu_v \dot{l} + \alpha_v l^2 \dot{l} = k_1 y + k_2 \dot{y} \\
\\
\ddot{y} + 2\xi \frac{2\pi}{U^*} \dot{y} + (\frac{2\pi}{U^*})^2 y = \frac{2}{\pi m^*} l
\end{cases}
\tag{6.6}
$$

where l is the lift coefficient, y is the transverse oscillation of the cylinder. The values for μ_v, α_v, k_1, and k_2 are obtained from the results presented in Chapter 4.

6.2 Results

The coupled system equation 6.6 was solved using numerical techniques in MATLAB. The values for parameters in Equation 6.6 are listed in Table 6.1. The initial conditions for the numerical simulation are listed in Table 6.2. Figure 6.3 shows the amplitude and phase of the response of the free oscillation cylinder for the case of high $m^*\xi(m^* = 248$ and $m^*\xi = 0.32)$. By comparison with Figure 6.1, it is obvious that the coupled model presented in equation 6.6 can predict the initial branch for high $m^*\xi$. The results show that the maximum amplitude near 0.5 matches the reported value by Govardhan and Williamson[26]. Additionally, the observed variations in the phase in the initial region are similar to variations observed by Govardhan and Williamson[26] (see their Figure 10).

Figure 6.4 shows the amplitude and phase of the response of the free oscillation cylinder for the case of low $m^*\xi($ $m^* = 10$ and $m^*\xi = 0.013)$. Obviously, equation 6.6 and parameters presented in Table 6.1 cannot be used to predict any of the three branches observed for low $m^*\xi$. Random variations in the value of k_2 which is related to the phase between the vortex shedding and the cylinder's motion showed that the maximum amplitude and phase are strongly dependent on the sign of k_2 as well as on its magnitude. Figure 6.5 shows an example of these variations when k_2 is set equal to 0.5.

The discussion and results presented above yield the following conclusions in relation to the ability of using parameters derived from forced experiments for the prediction of free response. The initial branch in terms of maximum amplitude and phase relation between the lift force and cylinder's motions can be predicted for the case of high mass ratio. On the other hand, these parameters fail to predict the observed upper and wide lower branches at low mass ratio. The reason for this failure is that the proposed model and the analysis presented in this thesis do not account or solve for the added mass. This argument is strengthened by the realization that varying the amplitude and sign of one of the parameters yields large variations in the predicted response. Consequently, it is proposed that, in order to derive the parameters for the upper and lower branches, numerical simulations in the $2P$ regime should be performed.

Table 6.1: Parameter values in equation 6.6

Parameter	Value
μ_v	0.3052
α_v	0.3899
k_1	0.8429
k_2	-1.2140
ω_s	2*π*0.2
ξ	0.0013
m^*	10

Table 6.2: Initial values in equation 6.6

Name	Initial Value
l	1.0158
l'	-2.3786
y	0.1
y'	0.0

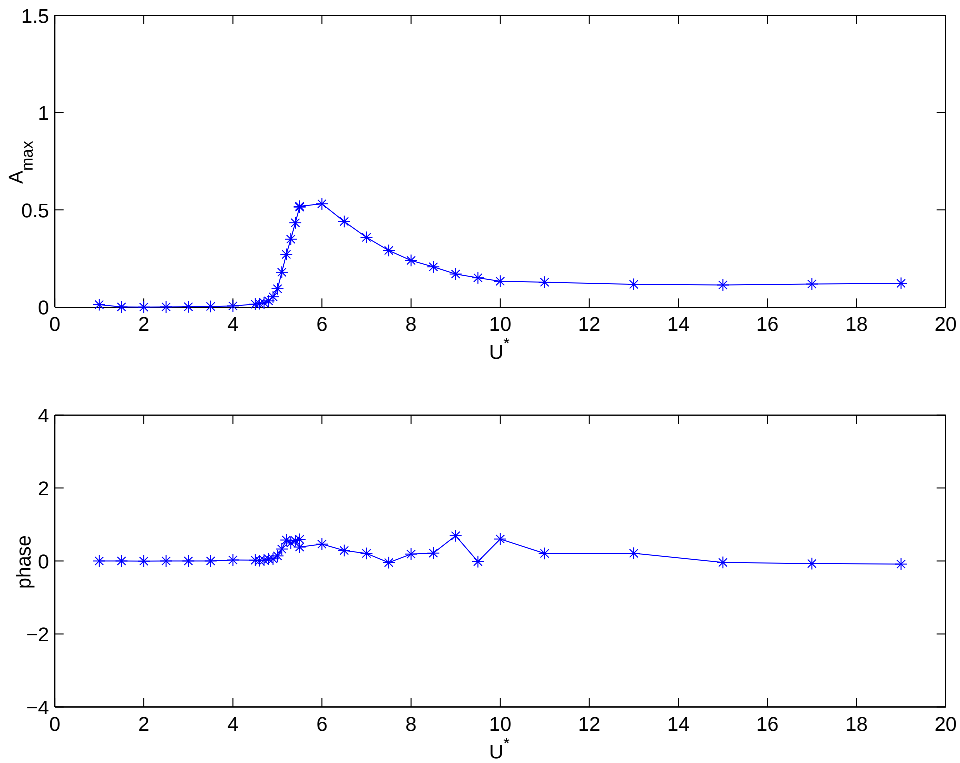

Figure 6.3: Amplitude response and phase angle variation with U^*. Case of high $m^*\xi(m^* = 248$ and $m^*\xi = 0.32)$

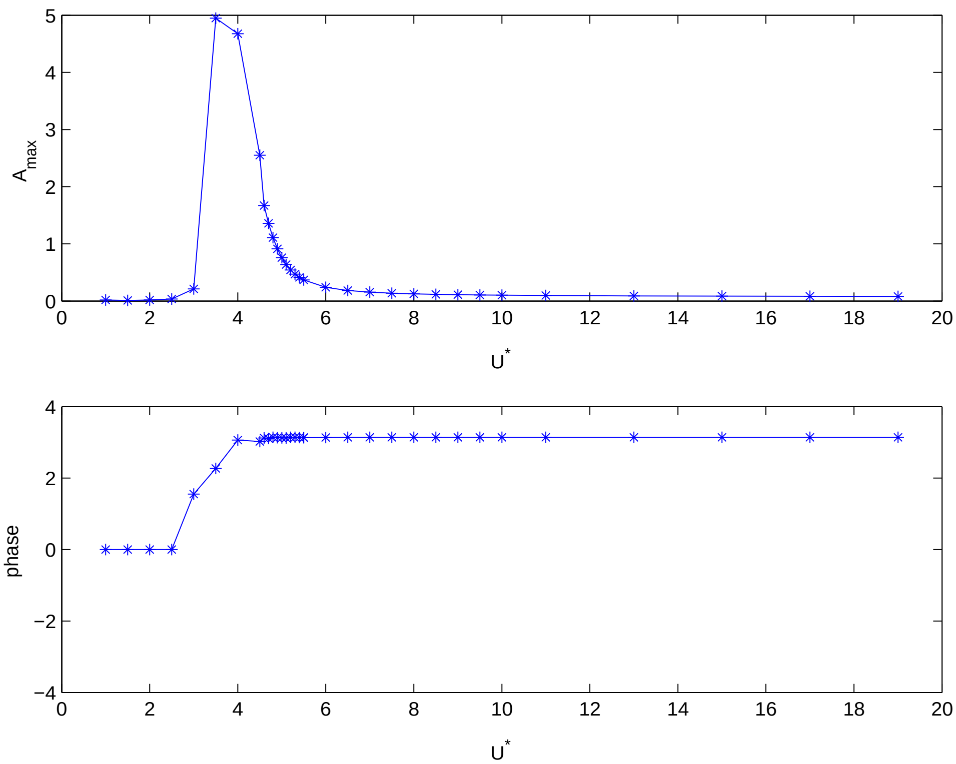

Figure 6.4: Amplitude response and phase angle variation with U^*. Case of low $m^*\xi(m^* = 10$ and $m^*\xi = 0.013$, $k_2 = -1.2140)$

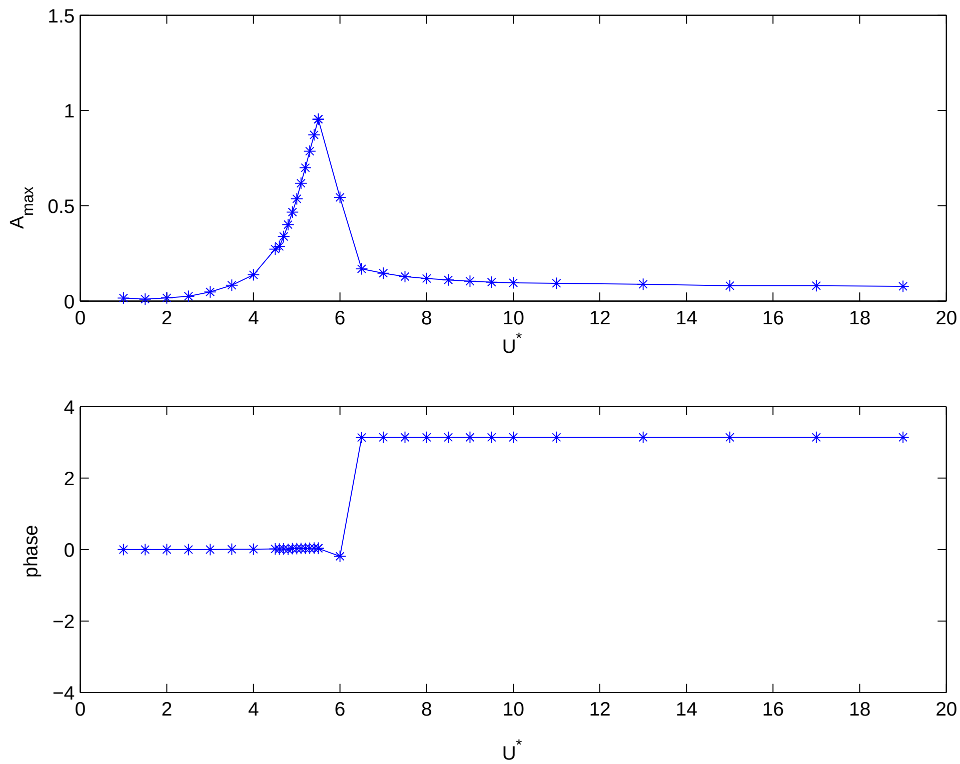

Figure 6.5: Amplitude response and phase angle variation with U^*. Case of low $m^*\xi$($m^* = 10$ and $m^*\xi = 0.013$, $k_2 = 0.5$)

Chapter 7

Conclusions

7.1 Conclusions

The major conclusions of this thesis can be summarized in the following:

First, this thesis presents a consistent approach for the development of reduced-order models for the lift and drag coefficients on oscillating cylinders. In this approach, higher-order spectral moments are developed as a tool to identify the nonlinearities in the lift and drag time series. In particular, the trispectrum is used to determine cubic nonlinearities in the lift time series. Additionally, it is shown how amplitudes and phases of these spectral moments can be combined with approximate solutions of the representative models to identify their parameters.

Second, different cases of transverse and inline oscillations were considered. The results show that the forced van der Pol equation can be used to represent the lift on a transversely oscillating cylinder. For the inline oscillating cylinder, a parametrically excited van der Pol equation should be used to model the lift coefficient. This relation between the inline oscillation and lift coefficient is of particular interest since a parametric excitation as such could enhance vortex-induced-vibrations. Additionally, it shows that allowing for both inline and transverse motions may yield higher amplitudes of vortex-induced vibrations than in cases where the inline response is inhibited. All cases of excitations lead to close values for the damping and nonlinear parameters in the van der Pol equation. Consequently, and as shown in this thesis, any excitation case could be used to identify the parameters in the governing equation. The results in this thesis show that the drag coefficient could be derived from the lift coefficient through a square relation that takes into account the effects of the forced motions.

Third, and in relation to the existing data on vortex-induced-vibrations of circular cylinders, it is noted that the model parameters derived from the forced excitation are able to predict what is observed and termed as the initial branch of the amplitude response in the high mass ratio high damping experiments. These parameters fail to predict the upper and lower branches. The reason for this failure is that the flow regime changes significantly over these branches. Data derived from experiments or numerical simulation of the flow regimes associated with the upper and lower branches should be used to determine the correct parameters. Additionally, the parameters derived in this thesis could not predict the vortex-induced-vibrations characteristics for the case of low mass ratio. The reason being that the model as formulated and the analysis as performed do not allow for an independent formulation of the added mass which is important for the case of low mass ratio.

Bibliography

[1] Williamson, C.H.K., 1996 “Vortex dynamics in the cylinder wake”, Annu. Rev. Fluid Mech., 28, 477-539

[2] Williamson, C.H.K., 1992, “The natural and forced formation of spot-like L-structures caused by vortex dislocations in wake transition”, Journal of Fluid Mechanics, 243, 393-441

[3] Schlicting, H., 1979, “Boundary layer theory”, Mcraw-Hill, New York, 7^{th} edition

[4] Abernathy, F.H., and Kronauer, R.E., 1962, “The formation of Vortex Streets”, Journal of Fluid Mechanics, 13, 1-20

[5] Gerrard, J.H., 1996, “The mechanics of the formation of vortices behind bluff bodies”, Journal of Fluid Mechanics, 25, 401-413

[6] Sarpakaya, T., 1979, “Vortex-induced oscillations: a selective review”, Journal of Applied Mechanics, 46, 241-258

[7] Provansal, M., Mathis, C., and Boyer, L., 1987, “Bernard-von karman instability: transient and forced regimes”, Journal of Fluid Mechanics, 182, 1-22

[8] Alberde, P., and Monkewitz, P.A., 1992, “A model for the formation of oblique shedding and ’chevron’ patterns in cylinder wakes”, Phys. Fluids, A4, 744-756

[9] Williamson, C.H.K., 1996, “Three-dimensional wake transition”, Journal of Fluid Mechanics, 328, 345-407

[10] Roussopoulos, K., and Monkewitz, P.A., 1996, “Nonlinear modelling of vortex shedding control in cylinder wakes”, Physica, D97, 264-273

[11] Noack B. N., Ohle, F. and Eckelmann, H., 1991, “On cell formation in vortex street”, Journal of Fluid Mechanics, 227, 293-308

[12] Balasubramanian, S., and Skop, R.A., 1996, “A nonlinear oscillator model for vortex shedding from cylinders and cones in uniform and shear flows”, Journal of Fluids and Structures, 10, 197-214

[13] Hartlen, R.T., and Currie, I.G., 1970, “Lift oscillator model for vortex-induced vibrations”, ASCE Journal of Engineering Mechanics, 96, 577-591

[14] Currie, I.G., and Turnball, D.H., 1987, “Streamwise oscillations of cylinders near the critical Reynolds number”, Journal of Fluids and Structures, 1, 185-196

[15] Kim, J., and Perkins, N.C., 2002, “Two-dimensional vortex-induced vibration of cable suspensions”, Journal of Fluids and Structures, 16(2), 229-245

[16] Nayfeh, A.H., Owis , F., and Hajj, M.R., 2003, ”A model for the coupled lift and drag on a circular cylinder”, Proceedings of DETC 2003, ASME

19^{th} Biennial Conference on Mechanical Vibrations and Noise, Sept. 2-6, 2003, Chicago, IL, USA

[17] Brillinger, D.R., 1965, "An Introduction to Polyspectra", Ann. Math. Statist., 36, 1351-1374

[18] Kim, Y.C., and Powers, E.J., 1979, "Digital bispectral analysis and its applications to nonlinear wave interactions", IEEE Trans. Plasma Sci., PS-7, 120-131

[19] Hajj, M.R., Miksad, R.W., and Powers, E.J., 1997, "Perspective: measurements and analysis of nonlinear wave interactions with higher-order spectral moments", Journal of Fluids Engineering, 1119, 3-13

[20] Brillinder, D.R. and Rosenblatt, M., 1967, "Computation and interpretation of the k^{th}-order spectra" in Spectral Analysis of Time Series, B. Harris (ed.), 189-232

[21] Hajj, M.R., Miksad, R.W., and Powers, E.J., 1993, "Fundamental-subharmonic interaction: effect of the phase relation", Journal of Fluid Mechanics, 256, 403-426

[22] Nayfeh, A. H., 1973, Perturbation Methods, Wiley, New York.

[23] Nayfeh, A. H., 1981, Introduction to Perturbation Techniques, Wiley, New York.

[24] Ali H. Nayfeh and Dean T. Mook, Nonlinear Oscillations, Wiley-Interscience, NY, May 1979.

[25] Carberry, J., Govardhan, R., Rockwell, D., and Williamson, C.H.K, 2004, "Wake states and response branches of forced and freely oscillating cylinders", European Journal of Mechanics B/Fluids, 23, 89-97

[26] Govardhan, R., and Williamson, C.H.K, 2000, "Models of vortex formation and frequency response of a freely vibrating cylinder", Journal of Fluid Mechanics, 420, 85-130